Tuning the Bose-Einstein Condensation in Spin Dimer Quantum Magnets

Dissertation

zur

Erlangung der naturwissenschaftlichen Doktorwürde
(Dr. sc. nat.)

vorgelegt der

Mathematisch-naturwissenschaftlichen Fakultät

der

Universität Zürich

von

Henrik Grundmann
aus
Deutschland

Promotionskomitee

Prof. Dr. Andreas Schilling (Vorsitz)
Prof. Dr. Ulrich Straumann
Prof. Dr. Hugo Keller

Zürich, 2014

Vorwort

In der überaus komplexen Welt der modernen Physik ist es vermutlich das Gebiet der Festkörperphysik, welchem die größten und umfangreichsten Forschungsbemühungen gewidmet sind. Diese intensiven Forschungen führten zu einer Vielzahl von außergewöhnlichen Entdeckungen wie dem Riesenmagnetowiderstand, dem Quantenhalleffekt oder der Supraleitung. Obwohl diese und viele andere Phänomene Generationen von Physikern fasziniert und inspiriert haben, erschienen die zugehörigen theoretischen Erklärungen schon aufgrund der schieren Zahl der in Festkörpern interagierenden Teilchen als oftmals fast aussichtslose Unterfangen.

Eine der elegantesten Methoden, um derartige Probleme bei der theoretischen Bearbeitung von Viel-Teilchen-Systemen zu umgehen, ist die Einführung von Quasiteilchen. Hierbei wird die überaus komplizierte Dynamik solcher Viel-Teilchen-Systeme auf ein einfacher zu behandelndes Ensemble von wechselwirkenden Quasiteilchen projiziert. Diese Quasiteilchen verhalten sich in vielen Fällen vergleichbar mit „realen“ Teilchen wie Elektronen oder Atomen und zeigen sogar ganz analoge Phänomene, wie zum Beispiel die Bose-Einstein-Kondensation.

Das dieser Arbeit zugrundeliegende Forschungsprojekt wurde ins Leben gerufen, um die Tragweite dieser Analogien an einem konkreten Beispiel zu untersuchen - den Spin-Anregungen in magnetischen Isolatoren, die sich mathematisch als bosonische Quasiteilchen beschreiben lassen. Werden diese Materialien in hohen Magnetfeldern unter eine bestimmte kritische Temperatur abgekühlt, so zeigt ihr elektronisches System einen Phasenübergang welcher als Bose-Einstein-Kondensation dieser Spin-Quasiteilchen aufgefasst wird. Obwohl ein Großteil der Eigenschaften dieses Kondensates und des zugehörigen Phasenüberganges im Rahmen dieser Beschreibung erklärt werden kann, ist diese Interpretation bis heute umstritten.

Zur näheren Untersuchung dieser Fragestellung wurde durch unsere Gruppe ein neuer experimenteller Ansatz entwickelt, welcher darauf abzielt, die langreichweitige Phasenkohärenz in diesen Systemen nachzuweisen, eine der definierenden Eigenschaften von Bose-Einstein-Kondensaten interagierender Teilchen. Diese Phasenkohärenz sollte in einem gekoppelten System aus zwei Quasiteilchen-Kondensaten mit unterschiedlichen kritischen Parametern zu charakteristischen Änderungen in den Energiespektren der beiden Kondensate führen, ähnlich den Josephson-Effekten in supraleitenden Materialien. Ein Nachweis dieser Änderungen wäre ein deutlicher Indikator für die Existenz einer lang-

reichweitigen Phasenkohärenz in diesen Systemen und daher ein starkes Argument für die Beschreibung als Bose-Einstein-Kondensat.

Die vorliegende Doktorarbeit stellt eine Art Statusmeldung für unsere derzeitigen Bemühungen zur konkreten Realisierung des oben skizzierten experimentellen Ansatzes dar. Die ersten beiden Kapitel sind dabei der Einführung der grundlegenden theoretischen Konzepte sowie der genutzten experimentellen Techniken gewidmet. Im anschließenden, zweigeteilten Hauptteil sind die eigentlichen Ergebnisse unserer Forschung zusammengefasst.

Das Kapitel 3 enthält die Beschreibung unserer erfolgreichen Versuche zur Kontrolle des kritischen Magnetfeldes des Spin-Systems $Ba_{3-x}Sr_xCr_2O_8$, einer Mischreihe aus $Ba_3Cr_2O_8$ und $Sr_3Cr_2O_8$, welche Kandidaten für die Bose-Einstein-Konsensation magnetischer Spin-Quasiteilchen darstellen. Die beobachteten Änderungen des kritischen Feldes sind dabei gegeben durch Modifikationen der magnetischen Wechselwirkungen innerhalb des Spin-Systems. Diese Wechselwirkungen werden in starkem Maße durch einen strukturellen Phasenübergang innerhalb der Kristallstruktur des Materials beeinflusst, welcher wiederum für intermediäre Kompositionen der Mischreihe graduell unterdrückt wird. Somit lässt sich das kritische Feld der Quasiteilchen-Kondensation durch Änderung der Probenstöchiometrie kontrollieren.

Versuche zur Kontrolle der kritischen Parameter für die Quasiteilchen-Kondensation mittels chemischer Substitution wurden in der Vergangeheit auch an anderen Materialien durchgeführt. Ein prominentes Beispiel hierfür ist $NiCl_2(SC(NH_2)_2)_4$ (DTN), ein System bei dem durch graduelle Ersetzung von Cl durch Br (Br-DTN) eine Reduktion des kritischen Feldes erreicht wurde. Aufgrund der deutlichen Änderung des kritischen Feldes sind in einem gekoppelten System aus DTN und Br-DTN sichtbare Änderungen der Energiespektren zu erwarten. Die zugehörigen Elektronenspinresonanz-Untersuchungen des Spin-Systems für reines DTN, Br-DTN und das gekoppelte System DTN/Br-DTN haben jedoch keine vollkommen eindeutigen Resultate erbracht und sind in Kapitel 4 dargelegt.

Bisher war unsere Suche nach Josephson-Effekten in gekoppelten Quasiteilchen-Kondensaten nicht von Erfolg gekrönt. Dennoch sind wir überzeugt, dass dieses revolutionäre Konzept überaus hilfreich sein wird um zu untersuchen, ob die Kondensation von bosonischen magnetischen Quasiteilchen tatsächlich ein Beispiel echter Bose-Einstein-Kondensation darstellt.

Preface

Solid state physics is probably the most widely studied field of modern physics. This intense research culminated in the discovery of a number of fascinating effects such as giant magnetoresistance, the quantum hall effect or superconductivity. Such phenomena have captured the interest of countless physicists, although their understanding has often been somewhat hindered by the sheer number of interacting entities in a normal solid state sample that have to be taken into account for a correct theoretical description.

One of the most beautiful and elegant principles in physics is thus the introduction of quasiparticles to map the complicated dynamics of such many-body systems onto weakly interacting imaginary particles. In many cases, these quasiparticles behave very much akin to "real" particles like electrons or atoms, showing similar properties and even exhibiting analogous phenomena such as Bose-Einstein condensation.

The present project was born out of the desire to examine how far these analogies can be driven in the case of a very specific example. The spin excitations in certain insulators can be described in the framework of bosonic quasiparticles. When cooling these materials in high magnetic fields below a certain critical temperature, their spin systems exhibit an ordering transition that has been interpreted in terms of a Bose-Einstein condensation of the bosonic quasiparticles. Although a number of reported properties can be explained in terms of this interpretation, the question of whether it fully holds or not is still a matter of debate.

We have thus developed a new experimental scheme in an attempt to specifically probe the long range phase coherence in these systems, which is a key property of a true Bose-Einstein condensate of interacting particles. This phase coherence should lead to profound changes in the energy spectrum of two quasiparticle condensates with different critical fields that are coupled to one another. An observation of these changes, which represent an analogue to Josephson effects in superconductors, would thus be a strong indication for phase coherence in these systems.

This PhD thesis presents the status of our current attempts to realize the proposed experimental scheme. As usual, the first two chapters are dedicated to introducing the basic theoretical concepts and the most important experimental techniques that have been used for this work. The main body of this thesis, however, has two distinct parts summing up the actual results of our research.

In chapter 3, we describe our attempts and success in tuning the critical field for a particular system, $Ba_{3-x}Sr_xCr_2O_8$, which is a solid solution of the triplon BEC candidates $Ba_3Cr_2O_8$ and $Sr_3Cr_2O_8$. The observed changes of the critical field are given by changes in the magnetic interaction between the electronic spins. These magnetic spin interactions are in turn heavily influenced by the gradual suppression of a structural phase transition for intermediate Sr concentrations in $Ba_{3-x}Sr_xCr_2O_8$. Although this part of the thesis represents one of the more thorough analyzes of the microscopic influence of chemical substitution on magnetic spin interactions, it is certainly not the first attempt of changing the properties of the supposed quasiparticle BEC phase. On the contrary, a number of reports exist on the change of critical parameters induced by chemical substitution in other systems.

One of these systems is $NiCl_2(SC(NH_2)_2)_4$ (DTN), where gradual replacement of Cl by Br (Br-DTN) leads to a decrease of the critical field H_{c1}. We analyzed samples of pure DTN, Br-DTN and a corresponding Josephson device of DTN and Br-DTN using high frequency ESR techniques in search for the expected changes in the energy spectrum of the device. The results of these experiments were not conclusive and are summarized in chapter 4.

Although the search for Josephson effects in coupled quasiparticle BEC did not yet yield the expected results, we believe that this pioneering concept can be key to determine whether the condensation of magnetic bosonic quasiparticles can be regarded as a true BEC.

Contents

1 Introduction **3**

1.1 BEC - accepted knowledge . . . 3
1.2 BEC in magnetic insulators - a debated concept . . . 10
1.3 Josephson effects in magnetic insulators - a proposition . . . 19

2 Experimental Techniques **25**

2.1 Magnetization experiments . . . 25
2.1.1 Measuring *M(T)* in low magnetic fields . . . 25
2.1.2 Measuring *M(H)* in high magnetic fields . . . 26
2.2 Powder diffraction techniques . . . 28
2.2.1 Structure factor . . . 29
2.2.2 Debye-Waller factor . . . 30
2.2.3 X-ray powder diffraction . . . 31
2.2.4 Neutron powder diffraction . . . 33
2.2.5 Rietveld analysis . . . 34
2.3 Electron spin resonance experiments . . . 35
2.3.1 X-band ESR . . . 38
2.3.2 High-frequency ESR in quasistatic magnetic fields . . . 38

3 Experiments on $Ba_{3-x}Sr_xCr_2O_8$ **41**

3.1 General properties of $Ba_3Cr_2O_8$ and $Sr_3Cr_2O_8$ . . . 41
3.2 Preparation of $Ba_{3-x}Sr_xCr_2O_8$ . . . 51
3.3 Crystallographic structure at room temperature from X-ray diffraction . . . 53
3.4 Obtaining J_0 from magnetization measurements . . . 55
3.5 Analyzing the magnetic background . . . 57
3.6 Estimating J_0 from high field ESR experiments . . . 58
3.7 Crystallographic structure from neutron diffraction . . . 61
3.8 Calculating J_0 by taking the structural transition into account . . . 67
3.9 A possible explanation of the suppressed structural transition by chemical disorder . . . 69
3.10 Disorder effects probed by low-frequency ESR techniques . . . 73
3.11 Examination of the critical field of $Ba_{3-x}Sr_xCr_2O_8$ using pulsed high-field magnetometry . . . 77

4 Experiments on $NiCl_2(SC(NH_2)_2)_4$ (DTN) 83
4.1 General properties of DTN 83
4.2 DTN as a prototype system for the the construction of a Josephson-device of magnetic insulators 91
4.3 ESR experiments on DTN-based samples above T_c 92
4.4 ESR experiments on DTN-based samples below T_c 97

Conclusion and Outlook 100

References 103

Appendix 112

1 Introduction

1.1 BEC - accepted knowledge

One of the most important differences between classical statistics and quantum statistics is the importance of the spin of the examined particles. This quantum mechanical property has no analogue in classical physics but causes huge differences in the low temperature behavior of fermions (half-integer spin) and bosons (integer spin). While two fermions can not occupy the same state, the possible number of bosons per state is infinite. This is reflected in the occupation probability functions for fermions (Eq. 1.1) and bosons (Eq. 1.2). The latter was introduced by Einstein [1], inspired by Bose's statistical treatment of light quanta [2].

$$f_{\mathrm{FD}} = \frac{1}{e^{\beta\left(\epsilon_{\vec{k}}-\mu\right)}+1} \tag{1.1}$$

$$f_{\mathrm{BE}} = \frac{1}{e^{\beta\left(\epsilon_{\vec{k}}-\mu\right)}-1}, \tag{1.2}$$

where μ is the chemical potential and $\beta = \frac{1}{k_B T}$. The function f thus gives the probability density for the occupation of a certain state with an energy $\epsilon_{\vec{k}}$ where $\vec{k}$ is a set of quantum numbers that define this state. The chemical potential can be viewed as the energy needed (gained) when adding (removing) one particle to the system. Einstein understood, that for a vanishing chemical potential a macroscopic number of bosons would occupy the ground state, a phenomenon now known as Bose-Einstein condensation (BEC).

According to Eq. 1.2 the occupation probability at $T = 0$ is zero for all states but the lowest state so that all bosons occupy this ground state (see Fig. 1.1). Even for finite temperatures with

$$k_B T < \epsilon_1 - \epsilon_0, \tag{1.3}$$

where ϵ_0 is the energy of the lowest state and ϵ_1 is the energy of the first excited state, a macroscopic number of bosons occupy the ground state. This is a simple result of thermal population of the states. A macroscopical occupation of the ground state, by itself, is

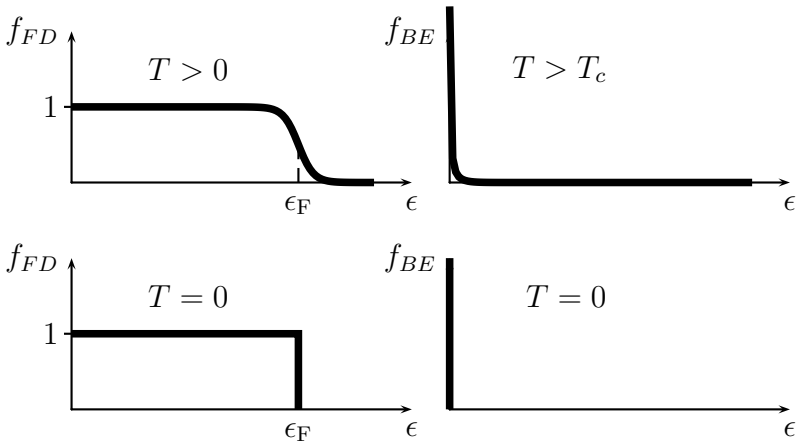

Abbildung 1.1: Sketch of the occupation probability for fermions (left) and bosons (right) at low, finite temperatures and $T = 0$. For $T = 0$ *all* bosons occupy the ground state that was chosen as $\epsilon = 0$. For fermions, the occupation probability is one for states with an energy up to the fermi energy ϵ_f and vanishes for all higher states.

therefore not puzzling. However, the temperature given by 1.3 is on the order of $10^{-20}\,\mathrm{K}$, to small to be accessed experimentally. However, the reported critical temperatures for the BEC transition range from several nK [3] to μK [4] for dilute clouds of atomic gases. The condensation temperature of ^{4}He is even on the order of 1 K.

In order to obtain an expression for the occupation number n_0 of the ground state, one can calculate n_0 as the difference between the total boson number n and the occupation number of all states above the ground state. Assuming vanishing interactions between the bosons, the Hamilton operator can be written as

$$\hat{H} = \sum_{\vec{k}} \frac{\hbar^2 \hat{\vec{k}}^2}{2m} \hat{a}^\dagger_{\vec{k}} \hat{a}_{\vec{k}} = \sum_{\vec{k}} \epsilon_{\vec{k}} \hat{a}^\dagger_{\vec{k}} \hat{a}_{\vec{k}}, \text{ or}$$
$$\hat{H} = \int \hat{\psi}^\dagger(\vec{r}) \left(-\frac{\hbar^2}{2m} \Delta \right) \hat{\psi}(\vec{r}) \mathrm{d}^3 r$$

where $\hat{a}_k$ and $\hat{a}^\dagger_k$ are the creation and annihilation operators for the state $\vec{k}$ while $\hat{\psi}^\dagger(\vec{r})$ and $\hat{\psi}(\vec{r})$ are the particle creation and annihilation operators at point $\vec{r}$. To calculate the occupation number of the ground state, we can use the expression for the total boson density,

$$\begin{aligned} n &= \sum_{\vec{k}} \left\langle \hat{a}^\dagger_{\vec{k}} \hat{a}_{\vec{k}} \right\rangle \\ &= n_0 + \int_0^\infty D(\epsilon) \frac{\mathrm{d}\epsilon}{e^{\beta(\epsilon-\mu)} - 1}. \end{aligned}$$

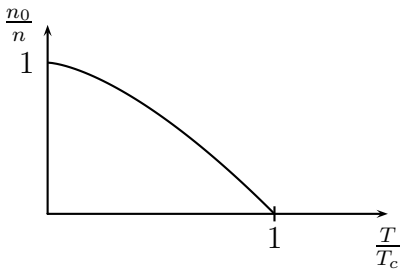

Abbildung 1.2: The macroscopic occupation of the ground state below the critical temperature T_C in a bosonic system without interactions.

Here we excluded the ground state from the integration since the dispersion relation $\epsilon\vec{k} = \frac{\hbar^2 k^2}{2m}$ in a $S = 0$ system leads to a density of states of: $D(\epsilon_{\vec{k}}) = \frac{V}{4\pi^2}\left(\frac{2m}{\hbar^2}\right)^{\frac{3}{2}}\sqrt{\epsilon_{\vec{k}}}$. This would give a vanishing weight to the ground state, even if macroscopically occupied. By specifically excluding the ground state from the integration, this problem is circumvented. The integration is solved in textbooks [5] and we have:

$$n = n_0 + \zeta\left(\frac{3}{2}\right)\left(\frac{mk_BT}{2\pi\hbar^2}\right)^{\frac{3}{2}}.$$

With $\zeta\left(\frac{3}{2}\right)\left(\frac{mk_B}{2\pi\hbar^2}\right)^{\frac{3}{2}} = \frac{n}{T_c^{\frac{3}{2}}}$, we arrive at:

$$\frac{n_0}{n} = 1 - \left(\frac{T}{T_c}\right)^{\frac{3}{2}}. \tag{1.4}$$

Even without interactions, a system of bosons exhibits a temperature induced phase transition with a non-vanishing portion of the particles occupying the ground state. Below the critical temperature, the occupation of the ground state increases until all bosons occupy the ground state at $T = 0$. The behavior of $n_0(T)$ (see Fig. 1.2) will be an important aspect when identifying phase transitions in spins systems as a BEC of quasiparticles (see section 1.2).

This transition takes place when the chemical potential μ vanishes. Note that the exponent $\frac{3}{2}$ in Eq. 1.4 follows from the assumed dispersion relation $\epsilon_{\vec{k}}$ and is no general property of a system of bosons. The first important property of the Bose-Einstein condensation is thus the macroscopic occupation of the systems ground state at temperatures well above zero.

Furthermore one expects the heat capacity C_V to exhibit a specific behavior at the condensation point. It is commonly accepted [6] that C_V increases as $T^{\frac{3}{2}}$ until $T = T_c$ and decreases for higher temperatures until C_V reaches the classical Dulong-Petit value for an ideal gas (see Fig. 1.3). The heat capacity shows no singularity but only a change of the slope at the transition point (a cusp). This is specific to any non-interacting gas of bosons.

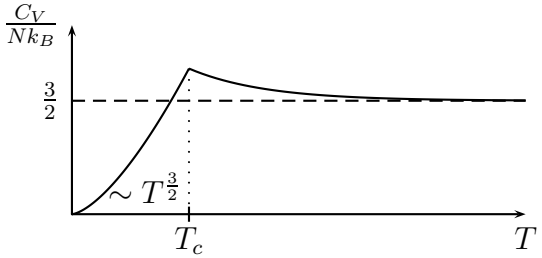

Abbildung 1.3: Sketch of the heat capacity per boson as a function of the temperature. As expected for high temperatures, the heat capacity converges to the classical Dulong-Petit result $C_V = \frac{3}{2}Nk_BT$. For small T, the heat capacity decreases as $T \to 0$

For the strongly interacting bosonic system ^{4}He [5] but even for weakly interacting bose gases [7], a divergence develops at the critical temperature resulting in a λ-shape of C_V. More precisely, the heat capacity diverges as $C_V(T) = C_0(T) + A_\pm|T - T_c|^{-\alpha}$ with a smooth base function C_0 and the critical exponent $\alpha = 0.0151$ [8], which is also characteristic for the XY-universality class.

The BEC transition is characterized by an macroscopic wave function $\psi_0(\vec{r}) = \langle\hat{a}\rangle = \sqrt{n_0}e^{i\phi}$, where ϕ denotes the phase of the wave function. This phase is related to the fact that the condensed system is in a coherent state. Such a description of the system is only possible in the BEC state so that ψ_0 is an order parameter of the transition. The idea of coherent states is often illustrated based on eigenstates of the annihilation operator in the case of the harmonic oscillator:

$$\hat{a}\,|\alpha\rangle = \alpha\,|\alpha\rangle\,, \tag{1.5}$$

where $\alpha = |\alpha|e^{i\phi}$ is a complex number. Annihilating one particle therefore leads to a global damping and a phase shift of the state $|\alpha\rangle$. The state $\hat{a}\,|\alpha\rangle$ is a superposition of eigenstates of the oscillator, $|\alpha\rangle = \sum_n c_n\,|n\rangle$. As the effect of the annihilation operator on $|n\rangle$ is given by $\hat{a}\,|n\rangle = \sqrt{n}\,|n-1\rangle$, we have

$$\begin{aligned}\hat{a}\,|\alpha\rangle &= \sum_{n=0}^{\infty} c_n\sqrt{n}\,|n-1\rangle \\ &= \sum_{n=0}^{\infty} c_{n+1}\sqrt{n+1}\,|n\rangle \overset{!}{=} \alpha\sum_{n=0}^{\infty} c_n\,|n\rangle\,,\end{aligned}$$

so that $c_n = \frac{\alpha^n}{\sqrt{n!}}c_0$. With $1 \overset{!}{=} \langle\alpha|\alpha\rangle = c_0^2\sum_{n=0}^{\infty}\frac{|\alpha|^{2n}}{n!} = c_0^2e^{|\alpha|^2}$, the constant c_0 can be calculated to $c_0 = e^{-\frac{|\alpha|^2}{2}}$, so that condition 1.5 can be achieved by

$$|\alpha\rangle = e^{-\frac{|\alpha|^2}{2}}\sum_{n=0}^{\infty}\frac{|\alpha|^n e^{in\phi}}{\sqrt{n!}}\,|n\rangle\,. \tag{1.6}$$

As $|\langle n|\alpha\rangle|^2 = \frac{\alpha^{2n}}{n!}e^{-|\alpha|^2}$, we see that the overlap of $|\alpha\rangle$ with $|n\rangle$ is given by a Poissonian distribution. The maximum of this distribution can be found at $n = |\alpha|^2$ so that for very small α the ground state has the largest contribution to the coherent state.

It can be shown that the particle number operator $\hat{n}$ and the phase operator $\hat{\phi}$ form a conjugated pair so that $\Delta n \Delta\phi \geq \frac{1}{2}$ [5]. As $\Delta\phi = \sqrt{\left\langle \hat{\phi}^2 \right\rangle - \left\langle \hat{\phi} \right\rangle^2} = 0$, the phase of the coherent state is well defined, while the total particle number is not.

The specific value of the phase ϕ is not dictated by the isotropic Hamilton operator of the system. On the contrary, it is spontaneously chosen by the system upon condensation. Although this phase can not be directly measured, phase *differences* between two coupled condensates have profound, measurable effects (see section 1.3). The complex order parameter can be thought of as a two-dimensional vector in the complex plane. Such a two-dimensional order parameter is characteristic for systems that belong to the so called XY universality class[1]. The emergence of this coherent (global) phase is therefore an important aspect of the Bose-Einstein condensation.

It may be noted that Eq. 1.6 allows to gain insight into the basic idea of *coherent states* and to introduce the particle number operator and the phase operator. For systems that undergo a BEC, however, this particular ansatz is not applicable. As stated in the beginning of this section, the ground state of a system in the BEC phase is macroscopically occupied so that the particles in this ground state should strongly contribute to the macroscopic wave function. Thus, the absolute value of the order parameter $\sqrt{n_0}e^{i\phi}$ should increase with the contribution of the ground state to the coherent state. In the above case of the harmonic oscillator, the ground state contribution is largest for a vanishing order parameter $\alpha = 0$ and decreases as $\alpha \to 1$. This is due to the fact that we explicitly used the eigenstates of the harmonic oscillator and not of our actual bosonic system.

A more appropriate ansatz was presented by Bogoliubov [9] for the field operator $\hat{\psi}(\vec{r})$ that constitutes our coherent state:

$$\begin{aligned}\hat{\psi}(\vec{r}) &= \theta_0(\vec{r})\sqrt{N_0} + \sum_{i\neq 0}\theta(\vec{r})\delta\hat{a}_i \\ &= \psi_0(\vec{r}) + \delta\hat{\psi}(\vec{r}).\end{aligned}$$

This ansatz, which is justified in the condensed phase when the ground state is macroscopically occupied ($N_0 >> 1$) so that the operator $\hat{a}_0$ can be replaced by $\sqrt{N_0}$, extends the condensation concept to the case of weakly interacting bosonic gases [9, 10]. Here,

[1] When two systems fall in the same universality class, parameters like the heat capacity C, the correlation length ξ or the ordering parameter show the same dependence on the reduced temperature $\epsilon = \frac{T-T_c}{T_c}$ for ϵ close to 0, independent of details of the specific interactions in the system [6]. They are then given by power laws with certain critical exponents, e.g. $C \propto \epsilon^{\alpha}$ or $\xi \propto \epsilon^{\nu}$. These critical exponents are, per convention, denoted by the common greek letters α, β, γ, δ, ν and η.

the interaction potential between the bosons is usually approximated by a hard-core interaction of strength ν_0 so that the Hamilton operator may be written as

$$\hat{H} = \sum_k \left(\frac{\hbar^2 k^2}{2m} - \mu \right) \hat{a}_k^\dagger \hat{a}_k + \frac{\nu_0}{2} \sum_{k,k',q} \hat{a}_{k+q}^\dagger \hat{a}_{k'-q}^\dagger \hat{a}_k \hat{a}_{k'}. \tag{1.7}$$

The introduction of interactions has several consequences. In the case of a condensate of non-interacting bosons, we have stated that the condensation occurs when the chemical potential μ vanishes. In the case of interacting bosons, the condensation occurs when $\mu = 2t_0\zeta\left(\frac{3}{2}\right)(4\pi)^{-\frac{3}{2}} T^{\frac{3}{2}}$. This yields the phase boundary for variable chemical potentials and can be of interest when comparing different condensates. The exponent $\frac{3}{2}$ is again a consequence of the dispersion relation $\epsilon_{\vec{k}} = \frac{\hbar^2 k^2}{2m}$ of the bosons and the fact that we have to consider three spacial dimensions. It is *no* critical exponent of the XY-universality class.

One of the most important differences introduced by the weak interactions is the phenomenon of superfluidity, i.e. a flow without resistance. This phenomenon has been first discovered by Kapitza [11] and Allen [12]. Kapitza used a setup as shown in Fig. 1.4 with a cylinder filled with liquid He. This cylinder could be emptied through a slit of variable diameter. With the lowest diameter (about 0.5 µm), and a temperature above the critical point, $T_\lambda > 2.17\,\mathrm{K}$, it took several *minutes* until the He level in the cylinder and the dewar were equal. Once the temperature was below T_λ, the He level were aligned in several *seconds*, indicating an extreme decrease of viscosity (in terms of laminar motion), motivating Kapitza to use the term *superfluid* to describe this frictionless flow.

Landau deduced that superfluidity is a consequence of a coherent state and is impossible if the dispersion relation for this state is parabolic as in the case of free particles. The argument is based on a microscopic concept of flow resistance as scattering from the walls of the container of the fluid. When the flow moves with a speed $\vec{v}$, scattering from the wall would lead to a change of the momentum by $\delta\vec{p}$ and a change of the kinetic energy by $\Delta E = \vec{v}\Delta\vec{p}$. No matter how slow the particles move, this can always be fulfilled due to $E(\vec{p}) = \frac{p^2}{2m}$. If, however, the energy depends linearly on the momentum, scattering becomes impossible. This linear part in the dispersion relation is the so called *Goldstone*-mode. Boguliobov [9] could show that the excitation spectrum of an interacting condensed Bose-Gase is given by

$$E(\vec{k}) = \left(\frac{\hbar^2 k^2}{2m} \right)^{\frac{1}{2}} \left(\frac{\hbar^2 k^2}{2m} + 2n_c\nu_0 \right)^{\frac{1}{2}}.$$

For wave numbers smaller than the inverse coherence length, $|\vec{k}| < \frac{1}{\xi}$ with $\xi = \frac{\hbar}{2mn_c\nu_0}$, this excitation spectrum becomes linear with $E(\vec{k}) \approx \hbar c_0 |\vec{k}|$ and the particles move

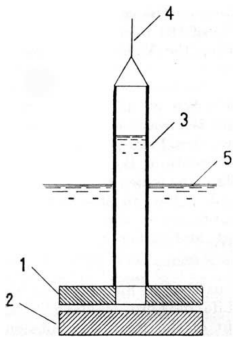

Abbildung 1.4: Sketch of the experimental setup used by Pyotr Kapitza to measure the viscosity of He below the λ-point, reproduced from [11]. Two optically flat glass discs (1 and 2) are emerged into liquid ^{4}He (5). A glass cylinder (3) is connected to the upper disc. The whole arrangement is suspended on a thread (4) that can be used to lift or lower the cylinder with the discs, thereby increasing or decreasing the He level in the cylinder with respect to the level in the dewar.

collectively. The constant $c_0 = \sqrt{\frac{n_c \nu_0}{m}}$ is the sound velocity, i.e. the speed at which these excitations propagate, and it can be deduced, e.g. from measuring the dispersion relation $E(\vec{k})$ with neutron scattering techniques. The presence of a Goldstone-mode is therefore an important feature of true Bose-Einstein condensation of interacting bosons.

Contrary to the frictionless fluid found moving through capillaries in Kapitza's experiments, the famous experiment by Andronikashvili [13](translated in [14]) clearly showed that a pile of discs emerged in liquid helium is still subject to friction with the He-system, even below T_λ. However, the friction decreases smoothly until it would disappear at $T = 0$. This suggests that either the friction itself or the amount of substance that causes the friction decreases with temperature.

The seemingly contradictory results from disc- and capillary experiments can be readily reconciled based on the *two fluid model*, shown in Ref. [15]. Like in the case of weakly interacting bosons, not all ^{4}He particles are in the condensed, superfluid state at finite temperatures. Therefore, a pile of sufficiently spaced discs emerged in ^{4}He at $T > 0$ will always be exposed to friction from the normal fluid, even though the superfluid part does not inhibit the discs motion. As the portion of the normal fluid decreases with $T \to 0$, this resistance will decrease as well. When connecting two reservoirs of ^{4}He with a very thin capillary, we have a kind of filter that only permits the superfluid to move between the to reservoirs while movement of the normal fluid is completely inhibited. Such an experiment will therefore only measure the viscosity of the superfluid phase [15].

The two fluid model is also able to explain the large thermal conductivity of ^{4}He below the λ-point. Keesom *et al.* [16] have demonstrated that in ^{4}He, the thermal conductivity κ strongly increases as liquid ^{4}He is cooled below $T = 2.2\,\mathrm{K}$ at atmospheric pressure.

These results have been further refined by Kerrisk *et al.* [17] showing that κ shows a singularity when approaching the λ-point that also depends on the pressure p over $\kappa \propto (T - T_\lambda(p))^{-\beta}$, with $\beta = 0.423$ [2]. This strong increase seems puzzling at first when using the two fluid model. The contribution of the normal fluid should change smoothly as its properties are not affected by the emergence of the superfluid. The superfluid itself can carry no entropy and therefore no heat, giving no contribution to the thermal conductivity. Naively, a smooth decrease of κ would therefore be expected with $T \to 0$ as the superfluid portion increases monotonously. Therefore, another mechanism than pure diffusion has to be responsible for the observed results.

The strong increase of κ has been explained by London *et al.* [18] in terms on internal convection in the system, as suggested by Kapitza [11]. The normal fluid flows from the warmer part to the colder part of the system, carrying thermal energy. This energy is deposited at the colder end where parts of the normal fluid condense and become part of the superfluid. This superfluid moves frictionless in the opposite direction and becomes normal fluid at the warmer end of the system. This mechanism is very effective, making ^{4}He below the λ-point a better heat conductor than even copper or sapphire. As this principle is not a consequence of the specific interactions in ^{4}He, but of the superfluidity, any system of interacting bosons should show an extremely increased thermal conductivity once the BEC sets in.

Many of the above mentioned phenomena have been discovered in real bosonic systems apart from ^{4}He, classifying them as realizations of a true BEC. These systems include dilute atomic gas clouds [19] and pumped exciton-polariton and magnon condensates [20, 21, 22, 23]. A certain kind of magnetic insulators is supposed to show a BEC of magnetic quasiparticles constituted from spin singlets and triplets, so called *triplons* which will be discussed in the next section. When discussing the possibility of such a triplon BEC, it is important to keep in mind the key properties of a BEC of interacting bosons: a macroscopic occupation of the ground state, a divergent heat capacity at the transition point, the macroscopic phase coherence of the system and superfluidity (connected with a Goldstone mode).

1.2 BEC in magnetic insulators - a debated concept

The electronic spins in a solid are in many cases localized at specific sites of the underlying crystal lattice. One can therefore think of this arrangement as a lattice of spins. The simplest example of such a lattice would be a chain of spins with distance a and an interaction strength J_I (a Heisenberg chain, see Fig. 1.5). This fundamental system has been studied extensively over the last century both with and without external ma-

[2] Also not one of the critical exponents of the XY-universality class.

gnetic fields [24, 25, 26]. The exact solution for this model leads to a gapless excitation spectrum $\omega(k) = \frac{\pi}{2}\sin(ak)$ (see Fig. 1.5).

If one now considers an additional, identical spin chain and introduces an interaction between opposing spins of the two chains, J_r, the model is extended to a spin ladder with a leg interaction J_l and a rung interaction J_r. The properties of this ladder are then given by the relative strength of the interactions. It has been shown theoretically that spin ladder systems exhibit an energy gap Δ (spin gap) that is strongly depending on $\frac{J_\mathrm{r}}{J_\mathrm{l}}$ [27, 28]. When this spin gap is overcome through the application of a strong enough external magnetic field, one can observe an ordering of the spin system. Mathematically, this transition is in the same universality class as the condensation of hard-core bosons [29]. When mapping the spin system onto a system of bosons, an $S = 1$ state of an isolated rung can be seen as the presence of a boson a this site while the $S = 0$ ground state represents the absence of a boson. The hard-core condition is then due to the fact that each rung can only contain one of these excitations that are seen as quasi-bosons.

An ordering phase transition similar to that of the above described two-dimensional ladders has been reported for the spin system $TlCuCl_3$ [30, 31]. Structural examinations have shown a ladder-like arrangement of the Cu^{2+} ions, but with an additional diagonal interaction J_diag [30]. Theoretical analysis of such a model have revealed the existence of a spin gap [32, 33], similar to the simple ladder arrangement above. This spin gap leads to a broad peak in the magnetization $M(T)$ as a function of the temperature around $T = 40\,\mathrm{K}$(see Fig. 1.6b) that can be described in terms of a spin-triplet system [34] (see section 3.1). An important characteristic of the ordering transition is an increase of the magnetic moment parallel to the external magnetic field below a critical temperature T_c that is reminisent of $n(T)$ in a BEC (see Fig. 1.6).

As J_r is much larger than the other magnetic interactions [35], it is justified to think of $TlCuCl_3$ as a system of antiferromagnetically coupled dimers with weak interdimer interactions. This model naturally results in a gap in the magnetic excitation spectrum due to the energy difference between the singlet and triplet states of the dimers. For dimers with an antiferromagnetic intradimer interaction constant J_0 but vanishing interdimer interactions, the ground state is a singlet as well, that is energetically separated by J_0 from higher lying triplet states (see Fig. 1.7). With increasing interdimer interactions, the triplet states exhibit a certain dispersion with a finite bandwidth, similar to the case of lattice excitations (phonons) of coupled atoms in a crystal lattice. Thus, the spin gap Δ is generally not equal to J_0.

As the dispersion is only present in the triplet states, the resulting quasiparticles are usually called *triplons*. In addition to a strong rung coupling J_r, further examinations on [35]$TlCuCl_3$ have shown that the model of isolated ladders with diagonal interactions is only a rough approximation. In fact, neutron scattering experiments on single crystals of $TlCuCl_3$ revealed that a total of six different interactions paths have to be taken into account for an adequate description of the obtained quasiparticle dispersion [35].

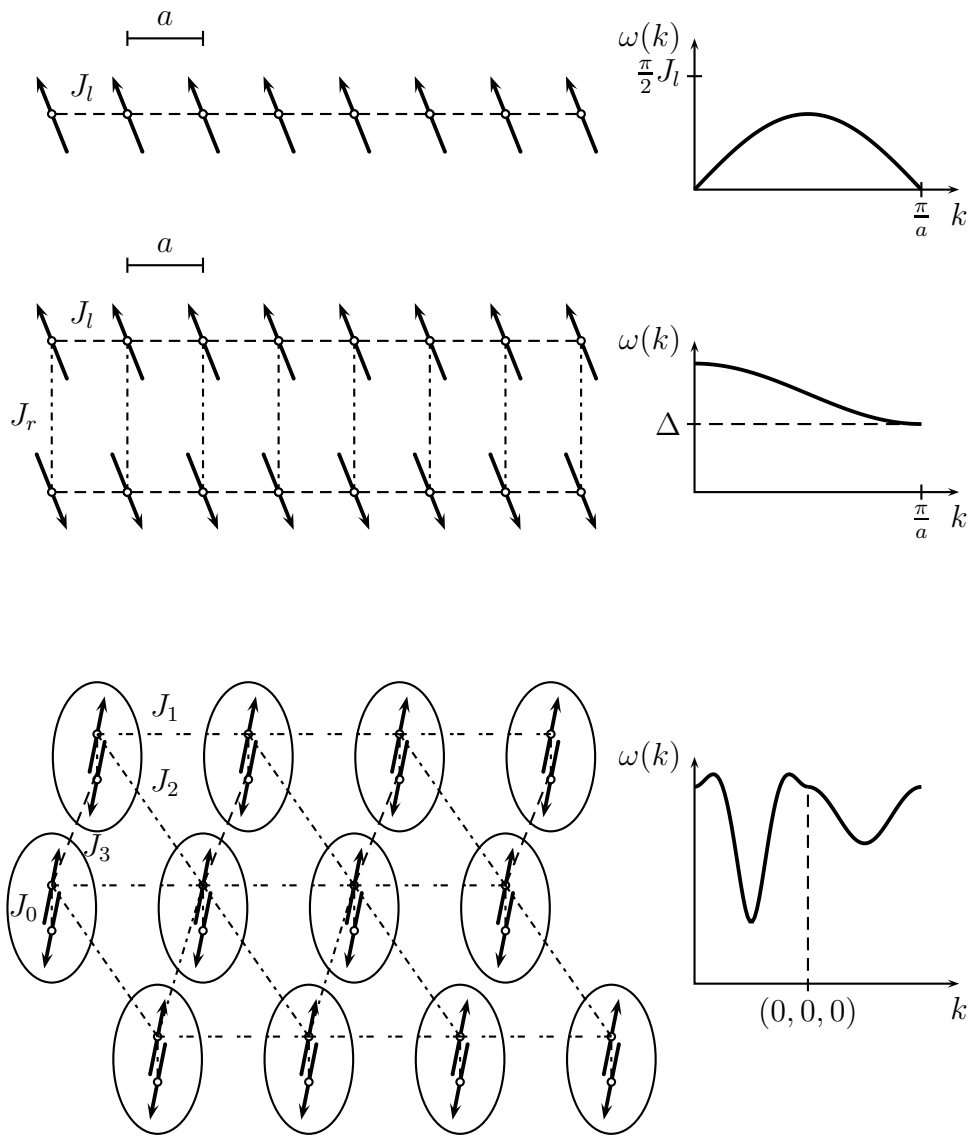

Abbildung 1.5: Sketches of the different spin systems mentioned in the text (left side) and the corresponding dispersion relations $\omega(k)$ (right side) based on the references given in the text. The path of each interaction J is depicted with a dashed line. Top: single spin chain, middle: spin ladder, bottom: three-dimensional dimer system. The dispersion relation for the ladder is given for the case of strong coupling $J_r >> J_l$.

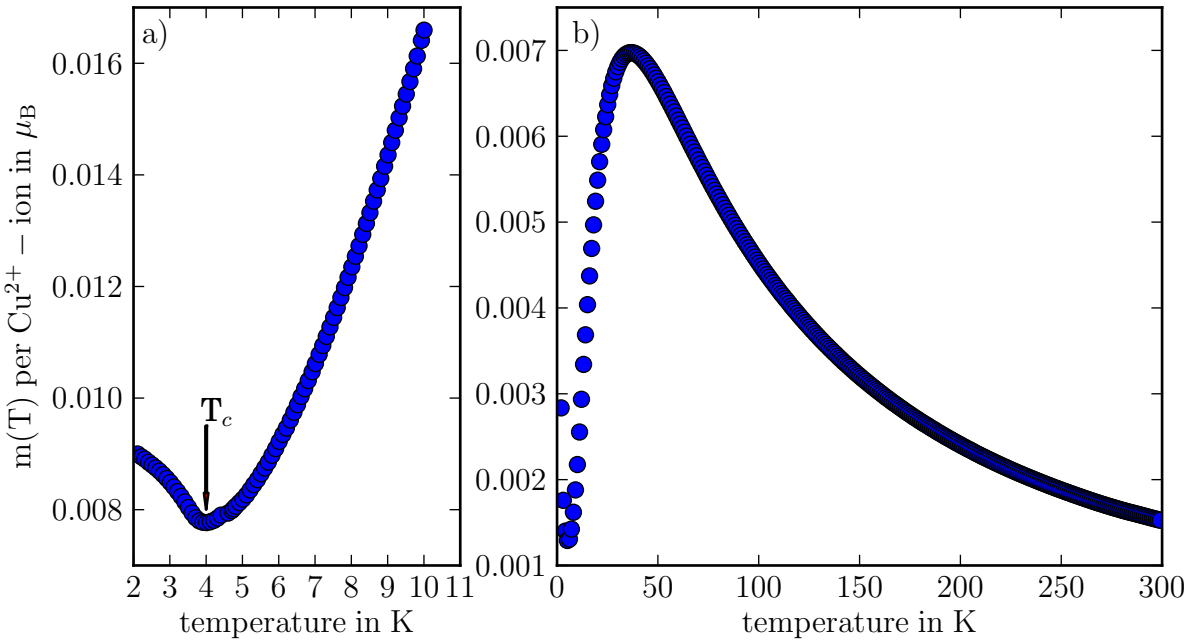

Abbildung 1.6: Magnetic moment parallel to the external field per Cu^{2+} ion in $TlCuCl_3$ in magnetic fields of $B = 7\,\mathrm{T}$ (a) and $B = 1\,\mathrm{T}$ (b).

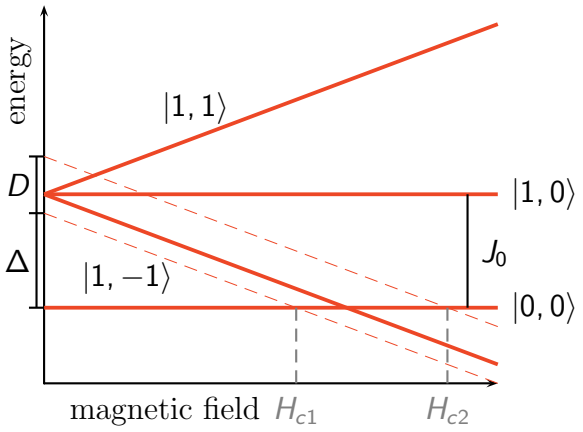

Abbildung 1.7: Sketch of the states of a weakly interacting spin dimer system with antiferromagnetic interaction constant J_0 as a function of an external magnetic field B. H_{c1} and H_{c2} are here the critical fields at zero temperature.

This triplon model has been successfully applied to a variety of spin-$\frac{1}{2}$ systems that are candidates for a field induced BEC of quasiparticles with two- or three-dimensional interactions [36, 37, 38, 39].

The complexity of the triplon dispersion resulting from the interdimer interactions can be reduced at temperatures and fields close to the transition point (field H_{c1} in Fig. 1.7) as only the lowest part of the triplon band will be occupied. Nikuni *et al.* have assumed a quadratic dispersion relation to describe the observed behavior of the magnetization at temperatures below $T = 4\,\mathrm{K}$ in high magnetic fields in terms of a BEC of triplons [40]. The resulting Hamilton operator already bears close resemblance to that of a gas of bosons with hard-core interaction strength ν_0 (compare 1.7):

$$\hat{H} = \sum_k \left(\frac{\hbar^2 k^2}{2m} - \mu \right) \hat{a}_k^\dagger \hat{a}_k + \frac{\nu_0}{2} \sum_{k,k',q} \hat{a}_{k+q}^\dagger \hat{a}_{k'-q}^\dagger \hat{a}_k \hat{a}_{k'},$$

($\hat{a}$ and $\hat{a}^\dagger$ are the usual Hartree-Fock creation and annihilation operators). Based on the Hartree-Fock-Popov approximation, the calculations predict an increase of the total triplon density for decreasing temperature below the transition, $T < T_c$,

$$n\left(T\right) = n\left(T_c\right) \left(2 - \left(\frac{T}{T_c} \right)^{\frac{3}{2}} \right). \tag{1.8}$$

As the triplons carry a spin of $S = 1$, the total triplon density $n(T)$ is connected to the average longitudinal magnetic moment $\langle m_z \rangle$ per dimer, $\frac{\langle m_z(T) \rangle}{N_d} = g\mu_B n\left(T\right)$. This relationship makes it possible to explicitly calculate the condensate density as a function of the magnetic field. The experimental results (see Figs. 1.6 and 1.8) are qualitatively well reproduced, although the experimental exponent α for

$$m_z \propto \left(2 - \left(\frac{T}{T_c} \right)^{\alpha} \right) \tag{1.9}$$

does not agree with the theoretical prediction from Eq. 1.8 [41].

The phase boundary $H_c(T)$ is also shown to follow a power law, $H_c(T) - H_c(0) \propto T^\phi$. This dependency is only valid close to the critical point and therefore poses no contradiction to the domelike shape of the global phase boundary, e.g. later presented in Fig. 3.2. The theoretical prediction of $\phi = \frac{3}{2}$ [29] is in reasonable agreement with the actual experimental values for the some of the examined systems (DTN [42], $Sr_3Cr_2O_8$ [37]), but not all of them ($TlCuCl_3$ [40]). At the condensation point, an order parameter $\langle \hat{a}_0 \rangle$ emerges with $\langle \hat{a}_0 \rangle \propto T^\beta$. The exponent gives insight about the universality class of the system. According to Nikuni *et al.* the system belongs to the 3D XY universality class with $\beta \approx 0.3485$ [43]. The exponents β and ϕ are not directly related.

Besides the details of the condensation process, one has to carefully analyze the properties of the condensate itself before classifying a phase as a BEC. The macroscopic

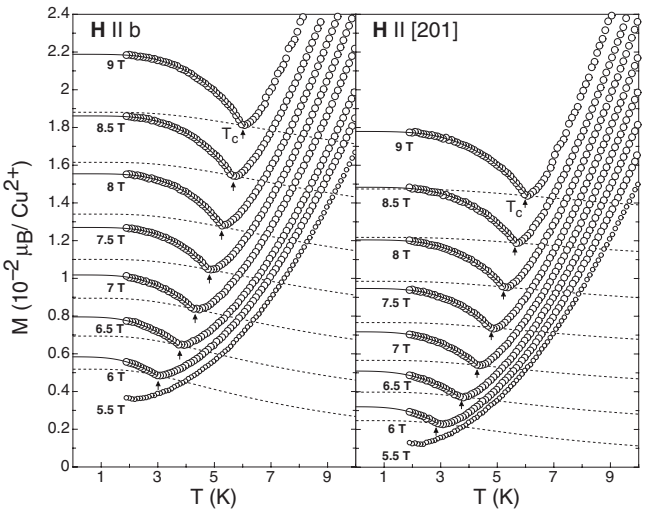

Abbildung 1.8: Magnetization of $TlCuCl_3$ parallel to the applied magnetic field as a function of the temperature. The solid lines are fits to Eq. 1.9 with a background contribution (dashed lines). The graphic is taken from Ref. [41].

occupation of the ground state that results in a nonzero longitudinal magnetization, as studied by Nikuni *et al.* and described above, gave a first indication that the observed phase transition of the triplons can be described as a BEC. Nevertheless, this indication alone is not sufficient to classify the observed phase transition of the magnetic subsystem as a true BEC.

Another important property of interacting BEC is the linear excitation spectrum (*Goldstone-Mode*) that results from the spontaneous breaking of the XY-symmetry as predicted by Boguliobov. A similar behavior has been theoretically predicted for $TlCuCl_3$ [44]. Using neutron scattering techniques, Rüegg et al. demonstrated that, inside their instrumental resolution, the excitation spectrum of the lowest triplon branch in the condensed phase is indeed linear [45]. However, according to Landau's argument given above, a linear excitation spectrum would give rise to superfluidity of the bosonic system.

As in the case of ^{4}He, a strong enhancement of the thermal conductivity should accompany this superfluidity. Kudo *et al.* [46, 47] have measured the thermal conductivity in $TlCuCl_3$ as a function of the temperature T and the magnetic field B, $\kappa(T, B)$. Their experiments showed that κ is not only temperature dependent as in a usual insulator, but also shows a dependence on the applied magnetic field. As the onset of the increase of κ coincides well with the reported phase boundary $T_c(B)$, they concluded that the increase in κ is due to the BEC state, as in ^{4}He. Unfortunately, the maximum field used in these experiments was too small to decide whether or not $\kappa(B)$ can exceed the zero-field contribution of the phonons alone. Moreover, in the spin system of the compound $Pb_2V_3O_9$, κ was found to generally *decrease* with increasing magnetic field. Only when

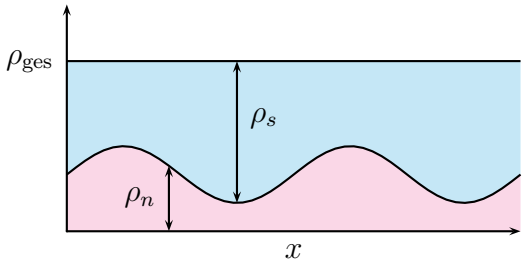

Abbildung 1.9: Sketch of the second sound as a oscillation of the densities of the superfluid (ρ_s) and the normal fluid (ρ_n) with a constant total particle density ρ_{ges}, here shown as a snapshot over a linear dimension x of the system.

measuring κ for certain crystal directions, a very small feature became visible [48] which bore, however, only small resemblance to the striking increase of κ in ^{4}He. As $Pb_2V_3O_9$ is another triplon BEC candidate, the reported behavior of κ is in strong contrast to the BEC picture [49].

Furthermore, it has been attempted to directly probe the superfluid properties by searching for corresponding magnetic resonances of the spin system [50]. The basic idea was to excite standing waves of the so called *second sound* mode. This mode is a direct consequence of the coexistence of superfluid and normal fluid and corresponds to their simultaneous oscillation with opposite phases, so that the superfluid density is decreased where the density of the normal fluid is increased and vice versa (see Fig.1.9). It is therefore not a density wave (the total density stays constant) but a temperature wave, where the temperature changes periodically in time and space. While the wave itself might not be detectable, the microwave absorption of the system should increase when the excitation frequency is in resonance with a standing wave. These resonant frequencies depend on the geometry of the examined sample and the sound velocity, given by the slope of the low energy dispersion relation $\omega(k)$, which is supposed to be linear (Goldstone-mode). As the linear dimensions of the samples are typically several mm and the sound velocity is of the order of 1000 $\frac{\text{m}}{\text{s}}$, the resonance frequencies should be on the order of 1 MHz. However, when examining the absorption spectrum of the sample in this frequency region, no clear sign of the above described resonances could be detected.

The heat capacity as well as the magnetocaloric effect have been studied for a number of materials that are supposed to show a triplon BEC [51, 52, 53, 36, 37]. These experiments confirm that the phase transition is of second order, as expected for a condensation of interacting bosons. However, apart from the order of the transition, neither direct evidence nor indication for a BEC can be drawn from this result.

Similarly, the magnetization can be used to examine the order of the phase transition. To the best of our knowledge, all examined triplon BEC candidates show a kink in the low temperature magnetization [54, 36, 37, 53, 38, 55, 39, 41] (see also section 3.11). The susceptibility is therefore not a continuous function, indicating a second order phase

transition as well.

However, when comparing the phase boundary $T_c(H)$ obtained by these different techniques, one observes an important discrepancy for some BEC candidate materials. The heat capacity C_V and the susceptibility χ are given as the second derivative of the Gibbs enthalpy G with respect to its natural variables T and B. As this enthalpy is a unique function $G(T, B)$, the phase boundary is also uniquely defined. Hence, it can not matter whether a critical point (T_c, B_c) is crossed by changing the temperature or the field or a combination thereof, as long as the chosen path $T(B)$ is not tangential to the phase boundary at this critical point. Any second derivative of G along this path must always show a discontinuity at (T_c, B_c). The heat capacity $C = -T\frac{\partial^2 G}{\partial T^2}$ has been shown to exhibit a corresponding jump upon entering the reported triplon BEC phase for all examined materials. The susceptibility $\chi = -\frac{\partial^2 G}{\partial B^2}$ can, e.g., be examined using the so-called *extraction magnetization* technique (see section 3.11). As stated above, the susceptibility χ should exhibit a discontinuity at exactly the same point (T_c, B_c) as the heat capacity C. This is indeed the case for some BEC candidates such as $TlCuCl_3$ and $KCuCl_3$ [56] or DTN [57, 42]. For other BEC candidate systems like $Ba_3Mn_2O_8$ [54] and $Sr_3Cr_2O_8$ [58, 59], the phase boundary obtained from the discontinuities in χ (as measured with the extraction magnetisation technique) and C does not coincide (see section 3.11). In principle, this could indicate that the observed transitions in $\chi(B, T)$ and $C_V(B, T)$ do not actually belong to the same subsystem for the latter materials, which may motivate the question whether it is really the spin system that shows a condensation.

As a true BEC transition results in a macroscopic wave function with a corresponding phase coherence, such a macroscopic phase should also exist in a triplon BEC. A system of spin dimers with interdimer interactions exhibits an ordering transition for low enough temperatures T and high enough magnetic fields B [60, 61]. For a visualization of this ordering one should think of the spin dimer system as being composed of two spin sublattices A and B such that one spin of every dimer belongs to subsystem A and the other spin belongs to subsystem B (see Fig. 1.10). Due to the ordering transition, the spins of each sublattice are aligned parallel to each other but antiparallel to the spins of the other subsystem. The direction of the spins with respect to the crystal host, given by an angle α between the spins and one of the crystal axes, is arbitrarily chosen if no anisotropy is present. The angle α is only meaningful for a long range order of the spin system, analogous to the macroscopic phase ϕ that can only be assigned for a macroscopic, coherent state. For the triplon BEC discussed in this work, the angle α is thus often seen as corresponding to the phase of the triplon condensate [62]. As the possibility to adopt an arbitrary value for this macroscopic phase of the condensate is one of the important prerequisites for the condensation itself ($U(1)$-symmetry of the system), the corresponding spin angle α should also be arbitrarily chosen upon entering the condensate regime. If, however, the value is the same for each condensation process, it is very likely that the system is anisotropic, inhibiting the formation of a BEC. It has been shown that the angle between the spins and the a-axis always takes a fixed value

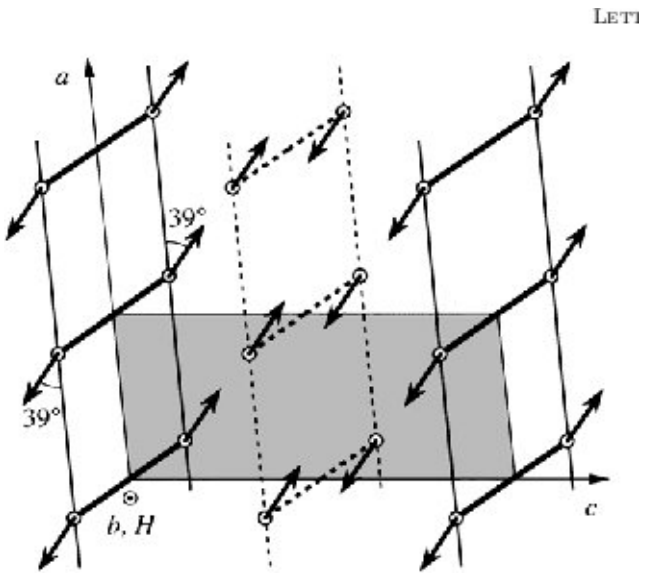

Abbildung 1.10: Sketch of the spin order in the *ac*-plane reported for $TlCuCl_3$. The ellipses enclose spins belonging to the same dimer. The solid and dashed lines mark spin chains in different planes (separated in the *b*-direction).

of $\alpha \approx 39°$ for $TlCuCl_3$ [31], making at least the analogy drawn between this angle and the phase of the condensate questionable.

The consequences of a spin anisotropy as mentioned above have been discussed with respect to the corresponding ESR spectra of the triplon system [63, 64] and the triplon condensation process itself [65], reporting clear but small corrections to the energy spectra and the specific heat. Dell'amore *et al.* have calculated that a small existing anisotropy γ that explicitly violates the axial symmetry leads to an anisotropy gap in the energy spectrum, so that no truly linear Goldstone mode can be present [34]. This gap would seriously limit the lifetime of the phase coherence in the condensate to the order of 1×10^{-9} s. A MHz-resonance experiment could therefore not excite such collective modes, possibly explaining why the expected characteristic magnetic resonances were not found in Ref [50](see above).

Furthermore, Dell'amore *et al.* showed that an anisotropy term actually lowers the total energy of the condensate, making an axial symmetry breaking energetically favorable even for systems with a perfect axial symmetry above the condensation point. Based on this energetic argument, *any* triplon-BEC system should show a spontaneous anisotropy and a corresponding *explicit* breaking of the $U(1)$-symmetry upon condensation, affecting the crystal structure in the process. The idea of a simultaneous structural transition is supported by the clear hysteresis observed in ultrasound attenuation [66] and thermal expansion experiments performed at the phase boundary for $TlCuCl_3$ [67] that indicate a first order contribution to the transition. Although providing an explanation for the locked spin angle in $TlCuCl_3$, the explicit violation of the axial symmetry would make

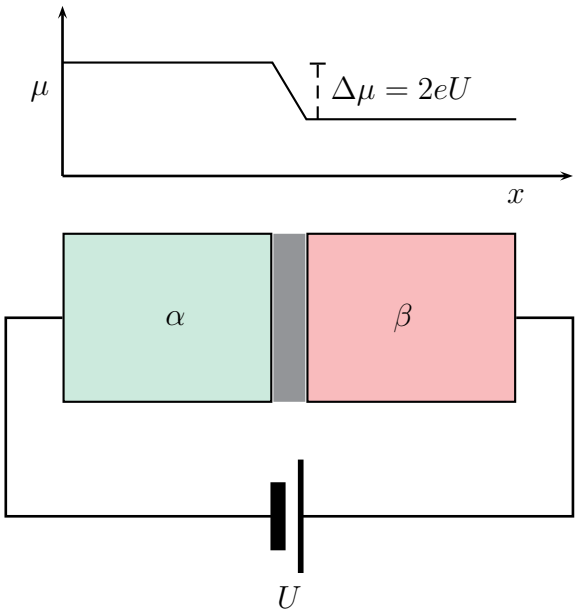

Abbildung 1.11: Sketch of a Josephson junction of two superconductors α and with an insulating barrier in between. The voltage U applied across the junction gives rise to the a.c. Josephson effect (see text).

the interpretation of the triplon phase transition as a BEC of quasiparticles at least questionable, since a true BEC requires perfect axial symmetry.

1.3 Josephson effects in magnetic insulators - a proposition

As discussed in the previous section, no concluding evidence that allows to unambiguously classify the phase transition of triplons as a BEC has yet been reported. In another attempt to probe the existence of a phase coherent state in these materials, we have suggested a new experimental scheme that bears close resemblance to the superconducting junctions used to demonstrate the existence of Josephson effects [68] which are based on the coherent state of the Cooper pairs in superconductors. Due to the smaller experimental time scale τ ($\tau \propto 1/\nu$ with frequencies ν in the range of GHz, see Fig. 1.13), this experimental scheme would probably be much less inhibited by the finite lifetime of the quasiparticles due to anisotropy effects than the search for magnetic superfluidity,

To explain the Josephson effects in weakly coupled superconductors, Feynman described the system by the macroscopic wave functions $\psi_j = \sqrt{n_j}e^{i\varphi_j}$ (with $j = \alpha, \beta$ for the two sides of the coupled device) that are weakly coupled to each other across a weak link (see Fig. 1.11). Here, n_j is the density of the condensed particles and φ_j is the phase of the

wave function. The weak coupling, described by a constant K, leads to a time-dependent change of the two condensates given by

$$i\hbar\frac{\partial}{\partial t}\psi_\alpha = \mu_\alpha\psi_\alpha + K\psi_\beta \tag{1.10}$$

$$i\hbar\frac{\partial}{\partial t}\psi_\beta = \mu_\beta\psi_\beta + K\psi_\alpha. \tag{1.11}$$

Here μ_α and μ_β denote the respective chemical potentials for the case of two isolated materials. The interaction is therefore considered as a small perturbation, $K << \mu_{\alpha;\beta}$. Inserting the above ansatz for the wave functions and dividing by $\sqrt{n_j}e^{i\phi_j}$ gives

$$\hbar\left(i\frac{\frac{\partial n_\alpha}{\partial t}}{2n_\alpha} - \frac{\partial\varphi_\alpha}{\partial t}\right) = \mu_\alpha + K\sqrt{\frac{n_\beta}{n_\alpha}}e^{i\varphi_\beta-\varphi_\alpha}$$

$$\hbar\left(i\frac{\frac{\partial n_\beta}{\partial t}}{2n_\beta} - \frac{\partial\varphi_\beta}{\partial t}\right) = \mu_\beta + K\sqrt{\frac{n_\alpha}{n_\beta}}e^{i\varphi_\alpha-\varphi_\beta}.$$

As the real part and the imaginary part do not mix, we arrive at four equations:

$$-\frac{\partial\varphi_\alpha}{\partial t} = \frac{\mu_\alpha}{\hbar} + \frac{K}{\hbar}\sqrt{\frac{n_\beta}{n_\alpha}}\cos\left(\varphi_\beta-\varphi_\alpha\right) \tag{1.12}$$

$$\frac{\frac{\partial n_\alpha}{\partial t}}{2n_\alpha} = \frac{K}{\hbar}\sqrt{\frac{n_\beta}{n_\alpha}}\sin\left(\varphi_\beta-\varphi_\alpha\right) \tag{1.13}$$

$$-\frac{\partial\varphi_\beta}{\partial t} = \frac{\mu_\beta}{\hbar} + \frac{K}{\hbar}\sqrt{\frac{n_\alpha}{n_\beta}}\cos\left(\varphi_\alpha-\varphi_\beta\right) \tag{1.14}$$

$$\frac{\frac{\partial n_\beta}{\partial t}}{2n_\beta} = \frac{K}{\hbar}\sqrt{\frac{n_\alpha}{n_\beta}}\sin\left(\varphi_\alpha-\varphi_\beta\right).$$

Introducing the phase difference $\Delta\varphi = \varphi_\alpha - \varphi_\beta$, we can summarize these to:

$$\frac{\partial n_\alpha}{\partial t} = -\frac{\partial n_\beta}{\partial t} = \frac{2K}{\hbar}\sqrt{n_\alpha n_\beta}\sin\left(\Delta\varphi\right) \tag{1.15}$$

$$\frac{\partial\Delta\varphi}{\partial t} = \frac{\mu_\alpha-\mu_\beta}{\hbar} - \frac{K}{\hbar}\frac{n_\alpha-n_\beta}{\sqrt{n_\alpha n_\beta}}\cos\left(\Delta\varphi\right). \tag{1.16}$$

In the usual example of two superconductors, the two sides of the junction are assumed to be made of the same material so that $n_\alpha = n_\beta$. The difference of the chemical potentials is then given by a voltage U that is applied across the junction, $\mu_\alpha - \mu_\beta = 2eU$. In that case, the phase difference will increase linearly with time. According to Eq. 1.15 such an increase should lead to an oscillation of the densities of the charge carriers. The electrodes that are connected to the two superconductors to maintain the voltage difference will act as a sink or source for the electrons that cross the junction, keeping the total density constant on both sides [69] so that no change of these densities can

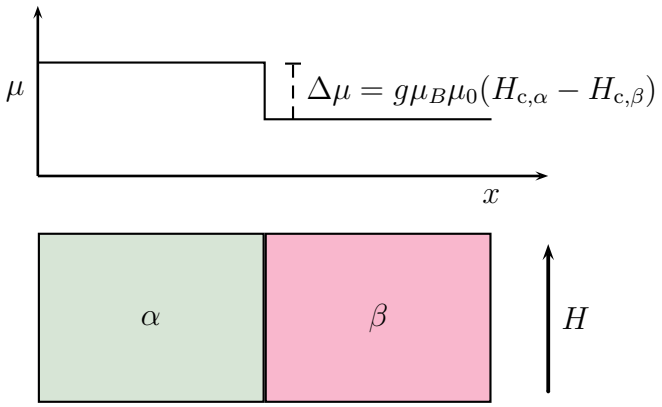

Abbildung 1.12: Sketch of a Josephson junction of two magnetic insulators α and β. The applied external magnetic field H should give rise to Josephson effects once it exceeds the critical fields H_c of both insulators (see text).

be detected. However, the resulting alternating current can be measured experimentally [70, 71] (a.c. Josephson effect).

In the case of the triplon BEC discussed in the last section, one can think of a similar device consisting of two dimerized spin systems coupled by a weak link (see Fig. 1.12). Again introducing K as a phenomenological coupling constant we can use the same equations to describe the time evolution of the wave functions of the triplon BEC as in the case of a superconducting junction (Eqs. 1.10 and 1.11). The chemical potential is here not given by an applied voltage, but by the external magnetic field that induces the triplon phase transition. To be specific, $\mu_{\alpha;\beta} = g_{\alpha;\beta}\mu_B\mu_0(H - H_{\alpha;\beta})$ [40], where g is the Landé factor for the crystal direction that is parallel to the external field H and μ_B is the Bohr magneton. $H_{\alpha;\beta}$ denotes the critical field of the respective triplon systems so that the chemical potential is actually given by the *excess* of the external field compared to the critical field for the triplon BEC.

For the wave functions, we introduce the same ansatz as for the superconducting junction, $\psi_j = \sqrt{n_j}e^{i\phi_j}$. The equilibrium density n_j of the respective isolated condensates is given by $n = \mu/\nu_0$ [72], where ν_0 is then the effective hard-core between the triplons introduced in the last section. The result is then formally equivalent to Eqs. 1.15 and 1.16.

Again, the density oscillation $n(t)$ cannot be detected directly. In principle, the particle density can change in the same way in which the triplons "move" - via *hopping* from one dimer site to another, e.g. triplon excitation at the new site and triplon decay at the original site. In that sense, a density oscillation would consist of decay of triplons on one side of the junction and corresponding excitation on the other side. However, in analogy to the external voltage applied to the superconducting junction, the applied magnetic field will act as a source or sink for the quasiparticles, keeping the density constant on

each side. The alternating current that can be assigned to the spacer between or the interface of the two spins systems is most probably virtual and can not be detected, contrary to the a.c. current of coupled electrons in the superconducting junction.

However, the time evolution of the phase would have some important implications. To analyze them more easily, we assume that $g_\alpha = g_\beta = g$ and $\nu_\alpha = \nu_\beta = \nu_0$. The former is relatively well justified, as g is around 2 for most of the triplon BEC candidates. Note that even if these assumptions are not met exactly, the results of the analysis would only change qualitatively, not quantitatively. Furthermore, we will assume a homogeneous magnetic field H into which the junction is placed so that the magnetic field is the same for both materials. We can then rewrite Eqs. 1.17 and 1.18 as:

$$-\frac{\partial \varphi_\alpha}{\partial t} = g\mu_B\mu_0 \frac{H - H_\alpha}{\hbar} + \frac{K}{\hbar}\sqrt{\frac{n_\beta}{n_\alpha}}\cos\left(\varphi_\beta - \varphi_\alpha\right) \tag{1.17}$$

$$-\frac{\partial \varphi_\beta}{\partial t} = g\mu_B\mu_0 \frac{H - H_\beta}{\hbar} + \frac{K}{\hbar}\sqrt{\frac{n_\alpha}{n_\beta}}\cos\left(\varphi_\alpha - \varphi_\beta\right). \tag{1.18}$$

To interpret the time evolution of the phases dictated by Eqs. 1.17 and 1.18, we will introduce a momentary frequency, $\omega_j = \frac{\partial}{\partial t}\varphi_j$. For $K = 0$ this momentary frequency would determine the excitation energy $\hbar\omega_j = \mu_j$ needed to excite a dimer out of the condensate into the intermediate non-condensed triplet state. The reference point would then be the respective excitation energy at the critical field, $\hbar\omega_j = g\mu_B\mu_0\left(H - H_j\right)$. As K is very small, this description holds also to first approximation for coupled systems ($K \neq 0$).

To second order approximation, the momentary frequencies take the form:

$$\omega_{\alpha;\beta} = \frac{g\mu_B\mu_0}{\hbar}\left(H - H_{\alpha;\beta}\right) - \frac{K}{\hbar}\sqrt{\frac{n_{\beta;\alpha}}{n_{\alpha;\beta}}}\cos\left(\frac{g\mu_B\mu_0}{\hbar}\left(H_\beta - H_\alpha\right)t + \varphi_0\right),$$

describing a time variation of the momentary frequency ω_j (a.c. Josephson effect). This situation is an analogue to the frequency modulation of a radio signal. Such a modulation alters the frequency spectrum of the system, as shown in Fig. 1.13. Additional peaks should appear in this spectrum with a separation that corresponds to the difference of the chemical potentials, $\Delta\mu = g\mu_B\mu_0\left(H_\beta - H_\alpha\right)$ (see Fig. 1.13). This process can be understood in terms of tunneling of triplons from one side of the junction to the other. As mentioned above, this tunneling corresponds to a periodic annihilation of a triplon on one side of the junction and the simultaneous creation of a triplon on the other side. This process requires the absorption/emission of the corresponding energy difference $\Delta\mu$ depending on whether the triplon tunnels from the side with lower μ to that with a higher μ or vice versa. Such a one-triplon tunneling would then give the first side band in the energy spectrum.

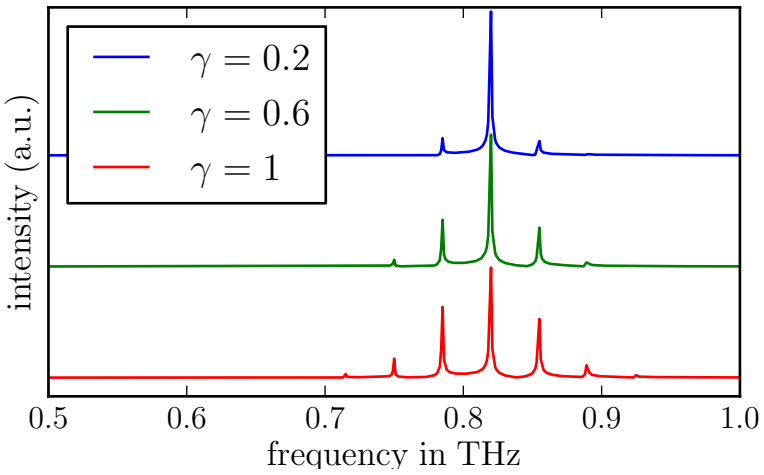

Abbildung 1.13: Sketch of the sidebands that appear in the Fourier spectrum according to Eq. 1.3. The parameter γ is given by $\gamma = \frac{K}{\Delta\mu}\sqrt{\frac{n_{\beta;\alpha}}{n_{\alpha;\beta}}}$. The difference $\Delta\mu$ of the chemical potentials is given by the critical fields $H_\alpha = 30.5\,\mathrm{T}$ and $H_\beta = 29.2\,\mathrm{T}$ and $g = 1.94$.

The additional peaks can only be present if both sides of the device are in their respective BEC state with macroscopic phases ϕ of the respective wave functions. The effect could therefore be suppressed by increasing the temperature, driving the triplon systems out of the condensation region. In a high frequency ESR experiment with a high resolution, the energy spectrum of the system can be probed, making it valuable technique to study the possible occurence of additional peaks in the frequency spectrum (see chapter 4).

2 Experimental Techniques

This chapter is devoted to descriptions of the experimental equipment used during the course of this thesis. The most important experimental techniques were magnetization measurements, structural examinations based on powder diffraction, and electron spin resonance experiments. The following sections contain the most important specifications of these techniques with details concerning the used sub-categories.

2.1 Magnetization experiments

As electronic spins are related to magnetic moments, one of the key techniques to spin dimer physics is to probe the magnetization, either locally (neutron scattering, muon spin rotation, ESR/NMR) or as a bulk property. The latter is connected with a total magnetic moment m of the sample that can be measured as a function of external parameters such as the magnetic field H or the sample temperature T. For the spin dimer systems discussed in this work, both measuring the magnetization $M(H)$ at high magnetic fields up to 65 T and $M(T)$ in medium fields up to 1 T yielded important information about the interactions within and between the dimers.

2.1.1 Measuring M(T) in low magnetic fields

The magnetic moment of a sample is usually detected by moving the sample inside a pick-up coil system. For this work, a *QuantumDesign* MPMS (Magnetic Properties Measurement System) was used to determine the dependence of the magnetic moment m of the sample on the temperature T. The MPMS is equipped with a SQUID (Superconducting Quantum Interference Device) that allows to obtain the total moment even for small powder samples with a high sensivity. This sensitivity is usually better than the relative uncertainty of the obtained corresponding sample mass ($\sigma_M/M \approx 1\,\%$). The weighted samples where placed in a non-magnetic sample holder made from plastic and inserted into the MPMS. After purging the sample space several times with He-gas to ensure a very low oxygen content, a low pressure He-atmosphere was maintained to allow for a sufficient thermal contact between the sample and the thermal bath of the MPMS.

Magnetization data were analyzed by approximating the sample as a magnetic dipole and fitting the SQUID-signal accordingly. For our experiments, we were mostly interested in changes of the magnetization as a function of the temperature and not its absolute magnitude. Subsequently, no demagnetization factors were taken into account to simplify the data analysis.

2.1.2 Measuring M(H) in high magnetic fields

The high field magnetometry experiments have been performed at the High Magnetic Field Laboratory in Dresden-Rossendorf (HZDR). The high magnetic fields are achieved by discharging a capacitor with a stored electrical energy of typically about $E = 20\,\mathrm{MJ}$ through a coil that is specifically designed for this purpose (see Fig. 2.1). The quick discharge leads to a high current in the coil, inducing fields of up to $B_{\max} \approx 100\,\mathrm{T}$ (in this work the maximum used field was $B_{\max} = 65\,\mathrm{T}$). This rapidly changing field induces a characteristic voltage pulse U_B in the main pickup coil.

Similarly, the magnetization of the sample changes with time and thus induces a voltage U_M in the sample pickup coil. To remove the main field contribution, a compensation coil identical to the sample pickup coil is used. Reversing the connection then gives the opposite signal so that the main field contribution is canceled out. Finally, a potentiometer is used to fine tune the compensation as the two pickup coils will in reality never produce *exactly* the same signals.

The experimental signals also show a background signal stemming from the cryostat itself that is only slightly temperature dependent. To deal with this problem, a background pulse without a sample is measured with the same pulse characteristics (pulse duration, maximum field) that are applied for the sample measurements.

Integration of the voltage signals over time and applying a calibration factor yield the absolute field and magnetization as a function of time. As explained in section 3.11, we are primarily interested in the second derivative of the magnetization. For this, we first calculate the susceptibility

$$\chi = \frac{\partial}{\partial B} M \propto \frac{U_M}{U_B}.$$

From that, we obtain the second derivative $\rho = \frac{\partial^2}{\partial B^2} M$ as

$$\rho = \frac{\partial \chi}{\partial B} \approx \frac{\Delta \chi}{\Delta B} = \frac{\Delta \chi}{U_B \Delta t} \propto \frac{\Delta \chi}{U_B},$$

where $\Delta\chi$ is the difference between consecutive values of χ and Δt is the (constant) time difference between consecutive measurements.

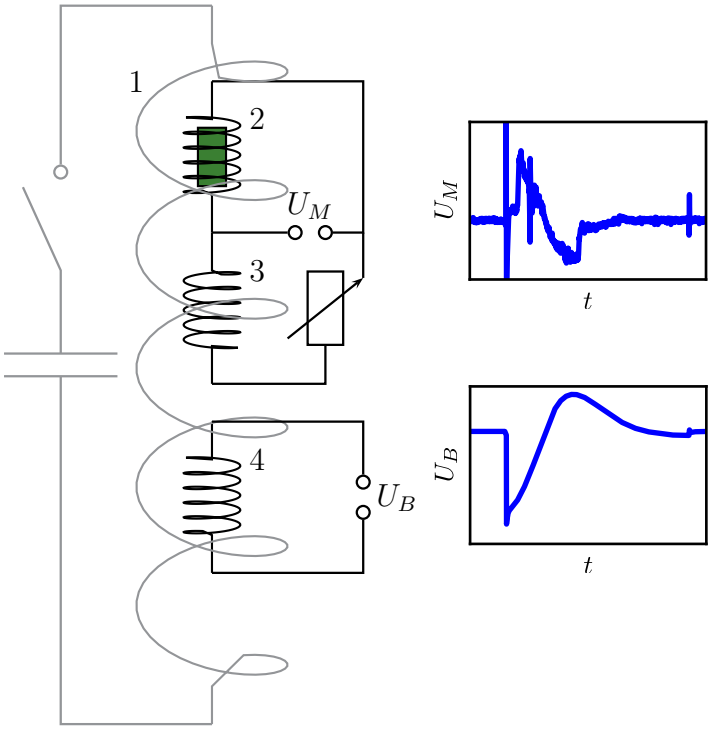

Abbildung 2.1: Sketch of the principle of pulsed field magnetometry (see text). 1: Main coil (with capacitor and switch), 2: Pickup coil (with sample in green), 3: Compensation coil (with potentiometer), 4: Pickup coil for main field. The plots on the right side show the voltages in the main pickup coil (lower graph) and the sample pickup coil (upper graph) as a function of time.

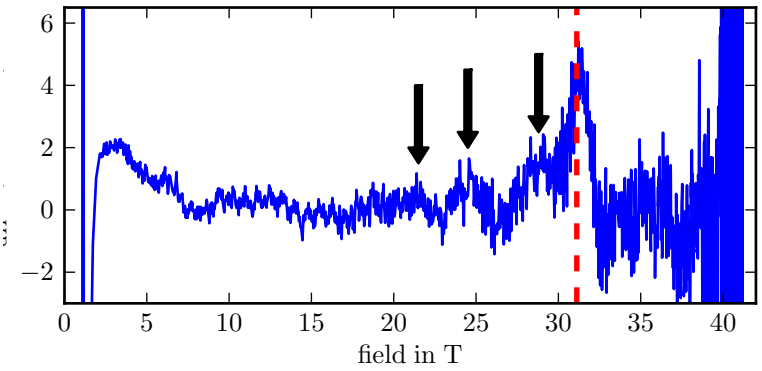

Abbildung 2.2: Example of a measurement of the second derivative of the magnetization $\frac{\partial^2 M}{\partial B^2}$ with signal disturbance due to a nonzero torque (marked with arrows, see text). The obtained critical field is marked by the dashed red line.

For our experiments, the polycrystalline samples were ground and inserted into a Teflon tube with a diameter of about 1 mm. This tube was closed with non-magnetic wooden stoppers at both ends that compressed the powder to inhibit vertical movement due to the pulsed magnetic field. However, due to an experimental problem a few weeks prior to our measurements, it was not possible to perfectly center the sample in the magnet. Therefore, the transversal magnetic forces were not zero, leading to a small torque on the sample holder. For some pulses, this torque resulted in slight oscillations in the susceptibility signal. This disturbance of the signal could not be removed so that the signal had to be interpreted very carefully to find the desired features and to not misinterpret these oscillations as the magnetic phase transition (see Fig. 2.2).

This pulsed field magnetometry technique is often referred to as *extraction magnetization technique*.

2.2 Powder diffraction techniques

The structural details on $Ba_{3-x}Sr_xCr_2O_8$ presented in this work have been obtained using powder samples. The reasons for this are twofold. First, single crystalline samples of sufficient quality have not been prepared to date for samples with $0 < x < 3$. Second, as $Ba_3Cr_2O_8$ and $Sr_3Cr_2O_8$ are isostructural, only gradual changes in the crystal structure have been anticipated. A complete re-characterization including single crystal diffraction to deduce the crystal symmetries from scratch was not expected to be required. Our experimental plan therefore only included the determination of the slightly changed atomic positions and the correct subgroup with respect to the room temperature structure.

The underlying principle of X-ray and neutron diffraction techniques is similar. A sample is irradiated with monochromatic neutrons or X-ray photons with a certain wave length λ, corresponding to an incident wave vector $\vec{K} = \frac{2\pi}{\lambda}\vec{e}_{\text{in}}$. The interaction with the sample leads to a scattering of the probing particles (neutrons or X-ray photons). Measuring the scattered intensity gives a non-zero value (a reflection) only for those outgoing wave vectors $\vec{K}_{\text{out}}$ that obey the Laue condition $\vec{K}_{\text{out}} - \vec{K}_{\text{in}} = \vec{G}$, where $\vec{G} = h\vec{b}_1 + k\vec{b}_2 + l\vec{b}_3$ is a reciprocal lattice vector of the examined sample. As this work mostly deals with powder diffraction, we can use the Bragg condition $n\lambda = 2\frac{2\pi}{\left\|h\vec{b}_1+k\vec{b}_2+l\vec{b}_3\right\|}\sin\frac{\theta}{2}$ for the scattering angle θ.

2.2.1 Structure factor

The Laue condition only gives the possible positions for reflections, and makes no prediction about the respective intensity. The intensity of a given reflection (hkl) is given by the structure factor [73]

$$F_{hkl} = \int n\left(\vec{r}\right) e^{i\vec{G}\vec{r}} \mathrm{d}^3 r, \tag{2.1}$$

where $n\left(\vec{r}\right)$ is the density of the scatterer and the integral is calculated over one direct unit cell. In the case of neutrons, $n\left(\vec{r}\right)$ would be the density of the nuclei (or spins, for periodic magnetic structures), whereas in the case of X-ray radiation $n\left(\vec{r}\right)$ is the electronic density. To take this into account, we rewrite Eq. 2.1 in terms of the positions of the base atoms at positions $\vec{r}_i$ measured from a reference point $\vec{0}$,

$$\begin{aligned} F_{hkl} &= \sum_i \int n_i\left(\vec{R}\right) e^{i\vec{G}\left(\vec{r}_i+\vec{R}\right)} \mathrm{d}^3 R \\ &= \sum_i e^{i\vec{G}\vec{r}_i} \underbrace{\int n_i\left(\vec{R}\right) e^{i\vec{G}\vec{R}} \mathrm{d}^3 R}_{f_i}, \end{aligned} \tag{2.2}$$

where f_i is then the form factor of the i-th atom which can be thought of as the Fourier transform of the density of the scatterer. As the intensity I_{hkl} is proportional to the squared structure factor, $I_{hkl} \propto |F_{hkl}|^2$, Eq. 2.1 shows that symmetries in $n\left(\vec{r}\right)$, given by atoms highly symmetric positions, can lead to the suppression of reflections. Gradual shifts of atoms out of these symmetric positions, on the other hand, result in a gradual appearing of reflections that were forbidden before. The intensity of these reflections can therefore be taken as a measure of the symmetry breaking - the larger the deviation from the symmetric case, the larger the measured intensity.

2.2.2 Debye-Waller factor

The form factor described in the previous section is based on a static lattice. In a real material, deviations $\vec{u}_i$ from the ideal (equilibrium) atomic positions $\vec{r}_i$ occur due to atomic movement or random static displacements over the whole crystal. We therefore have to introduce the averaged value of the structure factor,

$$\begin{aligned}\langle F\rangle_{hkl} &= \sum_i \left\langle e^{i\vec{G}(\vec{r}_i+\vec{u}_i)} f_i \right\rangle \\ &= \left(\sum_i e^{i\vec{G}\vec{r}_i} f_i\right) \left\langle e^{i\vec{G}\vec{u}_i} \right\rangle .\end{aligned}$$

The last factor, only depending on the scattering vector $\vec{G}$ and the atomic displacements, is the *Debye-Waller factor*. It describes the intensity reduction of a given reflection due to these atomic displacements.

It should be noted that, up to now, the type of displacement is not stated. Displacements due to thermal energy (phonons), $\langle u_T\rangle$, would require a time average, while displacements due to chemical disorder, $\langle u_D\rangle$, would require a spacial average over the whole crystal. If we assume the respective contributions to the atomic displacements to be independent from each other, we can write:

$$\langle F\rangle_{hkl} = \left(\sum_i e^{i\vec{G}\vec{r}_i} f_i\right) \left\langle e^{i\vec{G}\vec{u}_{Di}} \right\rangle \left\langle e^{i\vec{G}\vec{u}_{Ti}} \right\rangle .$$

The thermal part can be evaluated using the harmonic approximation to [74, 75]

$$\left\langle e^{i\vec{G}\vec{u}_T} \right\rangle = e^{-\frac{1}{2}\left\langle \left(\vec{G}\vec{u}_T\right)^2 \right\rangle}.$$

Similarly, we can evaluate the disorder part, if we assume that $\vec{u}_D$ obeys a normal distribution that is centered around zero for every spacial direction, and the average becomes [76]

$$\left\langle e^{i\vec{G}\vec{u}_D} \right\rangle = e^{-\frac{1}{2}\left\langle \left(\vec{G}\vec{u}_D\right)^2 \right\rangle}.$$

As each of the different types of displacements reduces the intensity in an analogous way, it is not possible to distinguish between those two contributions without further assumptions for a given compound. Any mean square displacement $\langle u^2\rangle$ obtained from refinements of diffraction data therefore results in a combination:

$$I_{hkl} \propto \langle F\rangle^2_{hkl} = \left(\sum_i e^{i\vec{G}\vec{r}_i} f_i\right)^2 e^{-\left\langle \left(\vec{G}\vec{u}\right)^2 \right\rangle} \qquad (2.3)$$
$$\text{with } \left\langle u^2 \right\rangle = \left\langle u_T^2 \right\rangle + \left\langle u_D^2 \right\rangle .$$

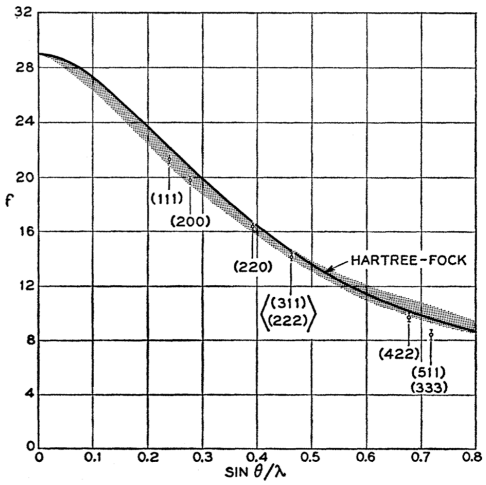

Abbildung 2.3: Experimental form factors for X-ray scattering on iron copper (graph taken from [77]).

However, the mean square displacement of an harmonic oscillator is anti-proportional to its mass. When replacing an atom with a lighter one, the Debye-Waller factor should therefore increase monotonously. This is not true for the disorder contribution for a gradual replacement of one sort of atoms by another in a solid solution. In the latter case, the mean square displacement should be given by the number of possible atom arrangements in a unit cell and should therefore be maximum for similar concentrations of the two sorts of atoms in the material. In principle, it should be possible to separate the disorder contribution from the thermal part by varying the temperature in additional diffraction experiments. However, as experimental time is always limited in the case of neutron diffraction, this approach was not a feasible option during this work.

2.2.3 X-ray powder diffraction

As stated above, X-ray diffraction probes the Fourier transform of the electronic density of a given material. Although the latter is strongly related to the atomic arrangement in a crystal, it has important implications on the sensitivity of the method. Firstly, the scattered intensity decreases for higher scattering angles (see Fig. 2.3). According to Eq. 2.3, the higher the scattering angle, the stronger the influence of the Debye-Waller factor is. Therefore the sensitivity on the mean square displacement is small for X-ray diffraction. Secondly, atoms with small electron numbers give only a small contribution to the total scattering intensity. The sensitivity on the position of oxygen atoms ($Z_{\mathrm{O}} = 8$) is reduced in comparison to the case of barium atoms ($Z_{\mathrm{Ba}} = 56$) by a factor of $\frac{Z_{\mathrm{O}}^2}{Z_{\mathrm{Ba}}^2} = 0.02$. Small changes in the position of light atoms, although important to the total electronic system, will therefore be virtually invisible to non-resonant X-ray diffraction.

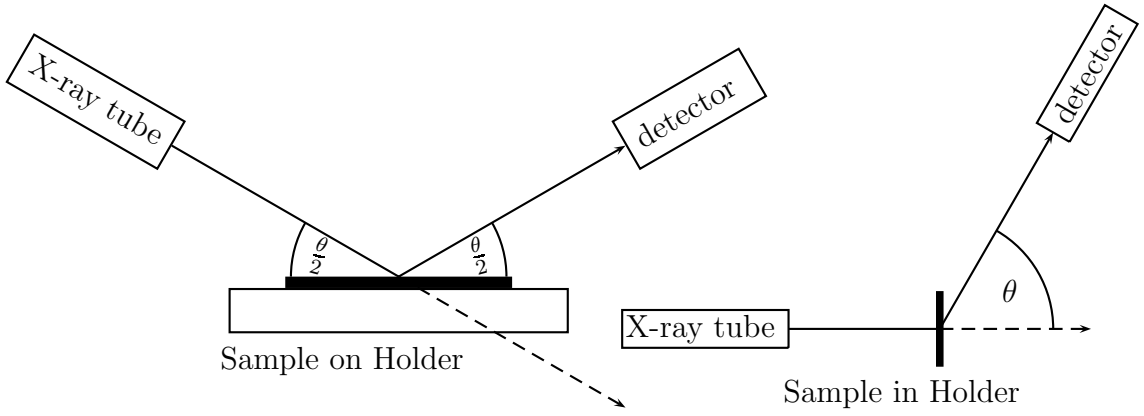

(a) Bragg-Brentano geometry (θ-θ-conf.) (b) Debye-Scherrer geometry

Lastly, the small penetration depth of a few hundred Å for X-ray photons leads to an increased sensitivity to the surface of a sample. Impurities that form on the surface (e.g. due to humidity or edge effects), will be a much more relevant part of the diffractogram than the bulk of the sample. Nevertheless, high quality X-ray sources are readily available even on a small laboratory scale. Furthermore, X-ray photons are easily manipulated and efficiently detected using, e.g. a CCD camera. The high flux of even a standard source allows to strongly collimate the probing beam, drastically increasing the resolution with still reasonable total counting times. These advantages make X-ray diffraction an important tool to access the structure and purity of a (crystalline) scientific sample sample, especially in combination with neutron diffraction techniques.

During this work, two types of diffractometers were used: the *Bruker AXS D8 Advance* and the *Stoe IPDS*. The *Bruker AXS D8 Advance* (used at Paul-Scherrer-Institute, Villigen) operates in the Bragg-Brentano geometry (see Fig. 2.4a). In our case, the powdered sample is fixed on a plane horizontal holder using Vaseline. This helped to overcome problems of preferred crystallite orientation. The latter occurred when leaving the sample unfixed or preparing a homogeneous mixture of sample powder and ethanol that was deposited on the sample holder in a thin film and left to dry.

For controlling the purity and obtaining the lattice constants, X-ray diffraction experiments were carried out using the *Stoe IPDS* at the University of Zürich. This system operates in the Debye-Scherrer geometry (see Fig. 2.4b). Using this diffraction geometry, a high degree of accuracy can be achieved concerning the reflection positions, leading to a good sensitivity with respect to the lattice parameters. However, as the diffracted X-ray photons have to be transmitted through the sample and the scotch tape sample holder after scattering, they are subject to inelastic scattering and absorption. This absorption leads to an additional decrease of the intensity for higher scattering angles which strongly decreases the sensitivity to the atomic coordinates (which are obtained from the relative peak intensities). Thus, the thereby refined atomic positions will not presented in this work (neither from the Debye-Scherrer nor the Bragg-Brentano geometry), apart

from estimates for the dimer length.

2.2.4 Neutron powder diffraction

In terms of crystal structure determination, neutron diffraction is not sensitive to the electronic density, but to the neutron scattering length b. As the value of b is given by the interaction between the neutron and the atomic core, it depends not only on the type of the considered atom, but also on the specific isotope. In the case of, e.g., ^{132}Ba the scattering length is $b = 7.8\,\mathrm{fm}$, while for ^{135}Ba, $b = 4.67\,\mathrm{fm}$, a relative difference of 67 % [78]. As no mono-isotopic chemicals were used, the scattering lengths are automatically weighted according to their natural abundance. As the average scattering length for oxygen ($b = 5.803\,\mathrm{fm}$) is comparable to that of Ba ($b = 5.07\,\mathrm{fm}$), Sr ($b = 7.02\,\mathrm{fm}$) and Cr ($b = 3.635\,\mathrm{fm}$), the sensitivity of our neutron scattering experiments with respect to the oxygen positions is much higher than in the case of X-ray diffraction.

As the neutrons are only weakly interacting with the sample, the entire sample volume is probed, making surface impurities and grain size of the sample powder much less important. Although the detection efficiency of the ^{3}He-gas detection chambers is higher than 75 % for thermal neutrons [79], the weak interaction between the incoming neutrons and the crystal atoms leads only to a small number of scattered neutrons and makes long counting times of several hours necessary to achieve sufficient statistics.

The neutron powder diffraction experiments for this work were carried out at the HRPT at PSI (Paul-Scherrer-Insitut, Villigen, Switzerland) [80]. The setup is depicted in Fig. 2.4. The neutron beam produced by the SINQ spallation source is narrowed by the collimator α_1 before arriving at the Si-filter. This filter, cooled with liquid N_2 removes high energy neutrons which would lead to an additional background for the diffraction experiment if not removed. Thermal neutrons have a much lower interaction probability with the cooled Si so that the filter remains almost transparent for neutrons in the relevant energy range. After the filter, a monochromator made of Ge-single crystals is used to choose a specific neutron wave length λ for the diffraction experiment. This monochromation is based on diffraction of the neutron beam on the Ge crystals. The monochromator angle is chosen so that a specific Bragg reflection is located directly between the outgoing slits. Due to the crystal symmetry of Ge, it is possible to remove neutrons with $\frac{\lambda}{2}$ by choosing a reflection hhl with h and l both odd or even. As the possible higher energy contributions ($\frac{\lambda}{3}$,$\frac{\lambda}{4}$...) are effectively filtered out before arriving at the monochromator, the neutron beam arriving at the sample can be regarded as pure. Thus, only one wave length had to be taken into account for the structural refinement of the obtained diffraction data. To further increase the signal-to-noise ratio, an oscillating radial collimator around the sample position is used. This additional collimator effectively removes any contribution of the sample environment (cryostat etc.) to the detected neutron signal.

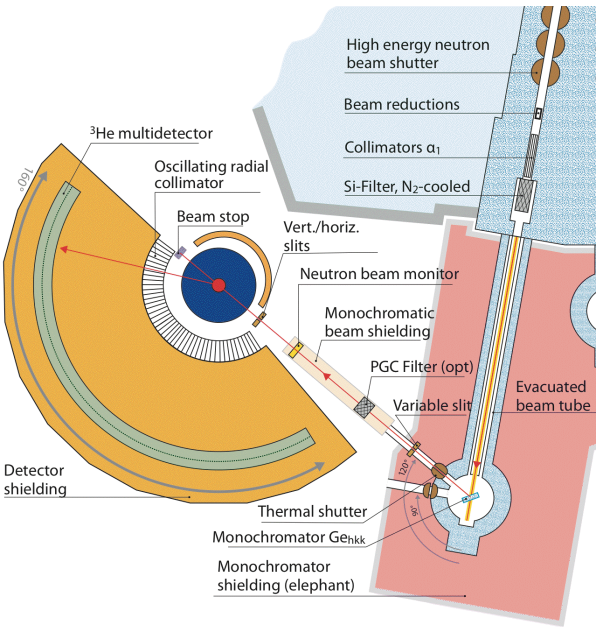

Abbildung 2.4: Schematic view of the HRPT powder diffraction setup, taken from *http://sinq.web.psi.ch/hrpt*.

The setup operates in the Debye-Scherrer geometry, which poses no problems concerning absorption effects as compared to X-ray diffraction due to the weak scattering probability of the neutrons. As described below, the experiments were performed at room temperature and at $T = 2\,\mathrm{K}$, using $\lambda = 1.494\,\text{Å}$ (given by the {533} reflection of the Ge monochromator). Although this wave length results in an intermediary resolution as compared to $\lambda = 2.45\,\text{Å}$ and $\lambda = 1.15\,\text{Å}$(see Fig. 2.5), the achieved neutron flux was five times higher than in the case of the optimal resolution, greatly reducing the counting time and total counts for the experiments. Scans were performed with fixed primary soller collimation (40') and a secondary slit of (40'). The powder samples ($\approx 6\,\mathrm{g}$) were loaded into cylindrical vanadium containers of 8 mm diameter (6 mm for $Ba_{\frac{8}{3}}Sr_{\frac{1}{3}}Cr_2O_8$). The low temperature measurements were performed using a standard PSI He cryostat.

2.2.5 Rietveld analysis

The powder patterns obtained from X-ray and neutron diffraction were analyzed using the *FullProf* package[1]. This method works by calculating a complete diffraction pattern for the sample material and comparing this simulated pattern to the experimental pattern. The calculation takes into account the expected crystal structure, impurities, the incoherent background, the form and width of the diffraction peaks (we used a pseudo-Voigt profile), slight sample displacements and several other factors that are controlled

[1] Available free of charge at http://www.ill.eu/sites/fullprof/.

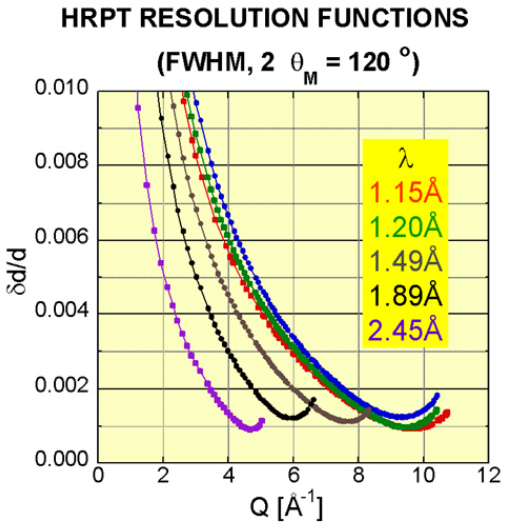

Abbildung 2.5: Resolution function for the wave length available at HRPT, taken from *http://sinq.web.psi.ch/hrpt*.

by fitting parameters. Although the number of free parameters can easily be greater than 60, the high number of actual data points (about 3200 per pattern) prevents these parameters from losing their significance in most cases (as opposed to the *fitting-an-elephant* problem).

Although the fitting routine itself is automatic, the fitting of a new pattern has to be approached step-by-step. First one should introduce only the most important parameters (background, total intensity, lattice parameters of the main phase) before refining atomic positions etc.. This increases the probability of the found set of parameters to really give the global instead of a local minimum in the programs residual function. However, as seen in the next chapter, the quality of a fit varies strongly between different diffractograms concerning one respective parameter, even for the same compound.

2.3 Electron spin resonance experiments

Electron spin resonance experiments are based on measuring the absorbtion/transmission of microwave radiation for a given sample. The frequency ν of the microwave radiation ranges from about 9 GHz (X-band ESR) to more than 2 THz (typically provided by free electron laser facilities such as *ELBE* in Dresden). In most cases, an external magnetic field is applied to separate electronic states by Zeeman splitting, or just to lower the respective energies, making them accessible through available microwave frequencies. The magnets used for these experiments provide fields in the range of 1 T (X-Band

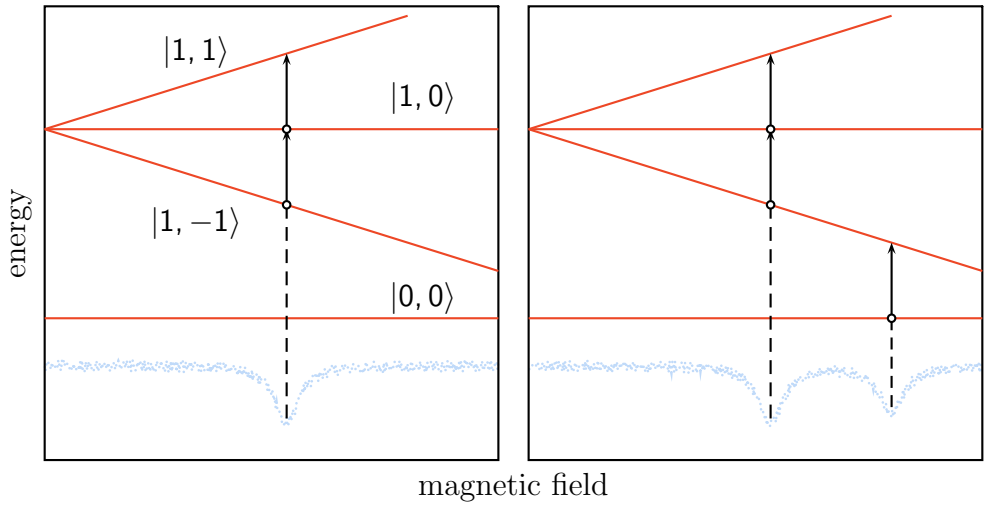

Abbildung 2.6: Possible ESR excitations for an isotropic spin-Hamilton operator (left) and for the anisotropic case (right) and the corresponding ESR transmission as a function of the magnetic field (bottom).

ESR) to over 60 T (pulsed magnetic fields).

In the case of the dimer systems examined in the work, the Zeeman splitting affects the triplet level, separating the three degenerate states with $S = 1$ (see Fig. 2.6). For a given microwave frequency ν, the Zeeman splitting energy between $|1, -1\rangle$ and $|1, 0\rangle$ ($|1, 0\rangle$ and $|1, 1\rangle$) due to the external magnetic field B leads to a resonant absorption as soon as $h\nu = g\mu_B B$. Generally, both excitations require the same energy, resulting in a single absorption line with a field value that is given by the Landé g-factor. Usually, this resonance line will be the only one detectable by ESR as the singlet-triplet transitions would require a change of the total spin from $S = 0$ to $S = 1$, which is forbidden by photon absorption as the total spin can not be changed by pure dipole radiation. Under certain conditions, like the occurrence of anisotropy terms in the spin-Hamilton operator, however, the singlet and triplet state can be mixed. Transitions between these new eigenstates can then be excited with microwave radiation, leading to additional resonance lines (see Fig. 2.6).

To describe the absorbed microwave power P as a function of the applied magnetic field B, a Lorentzian lineshape was used during this work:

$$P(B) \propto \frac{1}{1 + \left(\frac{B - B_0}{\Delta B}\right)^2}.$$

This lineshape occurs when the relaxation of the excitations of the examined spin ensemble to their original state can be described by an exponential decay. The probability for the spin still to be in the excited state after a time t passed would then be $p(t) = e^{-\frac{t}{\tau}}$ with a relaxation time τ. This relaxation time can be related to an uncertainty in energy

by the Heisenberg uncertainty principle [81]. The real value of the corresponding Fourier transform is:

$$\begin{aligned} A(\omega) &= \Re\left(\int_0^\infty e^{-\frac{t}{\tau}} e^{-i\omega t}\mathrm{d}t\right) \\ &= \frac{\tau}{1+\omega^2\tau^2}. \end{aligned} \tag{2.4}$$

Taking $\omega = \omega_0 - g\mu_B B$, setting $\Delta B = \frac{1}{g\mu_B \tau}$ and normalizing Eq. 2.4, we have:

$$\begin{aligned} A(B) &= A_0 \frac{1}{\pi\Delta B} \frac{1}{1+\left(\frac{B-\frac{\omega_0}{g\mu_B}}{\Delta B}\right)^2} \\ &= A_0 \frac{1}{\pi\Delta B} \frac{1}{1+\left(\frac{B-B_0}{\Delta B}\right)^2}. \end{aligned} \tag{2.5}$$

This corresponds to the microwave absorption of the spin ensemble in a magnetic field B for an incident microwave of energy $\nu_0 = \frac{\omega_0}{2\pi}$ which is given by the imaginary part χ'' of the susceptibility $\chi = \chi' + i\chi''$. The real part χ' is related to the so called dispersion part D of the ESR signal:

$$D(B) = D_0 \frac{1}{\pi\Delta B} \frac{B - B_0}{1+\left(\frac{B-B_0}{\Delta B}\right)^2}. \tag{2.6}$$

This part is irrelevant in setups that lock the frequency of the ESR source to the current eigenfrequency of the resonator by automatic frequency control (AFC) as this procedure suppresses any occurrence of $D(B)$. In experiments without a resonator, however, AFC is not possible and the obtained signal will be a mixture of $A(B)$ and $D(B)$ with a mixing angle ϕ:

$$P(B) = A(B)\cos\phi + D(B)\sin\phi, \tag{2.7}$$

which can lead to strong deviations from the pure Lorentzian lineshape. Especially in the case of an MVNA setup (see below), the recorded real and imaginary parts of the downconverted high-frequency ESR signal both contain a mixture of A and D. This makes correct identification of the individual resonance lines difficult, but it increases the sensitivity on the resonance field as the signals of both channels are simultaneously fitted to Eq. 2.7 with a common ϕ. In most cases, this mixing angle ϕ remains constant for an individual field sweep.

To increase the sensitivity of the X-band ESR experiments, the external field B is modulated with a small additional a.c.-component $B_{\mathrm{mod}}\cos(2\pi\nu_{mod}t)$ with an amplitude on the order of mT. Based on this modulation frequency ν_{mod} of typically several kHz,

the detected signal is then lock-in amplified as $I(B)$. Assuming that $\Delta B >> B_{\mathrm{mod}}$, the result will be the exact derivative of the sample absorption

$$I(B) = -2\frac{I_0}{\pi \Delta B^3}\frac{B - B_0}{\left(1 + \left(\frac{B-B_0}{\Delta B}\right)^2\right)^2}.$$

The amplitude I_0 of the underlying normalized Lorentzian line shape can then be directly compared to the susceptibility χ of the sample.

2.3.1 X-band ESR

The ESR experiments using a microwave frequency of $\nu = 9.56\,\mathrm{GHz}$ were performed using a commercial *Bruker EMX* spectrometer at the Institut für Werkstoffforschung (IFW, Dresden) with a rectangular resonator (*Bruker* 4104OR-C/0801 [82]). The temperature in the Helium gas-flow cryostat was controlled using an *Oxford Instruments* ITC503 temperature controller to stabilize sample temperatures between 4 K and 300 K with a temperature stability of about 0.05 K.

2.3.2 High-frequency ESR in quasistatic magnetic fields

The High-frequency ESR experiments in non-pulsed magnetic fields were performed at the Institut für Werkstoffforschung (IFW, Dresden). The employed *Oxford Instruments* cryostat allows magnetic fields up to 16 T with sample temperatures between 2 K and 300 K. This temperature range can be extended downwards to 0.3 K using an optional *Oxford Instruments* HelioxTL ^{3}He insert. The used microwave radiation was produced using either a Millimeterwave Vector Network Analzyer (MVNA, built by *AB millimetre*) or a Backward Wave Oscillator (BWO) as a source to achieve microwave frequencies between 83 GHz and 965 GHz.

The MVNA is based on mixing the ESR signal coming back from the sample with a reference signal of similar frequency. Analyzing this mixed signal, one can obtain information on both the total absorption and the dispersion (phase shift) of the microwave due to the sample.

The MVNA setup (depicted in Fig. 2.7) works as follows: an ESR signal of frequency f_1 is generated by the source 1 (based on the Gunn effect [84]). The frequency of the emitted radiation is then multiplied to Nf_1 using a harmonic generator HG (a Schottky-diode) before it is transmitted to the sample through waveguides with an inner diameter that is much larger than the microwave wave length (quasi-optical transmission). The microwave interacts with the sample and is reflected after experiencing a damping through

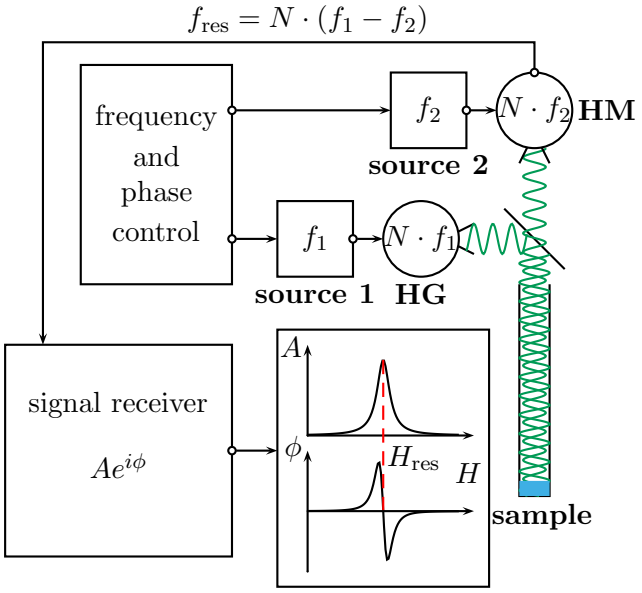

Abbildung 2.7: Operation principle of the Millimeter Vector Network Analyzer ESR setup (see text for explanations, adopted from Ref. [83]).

absorption, a phase shift ϕ and a rotation of the polarization. The part of the reflected signal with a polarization orthogonal to the original signal is then transmitted to a harmonic mixer HM (another Schottky diode), where it is mixed with another microwave of frequency Nf_2 (upconverted from source 2). This mixing is essentially a multiplication of the two signals:

$$A\cos(Nf_1 + \phi)\cos(Nf_2) = \frac{A}{2}\left\{\cos(N(f_1 + f_2) + \phi) + \cos(N(f_1 - f_2) + \phi)\right\}.$$

Using a low-pass filter, the high frequency contribution can be removed so that a signal with a frequency in the kHz-range can be processed using a corresponding lock-in amplifier. This signal contains information about both the amplitude A and the phase ϕ (absorption and dispersion, see above) of the ESR absorption, which can be analyzed simultaneously. As no cavity is used, the amplitude of the ESR signal is not given by the susceptibility of the spin system, contrary to the X-band case. The advantage of this setup is the ability to change the frequency in a quasi continuous manner in a broad range from 50 GHz to over 400 GHz, combined with a high frequency stability. More details on the operation principle and the capabilities of this setup can be found in Ref. [85].

The BWO is a different type of ESR source, providing radiation with frequencies up to 1.4 THz. It is based on the fact that accelerated charges emit electromagnetic radiation. Electrons moving in the vicinity of a magnet with a periodic structure will then emit radiation with a frequency both given by the speed of the electron and the periodicity of the structure. Inside a BWO element, electrons are emitted from a heated cathode and accelerated by a voltage on the order 1 kV. Thus, the frequency of the emitted radiation for a given BWO element can be controlled by changing the applied acceleration voltage

of the electrons. While the BWO is a standard ESR source for frequencies above 1 THz, the frequency stability and noise level is not as good as in the case of other ESR sources.

3 Experiments on $Ba_{3-x}Sr_xCr_2O_8$

The triplon BEC candidates $Ba_3Cr_2O_8$ [36] and $Sr_3Cr_2O_8$[37] have been proposed as prototype materials for the construction of a Josephson device of magnetic insulators [68]. The two materials have been studied extensively, both experimentally [36, 37, 86] and theoretically [87, 88, 89]. Admittedly, the BEC-region in the H-T-diagram of these two materials are well separated (see Fig. 3.2). As both materials constituting the Josephson junction need to be in the BEC state, a direct construction of a device of the two materials is therefore not possible. It is possible, however, to prepare members of the solid solution $Ba_{3-x}Sr_xCr_2O_8$. A change of the Sr content x changes the critical field $H_c(T)$, thereby shifting the BEC-region, as shown in this chapter.

3.1 General properties of $Ba_3Cr_2O_8$ and $Sr_3Cr_2O_8$

The compounds $Ba_3Cr_2O_8$ and $Sr_3Cr_2O_8$ have been known for several decades[90, 91]. Using X-ray diffraction techniques and analyzing the magnetic properties down to 90 K, it has been determined quite early that the chromium ions are in the unusual oxidation state Cr^{5+}[91]. Later, the crystal structure was determined by means of single crystal diffraction [92, 93]. At room temperature, both compounds exhibit a similar crystal structure, described by the space group $R\bar{3}m$ (see Fig. 3.1).

The Ba-/Sr- ions are stacked in groups of three along the c-axis at two different sites A_1 and A_2 with a multiplicity of 1 and 2, respectively. Between the Ba/Sr-ions, the Cr ions are located in pairs of two, each coordinated by an oxygen tetrahedron. Due to the tetrahedral coordination, the Cr ions are of valence 5+ with a total electron spin of $\frac{1}{2}$. These spin-$\frac{1}{2}$ ions are interacting due to super-super-exchange through the oxygen orbitals. As the different possible relative spin configurations lead to different exchange energies, one can think of the super-super-exchange as an effective intradimer coupling constant J_0. As J_0 is antiferromagnetic, the pairs of Cr^{5+} ions can be described in terms of dimers with a singlet ground state that is separated from the triplet states by an energy $\Delta E = J_0$.

Through the (weaker) exchange paths to other neighboring Cr^{5+} ions, the dimers form a three dimensional network, allowing a hopping of triplet excitations from one dimer

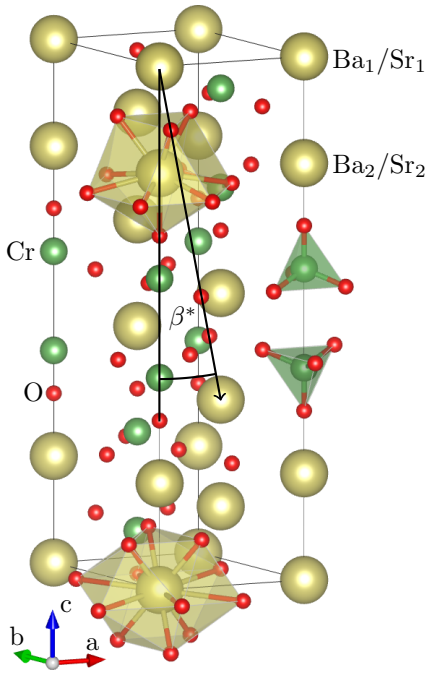

Abbildung 3.1: Crystal structure of $Ba_{3-x}Sr_xCr_2O_8$ at room temperature. The Cr tetrahedron is shown in dimer configuration on the right, the Ba_1/Sr_1-dodecatope is shown on the bottom and the Ba/Sr_2-decatope is shown on the top of the drawing. The angle $\beta^* = \beta - 90°$ is marked to show how the monoclinic angle β was calculated for Fig. 3.29. The picture has been partly created using the program *VESTA*.

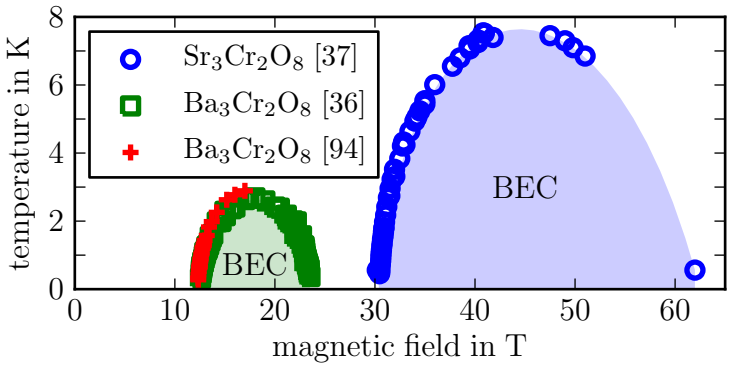

Abbildung 3.2: Sketch of the reported triplon BEC-phases of $Ba_3Cr_2O_8$ and $Sr_3Cr_2O_8$. Data points taken from Refs. [36, 37, 94]

to another. These interdimer coupling constants J_i lead to the formation of a three dimensional band structure that can be probed, i.e. with inelastic neutron scattering experiments. Using this technique, both the intradimer and the interdimer interactions have been estimated for the two compounds [86, 95]. In these experiments, it has been established that up to forth order nearest neighbor interactions have to be taken into account for an accurate description of the triplon dispersion (see Fig. 3.5). In the *Random Phase Approximation*, the model used to analyze these experiments, the triplon dispersion $\hbar\omega\left(\vec{K}\right)$ can be approximated as[96]

$$\hbar\omega\left(\vec{K}\right) = \sqrt{J_0^2 + J_0\gamma\left(\vec{K}\right)}, \tag{3.1}$$

$$\text{with } \gamma\left(\vec{K}\right) = \sum_i J\left(\vec{R}_i\right) e^{-i\vec{K}\vec{R}_i}, \tag{3.2}$$

where $\vec{R}_i$ is the spatial distance to the considered neighbor i, γ is the Fourier series of the magnetic interactions and $\vec{K} = h_{\mathrm{R}\bar{3}\mathrm{m}}\vec{b}_1 + k_{\mathrm{R}\bar{3}\mathrm{m}}\vec{b}_2 + l_{\mathrm{R}\bar{3}\mathrm{m}}\vec{b}_3$ is the scattering vector in terms of the space group R$\bar{3}$m. The Jahn-Teller transition occurring in the two materials (see section 3.7) lowers the the crystal symmetry so that the three directions are not equivalent any more. This leads to the introduction of a unique interaction with each of the three nearest neighbors instead of just one interaction parameter for all three. Marking these interactions as J_i', J_i'', J_i''', the Fourier sum $\gamma\left(\vec{K}\right)$for the two materials up to forth-nearest neighbor interaction can be given explicitly as

$$\begin{aligned}
\gamma\left(\vec{K}\right) = {} & 2J_1' \cos\left\{\frac{2}{3}\pi\left(2h_{\mathrm{R}\bar{3}\mathrm{m}} + k_{\mathrm{R}\bar{3}\mathrm{m}} + l_{\mathrm{R}\bar{3}\mathrm{m}}\right)\right\} \\
& + 2J_1'' \cos\left\{\frac{2}{3}\pi\left(-h_{\mathrm{R}\bar{3}\mathrm{m}} + k_{\mathrm{R}\bar{3}\mathrm{m}} + l_{\mathrm{R}\bar{3}\mathrm{m}}\right)\right\} \\
& + 2J_1''' \cos\left\{\frac{2}{3}\pi\left(-h_{\mathrm{R}\bar{3}\mathrm{m}} - 2k_{\mathrm{R}\bar{3}\mathrm{m}} + l_{\mathrm{R}\bar{3}\mathrm{m}}\right)\right\} \\
& + 2\left(J_2' - J_3'\right)\cos\left\{2\pi h_{\mathrm{R}\bar{3}\mathrm{m}}\right\} \\
& + 2\left(J_2'' - J_3''\right)\cos\left\{2\pi k_{\mathrm{R}\bar{3}\mathrm{m}}\right\} \\
& + 2\left(J_2''' - J_3'''\right)\cos\left\{2\pi\left(h_{\mathrm{R}\bar{3}\mathrm{m}} + k_{\mathrm{R}\bar{3}\mathrm{m}}\right)\right\} \\
& + 2J_4' \cos\left\{\frac{2}{3}\pi\left(2h_{\mathrm{R}\bar{3}\mathrm{m}} + 4k_{\mathrm{R}\bar{3}\mathrm{m}} + l_{\mathrm{R}\bar{3}\mathrm{m}}\right)\right\} \\
& + 2J_4'' \cos\left\{\frac{2}{3}\pi\left(2h_{\mathrm{R}\bar{3}\mathrm{m}} - 2k_{\mathrm{R}\bar{3}\mathrm{m}} + l_{\mathrm{R}\bar{3}\mathrm{m}}\right)\right\} \\
& + 2J_4''' \cos\left\{\frac{2}{3}\pi\left(-4h_{\mathrm{R}\bar{3}\mathrm{m}} - 2k_{\mathrm{R}\bar{3}\mathrm{m}} + l_{\mathrm{R}\bar{3}\mathrm{m}}\right)\right\}.
\end{aligned} \tag{3.3}$$

Tabelle 3.1: Reported interaction constants in $Ba_3Cr_2O_8$ and $Sr_3Cr_2O_8$.

	$Ba_3Cr_2O_8$[95]	$Sr_3Cr_2O_8$[86]
J_0	2.38(1) meV	5.551(9) meV
J_1'	0.08(2) meV	−0.04(1) meV
J_1''	−0.15(2) meV	0.24(1) meV
J_1'''	0.10(1) meV	0.25(1) meV
$J_2' - J_3'$	0.10(1) meV	0.75(9) meV
$J_2'' - J_3''$	0.07(2) meV	−0.543(9) meV
$J_2''' - J_3'''$	−0.52(2) meV	−0.120(9) meV
J_4'	0.04(2) meV	0.10(2) meV
J_4''	0.10(2) meV	−0.05(1) meV
J_4'''	0.09(2) meV	0.04(1) meV

The threefold rotational symmetry at the positions of the dimers found at room temperature leads to a spontaneous separation of the crystal into domains with three different orientations at the transition temperature [86], each equally contributing to the total neutron scattering amplitude. Therefore, all three domains will be probed at the same time and the obtained data will be a superpositions of the three triplon dispersion branches. The involved Fourier sums $\gamma\left(\vec{K}\right)$ can be generated through permutation of the interaction constants in Eq. 3.3 [86]:

$$\left\{J'_{1,2-3.4}, J''_{1,2-3.4}, J'''_{1,2-3.4}\right\} \rightarrow \left\{J''_{1,2-3.4}, J'''_{1,2-3.4}, J'_{1,2-3.4}\right\} \rightarrow \left\{J'''_{1,2-3.4}, J'_{1,2-3.4}, J''_{1,2-3.4}\right\}.$$

The bandwidth D, given by the difference of the highest and lowest possible triplon energy is therefore strongly influenced by changes in the interdimer interaction constants. Relating to Fig. 3.3, both J_0 and J_i are thus important for the critical field of the triplon-BEC. The reported interaction constants for the two materials are summarized in Tab. 3.1. While the interdimer interactions are comparable, the intradimer interaction in $Sr_3Cr_2O_8$ is much larger than in $Ba_3Cr_2O_8$, leading to a higher critical field (see Fig. 3.2).

Apart from neutron scattering experiments, an estimate for J_0 and the interdimer interactions can also be obtained by measuring the sample magnetization as a function of the temperature, $M(T)$[97, 98]. For a dimer system described by the Hamilton operator $\hat{H} = -J_0 \sum_i \hat{\vec{S}}_{i,1}\hat{\vec{S}}_{i,2}$, the magnetization M can be expressed as a function of the temperature T by

$$M(T) = \frac{n_d g^2 \mu_B B_{\text{ext}}}{k_B T\left(3 + e^{\frac{J_0}{k_B T}}\right)}, \tag{3.4}$$

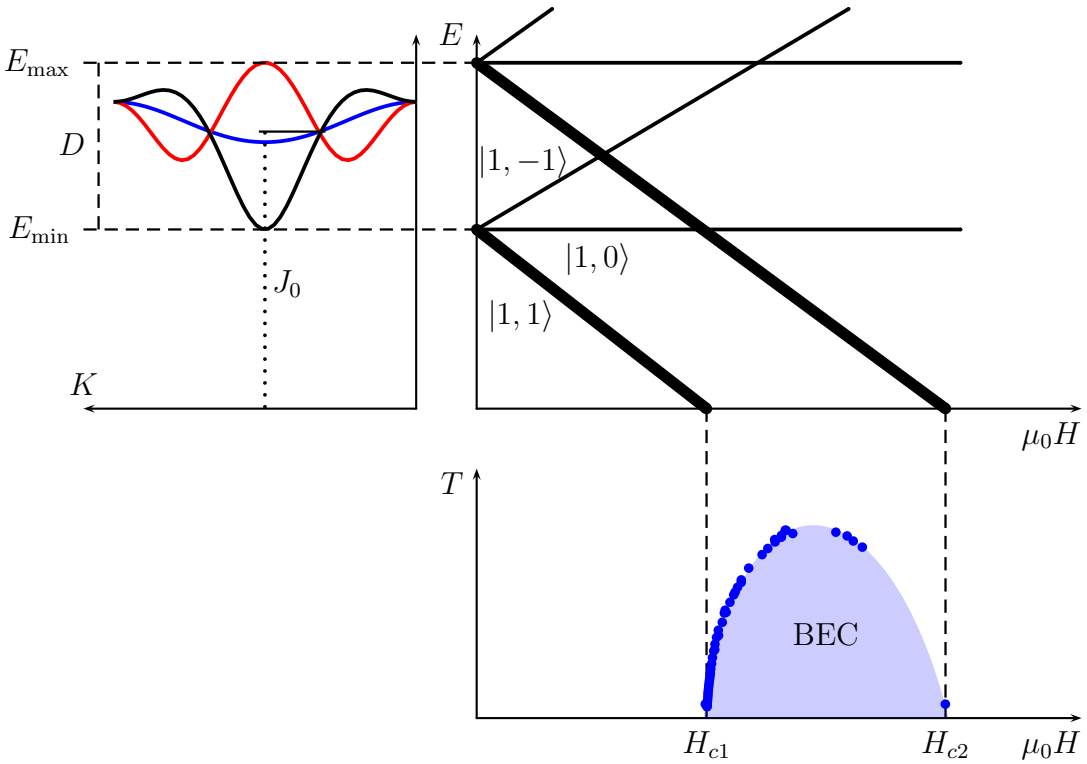

Abbildung 3.3: Relationship between the triplon dispersion $E\left(\vec{K}\right)$ and the critical fields H_{c1} and H_{c2} at zero temperature. Top left: triplon dispersion for $Sr_3Cr_2O_8$ from $\vec{K} = (-1,-1,0)$ to $\vec{K} = (0,0,0)$ with intradimer interaction constant J_0 and bandwidth D (calculated based on the reported interaction constants for $Sr_3Cr_2O_8$[86]). Top right: highest and lowest energy of the triplon bands as a function of the applied magnetic field $\mu_0 H$ due to Zeeman splitting (solid lines). The thick lines correspond to the lowest triplon branch that is relevant to the triplon BEC. Bottom right: BEC-dome for $Sr_3Cr_2O_8$ and critical fields corresponding to crossing of the singlet state with the bottom/top of the triplon bands (data points from Ref. [37]).

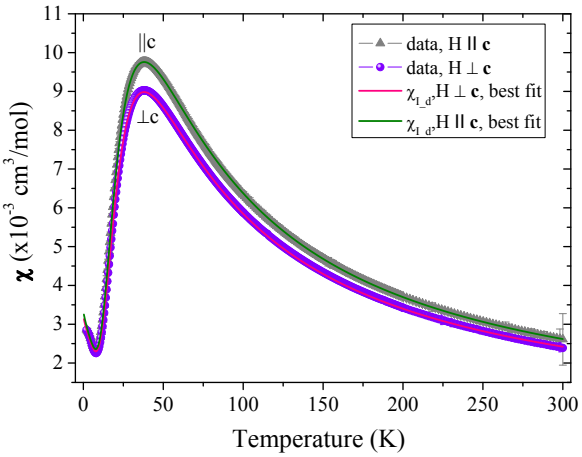

Abbildung 3.4: Magnetic susceptibility for a single crystal of $Sr_3Cr_2O_8$ as a function of the temperature (symbols) and corresponding fits using Eq. 3.5. Taken from [100]

derived by Bleaney and Bowers[99]. Here, g is the Landé factor, μ_B is the Bohr magneton, k_B is the Boltzmann constant and n_d is the dimer density. For systems of interacting dimers such as $Ba_3Cr_2O_8$ and $Sr_3Cr_2O_8$, the Hamilton operator includes additional interaction terms, $\hat{H} = -J_0 \sum_i \hat{\vec{S}}_{i,1}\hat{\vec{S}}_{i,2} + \sum_{i,j} J_{i,j}\hat{\vec{S}}_i\hat{\vec{S}}_j$. Therefore, the above formula has to be modified to take these interactions into account:

$$M(T) = \frac{n_d g^2 \mu_B B_{\text{ext}}}{J' + k_B T \left(3 + e^{\frac{J_0}{k_B T}}\right)}, \tag{3.5}$$

where J' is the effective interdimer interaction constant that incorporates all relevant $J_{i,j}$. For non-frustrated interactions, this effective interaction would be given by the modulus of the neighbor interactions, $J' = |J_1'| + |J_1''| + |J_1'''| + 2\left(|J_2'| + |J_2''| + |J_2'''|\right) + 2\left(|J_3'| + |J_3''| + |J_3'''|\right) + |J_4'| + |J_4''| + |J_4'''|$. Using Eq. 3.5, the interaction constants have been estimated to $J_0 = 2.328(2)\,\text{meV}$ and $J' = 0.52(2)\,\text{meV}$[36] for $Ba_3Cr_2O_8$ and $J_0 = 5.512(3)\,\text{meV}$ and $J' = 2.0(3)\,\text{meV}$[86] for $Sr_3Cr_2O_8$, in accordance with the reported values from inelastic neutron scattering experiments. However, the sensitivity of the fitting procedure on J' was found to be much weaker than the given uncertainty suggests [86].

As reliable experimental values for the interactions constants are known, several theoretical predictions of their strength have been reported, both quantitatively[87] and semiquantitatively[88, 101]. The latter work is based on calculations of the energy splittings $\Delta e_{\mu\mu}$ that occur to the μ-th orbital of a given CrO_4^{3-}-tetrahedron when interacting with the corresponding orbital of a neighboring CrO_4^{3-}-tetrahedron. The highest splitting occurs in the dimer configuration, but $\Delta e_{\mu\mu}$ is still sizable for the interaction between neighbors up to the forth order (see Fig. 3.5). The interaction constant for a given exchange path i can then be estimated as

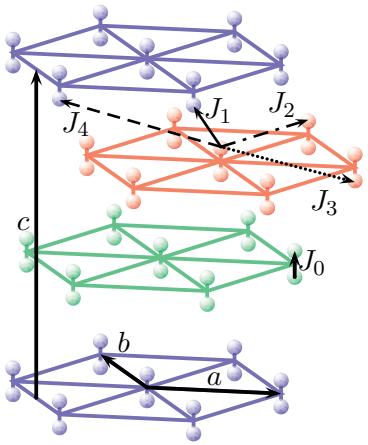

Abbildung 3.5: Spin interactions J_i found to be relevant in $Ba_3Cr_2O_8$ and $Sr_3Cr_2O_8$ according to [95, 86]. The spheres represent the Cr^{5+} ions that form the dimers, all other atoms are missing. The arrows marked as a, b and c give the lattice constants. The picture refers to the high temperature $R\bar{3}m$ phase.

$$J_i = 2K_{12} - \frac{\left\langle (\Delta e)^2 \right\rangle}{U_{\text{eff}}}, \tag{3.6}$$

where K_{12} is the ferromagnetic part of the interaction that can be neglected as it is dwarfed by the second, antiferromagnetic contribution[102]. The denominator U_{eff} is the effective on-site repulsion potential and should vary slowly as a function of distortion or substitution for closely related compounds [103]. The highest relevant Cr orbitals ($3z^2 - r^2$ and $x^2 - y^2$, see below) are only occupied by one electron in the room temperature structure of $Ba_3Cr_2O_8$ and $Sr_3Cr_2O_8$. Therefore, the splitting term is given by

$$\left\langle (\Delta e)^2 \right\rangle = \left(\frac{1}{2}\right)^2 \sum_{\mu=1}^{2} (\Delta e_{\mu\mu})^2 , \tag{3.7}$$

where the sum goes over the two equally occupied orbitals.

Using extended Hückel tight binding calculations, this energy difference and the resulting strength of J_i have been assessed in relation to similar compounds for $Ba_3Cr_2O_8$[88] or different structural configurations of $Sr_3Cr_2O_8$. In both cases, J_0 was to small in relation to similar compounds when the calculations were based on the room temperature structure while J' was found to be to large. Whangbo *et al.* therefore suggested an orbital ordering for $Ba_3Cr_2O_8$ that would leave only one orbital occupied [88]. This

should strengthen J_0 and decrease the value of J', in accordance with the comparison of experimental results for $Ba_3Mn_2O_8$ and $Ba_3Cr_2O_8$. Expanding this idea, Chapon *et al.* performed neutron powder diffraction experiments to probe the low temperature structure of $Sr_3Cr_2O_8$. Based on these experiments, they could verify the existence of a structural transition due to the Jahn-Teller active Cr^{5+} ions. This transition takes place at $T_{\mathrm{JT}} = 275\,\mathrm{K}$, strongly affects the lateral position of the apical oxygen in the CrO_4^{3-} tetrahedra (see Fig. 3.27) and thereby induces the expected orbital ordering. The threefold symmetry of the crystal system is broken and the space group $R\bar{3}m$ changes to $C_{2/c}$. In the room temperature structure, the Cr^{5+} ions are positioned in the middle of the oxygen tetrahedra with site symmetry 3m. The d-orbitals are grouped into the higher lying t state, given by the xy, xz and yz orbitals, and the lower lying e state, constituted by the $3z^2 - r^2$ and $x^2 - y^2$ orbitals. The remaining d-electron simultaneously occupies this twofold degenerate e state. Below the transition temperature T_{JT}, the apical oxygen gradually shifts perpendicular to the c-axis with decreasing temperature. This shift lifts the degeneracy of the e state, favoring a low lying, exclusively occupied $3z^2 - r^2$ orbital. The shift thereby enhances the splitting energy difference $(\Delta e_{11})^2$. In addition, the exclusive occupation reduces the splitting term to $\left\langle (\Delta e)^2 \right\rangle = \Delta e^2_{3z^2-r,3z^2-r}$, so that the total interaction constant for the exchange path i is given by

$$J_i = -\frac{\Delta e^2_{3z^2-r,3z^2-r}}{U_{\mathrm{eff}}}. \tag{3.8}$$

For $Sr_3Cr_2O_8$ the structural phase transition increases the total splitting term $\left\langle (\Delta e)^2 \right\rangle$ for the intradimer exchange path with $i = 0$ from $1010\,\mathrm{meV}^2$ at room temperature to $2390\,\mathrm{meV}^2$ at $T = 2\,\mathrm{K}$ (see Ch. 3.8). For $Ba_3Cr_2O_8$, the structural phase transition mentioned above for $Sr_3Cr_2O_8$ was found to take place as well, albeit with a much lower transition temperature of $J_{\mathrm{JT}} = 70\,\mathrm{K}$[95]. The splitting term for $i = 0$ increases from $740\,\mathrm{meV}^2$ at room temperature to $1450\,\mathrm{meV}^2$ at $T = 2\,\mathrm{K}$.

As mentioned above, ESR experiments are another valuable method to probe the excitations inside the dimer system. For a perfectly symmetric system, it is only possible to excite the $|1,-1\rangle \rightarrow |1,0\rangle$ and the $|1,0\rangle \rightarrow |1,1\rangle$ transition of the dimers using electromagnetic radiation. However, in real materials the Hamilton operator often contains terms that mix the wave functions of the singlet and triplet states like the Dzyaloshinskii-Moriya-interaction, leading to a non-zero probability of the $|0,0\rangle \rightarrow |1,-1\rangle$ and $|0,0\rangle \rightarrow |1,1\rangle$ transitions. Measurements of the frequency-field dependencies using frequencies of about 100 GHz to 1.5 THz have been performed by several groups for $Ba_3Cr_2O_8$[94, 104] and $Sr_3Cr_2O_8$[105] (see Fig. 3.7).

The observed modes E_1 and E_2 correspond to transitions in the center of the Brillouin zone (Γ-point) and at $\vec{K} = (0,0,1)$. Usually, only ESR excitations at the center of the Brillouin zone are possible, as $\Delta k = \frac{2\pi\nu}{c} \approx 0$ for a microwave frequency ν. However,

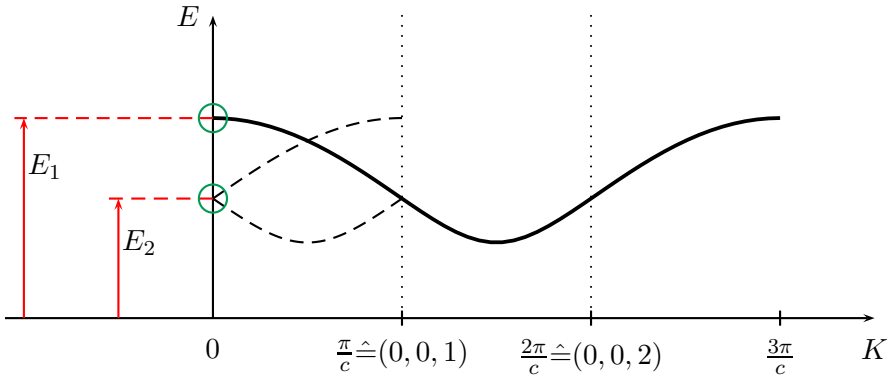

Abbildung 3.6: Sketch of the triplon dispersion along the $(0,0,1)$-direction for $Ba_3Cr_2O_8$ and $Sr_3Cr_2O_8$. ESR experiments can only access excitations with $\Delta k \approx 0$. However, the Dzyaloshinskii-Moria interaction that mixes singlet and triplet states, leads to an effective folding of the triplon dispersion into the first (reduced) Brillouin-zone. Therefore, not only states with $E = E_1$ can be excited, but also those with $E = E_2$ at the border of the Brillouin-zone (ESR-active states marked with green circles).

the three different bilayers lead to additional excitations at $\vec{k} = \vec{K}$, where $\vec{K}$ is the reciprocal vector corresponding to the connecting vector between equivalent bilayers in the crystal structure. For $Ba_3Cr_2O_8$ and $Sr_3Cr_2O_8$, $\vec{K} = (0,0,1)$ and $\vec{K} = (0,0,2)$. This is comparable to theoretical predictions for a spin dimer systems containing two different bilayers[106] and experimental results in TlCuCl3[107] and KCuCl3[108, 109]. It is a direct result of a staggered Dzyaloshinskii-Moriya interaction and can be understood in terms of the reduced Brillouin-zone (see Fig. 3.6). As the minimum and the maximum of the triplon dispersion are neither located at the Γ-point nor at the border of the Brillouin zone, they cannot be probed with ESR techniques(see Figs. 3.7). It is therefore not surprising that the critical fields for $Ba_3Cr_2O_8$ and $Sr_3Cr_2O_8$ do not coincide with the fields where the ESR gaps Δ_1 and Δ_2 are closed for the lowest triplon branch (see Fig. 3.7). Nevertheless, the smaller spin gap $\Delta_{Ba_3Cr_2O_8}$ in comparison to $\Delta_{Sr_3Cr_2O_8}$ is reflected in the lower lying ESR resonance modes for the singlet-triplet transition.

Several other techniques such as torque-magnetometry, measurements of the magneto-caloric effect, magnetic force experiments and elastic neutron scattering experiments have also been reported to probe the triplon-BEC region for $Ba_3Cr_2O_8$ and $Sr_3Cr_2O_8$[36, 37, 86, 94]. As we have not performed similar experiments on $Ba_{3-x}Sr_xCr_2O_8$, we will give no further details on these techniques.

In order to use $Ba_3Cr_2O_8$ and $Sr_3Cr_2O_8$ for the construction of a Josephson device (see chapter 1.3) it is necessary to change the critical fields, e.g. by doping. Our corresponding efforts are described in the following sections.

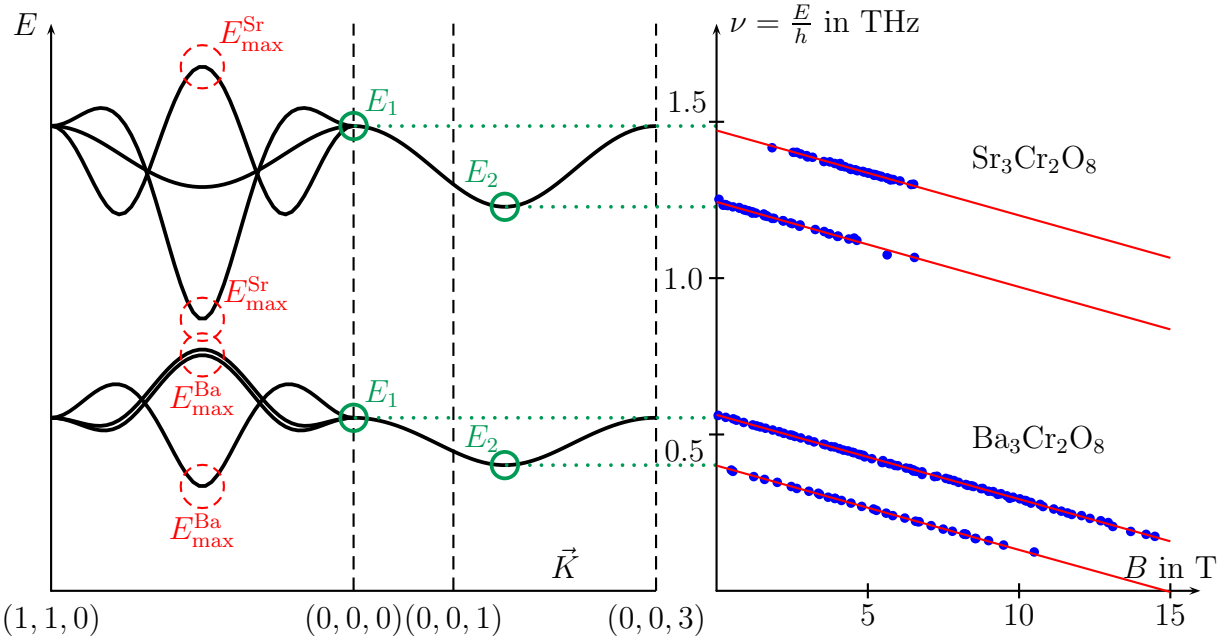

Abbildung 3.7: Left: Sketch of the calculated dispersion relation for $Ba_3Cr_2O_8$ and $Sr_3Cr_2O_8$, calculated based on the reported interaction constants [86, 95]. The red, dashed circles mark the extremal triplon energies at zero field, the green circles mark the possible ESR excitations. Right: Corresponding ESR-data taken from [110] and [104]. As the possible ESR excitations do not correspond to the extremal points of the triplon dispersion, no BEC is to be expected when the ESR gap closes.

3.2 Preparation of $Ba_{3-x}Sr_xCr_2O_8$

We prepared samples of $Ba_{3-x}Sr_xCr_2O_8$ based on two different reaction schemes. For the first method $Ba(NO_3)_2$, $Sr(NO_3)_2$ and $Cr(NO_3)_2 \cdot 9H_2O$ were used as reactants. The powders were mixed according to

$$(3-x)\mathrm{Ba(NO_3)_2} + x\mathrm{Sr(NO_3)_2} + \mathrm{Cr(NO_3)_2 \cdot 9H_2O} \rightarrow \mathrm{Ba_{3-x}Sr_xCr_2O_8} + \\ + 10\mathrm{NO_2} + \mathrm{O_2} + 9\mathrm{H_2O},$$

dissolved in water and heated afterwards while continuously stirred to keep the mixture homogeneous. After evaporating the water, the remaining powder was ground and heated under flowing Ar at 915 °C for 24 h to remove any excess water and NO_x. The resulting oxide powder was ground again, mechanically pressed into pellets and sintered at 1100 °C for 48 h under flowing Ar. For $x = 0.1$ and $x = 1.5$, rods were hydrostatically pressed and annealed under the same conditions. The obtained polycrystalline material was black, although regrinding (after the final annealing) in air or dry He-atmosphere lead to a slightly green hue that seemed more pronounced for intermediate x.

An optical floating zone method was used to grow crystals from those rods [111]. In this method, the light of four high power halogen lamps is focused onto a small volume by spherical mirrors. The polycrystalline rod is placed in that focus region. Depending on the chosen power of the lamps, the sample temperature can reach up to 1700 °C, thereby melting the material. By turning the rods it is ensured that the sample in the focus region is homogeneously illuminated. Slowly pulling the seed rod out of that region allows the liquid to cool slowly and recrystallize. The feed rod is gradually lowered with an appropriate speed to ensure a stable molten zone. One can thus think of the process as moving the molten zone along the feed rod. The molten and recrystallized material forms several grains which compete with each other until ideally only one remains at the end of the growth, analogous to furnace based molten zone methods like the Bridgman method.

Two of the obtained polycrystalline rods were mounted in a *Crystal Systems Inc.* image furnace using Pt wire, a short one (about 3 cm) as a seed rod, and a longer one (about 10 cm) as a feed rod. The crystal growth was performed in two stages, both in a high-purity environment of flowing Ar. The first stage was performed relatively fast (growth rates between 21 mm/h and 25 mm/h) to produce a premelted rod with a high density. For the second stage, the premelted rod was used as a feed rod with the remnants of the former feed rod as a seed. The growth rate was relatively low (between 2 mm/h and 5 mm/h), but was varied during the growth to maintain the zone stability. The resulting boule consisted of several, well oriented grains (see Fig. 3.8 for the X-ray Laue-diffractogram).

While we obtained crystalline samples for $x = 0.1$, attempts with $x = 1.5$ have not yet resulted in high quality crystalline material. For the neutron diffraction experiments

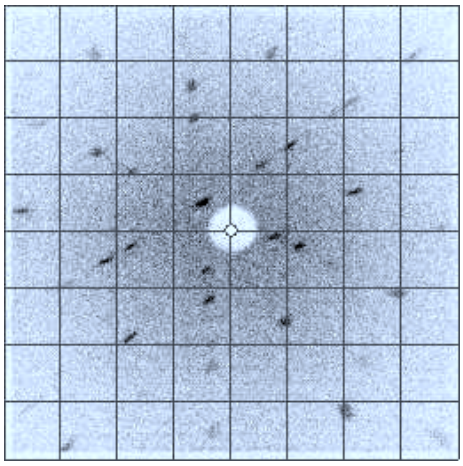

Abbildung 3.8: X-ray Laue diffractogram for the grown boule of $Ba_{2.9}Sr_{0.1}Cr_2O_8$. The beam direction was close to the c-axis. The hexagonal symmetry is clearly visible.

described below, a much greater total amount of each sample was needed. Therefore, we decided to explore different reaction schemes:

$$2(3\text{-x})BaCO_3 + 2xSrCO_3 + 4CrO_3 \rightarrow 2Ba_{3\text{-x}}Sr_xCr_2O_8 + 6CO_2 + O_2.$$

and

$$(3\text{-x})BaCO_3 + xSrCO_3 + Cr_2O_3 + O_2 \rightarrow Ba_{3\text{-x}}Sr_xCr_2O_8 + 3CO_2.$$

The latter has already been reported on for the mother compounds $Ba_3Cr_2O_8$ and $Sr_3Cr_2O_8$ [37, 94]. The respective carbonates and chromium oxides were mixed, ground and heated under flowing Ar at 1300 °C for 24 h. The resulting material was ground again and heated under flowing Ar at 1300 °C for 24 h. This last step was repeated several times.

The results from X-ray diffraction, static low field measurements of $M(T)$ and high field measurements of $M(H)$ were obtained from the samples prepared by the first method described above, and from single crystalline material (for $Ba_{2.9}Sr_{0.1}Cr_2O_8$). The neutron diffraction experiments were based on samples obtained with the third method described above.

3.3 Crystallographic structure at room temperature from X-ray diffraction

In order to perform structural analysis, parts of the obtained crystalline material as well as corresponding polycrystalline samples with $0 \leq x \leq 3$ were ground and examined using $Cu_{K\alpha}$ X-ray radiation. The used diffractometer was a *Stoe IPDS* in Debye-Scherrer diffraction geometry (see section 2.2.3). The powders were thinly distributed between two sheets of plastic tape to form an approximate plane and mounted on a circular holder so that the incoming X-ray beam was parallel to the ground and perpendicular to the sample plane. To average out any effects of an uneven distribution of the sample powders, the sample holder was spun around the beam axis. The beam was only collimated horizontally so that in the vertical direction, the total sample was illuminated. The resulting patterns were analyzed using the Rietveld method (*FullProf suite*). As expected, no difference was found between ground single crystals and polycrystalline material. All of the observed reflections of the mixed crystals are in good agreement with the space group $R\bar{3}m$ (see Fig. 3.9), which is the same as that of the mother compounds with $x = 0$ and $x = 3$. As scattering coefficients for Cr^{5+} were not available, the known corresponding parameters for Cr^{3+} were used.

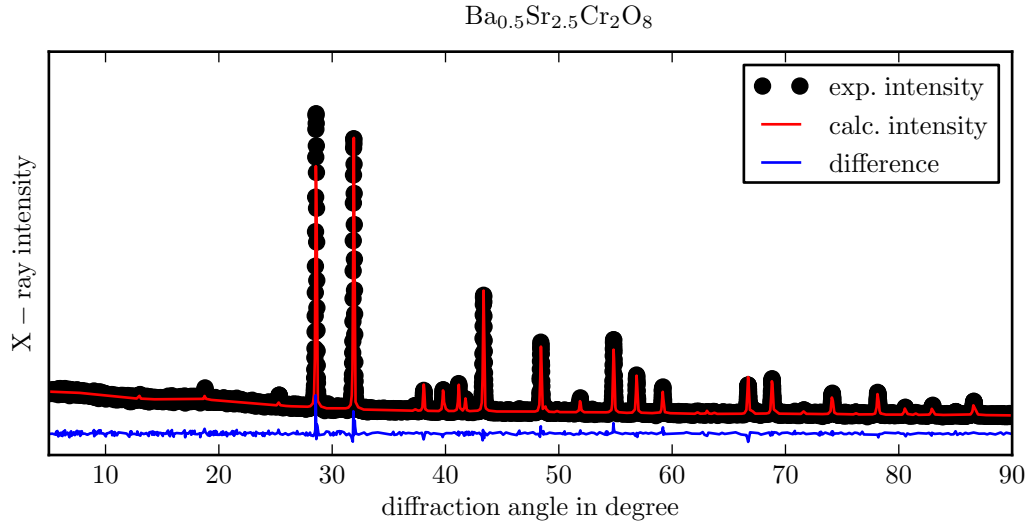

Abbildung 3.9: Experimental and calculated X-ray diffraction intensities for $Ba_{0.5}Sr_{2.5}Cr_2O_8$

The absolute values of the cell parameters depend linearly on the Sr content x, in agreement with Vegard's law (see Fig. 3.10). In Fig. 3.12, we have plotted the distance between two Cr ions forming a single dimer. As expected, this intradimer distance also decreases smoothly as a function of x. We did not find any relevant systematic change in the rela-

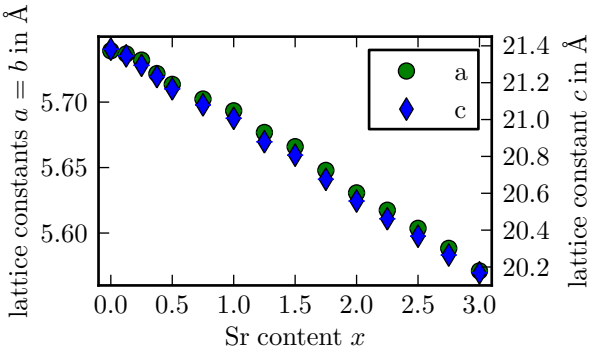

Abbildung 3.10: Lattice constants $a = b$ and c of $Ba_{3-x}Sr_xCr_2O_8$ as obtained from X-ray diffraction data, as functions of the Sr content x.

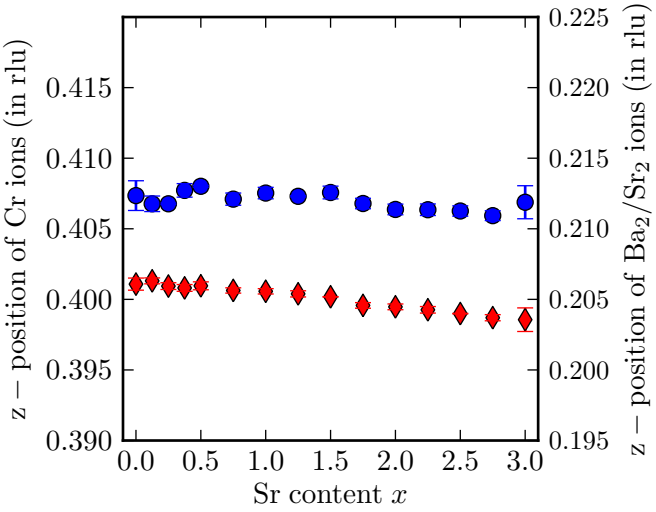

Abbildung 3.11: z-value of the atomic position for the Cr (circles) and Ba_2/Sr_2 ions(nomenclature according to [95]) (diamonds) as a function of the Sr content x. The x- and y-values were kept at zero.

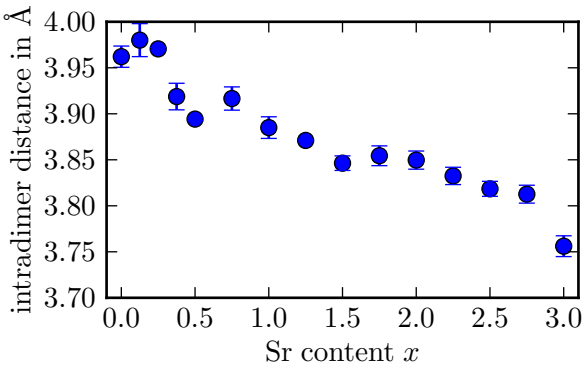

Abbildung 3.12: Distance between the Cr ions constituting one dimer as a function of the Sr content x.

tive atomic positions as a function of x, although it should be noted that the sensitivity of our X-ray experiments on the oxygen position is not high enough to exclude such a shift. In Fig. 3.11, we show the z-value of the atomic position for the Cr and Ba/Sr ions, while the respective x and y coordinates were assumed to be zero. All other atomic coordinates were kept zero for all x as well.

3.4 Obtaining J_0 from magnetization measurements

The magnetic properties of the polycrystalline samples were analyzed for temperatures between 2 K and 300 K and in magnetic fields of $\mu_0 H = 1\,\mathrm{T}$ and $\mu_0 H = 5\,\mathrm{T}$ (see section 2.1.1). For compositions with $x < 0.2$ and $x > 2.8$, the magnetization shows a pronounced maximum at low temperatures. The experimental data can be well described with the Bleaney-Bowers formula for interacting dimers,

$$M_d(T) = \frac{n_\mathrm{d} g^2 \mu_\mathrm{B} B_\mathrm{ext}}{J' + k_B T \left(3 + e^{\frac{J_0}{k_B T}}\right)}, \tag{3.9}$$

with $g = 1.94$, which is only slightly anisotropic in these systems[95, 86], n_d the density of the coupled ions. J' and J_0 are the inter- and intradimer coupling constants, respectively. For intermediate values of x around 1.5, a paramagnetic background becomes more and more relevant so that a Brillouin term had to be included,

$$M_p(T) = n_P g \mu_\mathrm{B} \frac{1}{2} \left(2 \coth\left(\frac{g\mu_\mathrm{B} B_\mathrm{ext}}{k_B T}\right) - \coth\left(\frac{g\mu_\mathrm{B} B_\mathrm{ext}}{2 k_B T}\right)\right), \tag{3.10}$$

where n_P denotes the density of the corresponding uncoupled ions. The experimental data are reasonably well described by the sum of the above terms (see Fig. 3.13). However, as the fit is not very sensitive to the interdimer interaction constant J' (especially in the presence of a strong paramagnetic background) we could not extract reliable values for it. It may be noted that the difference between values obtained by Eq. 3.10 and the usual approximation $M_p(T) = n_P g C \frac{B}{T}$ amounts to about 5 % for $\mu_0 H = 1\,\mathrm{T}$ at $T = 1.8\,\mathrm{K}$, the base temperature of the MPMS magnetometer.

The thus obtained intradimer interaction constant J_0 strongly depends on the stoichiometry, as shown in Fig. 3.14. Surprisingly, it first decreases with increasing Sr content up to $x \approx 1$, before increasing again up to the value for pure $Sr_3Cr_2O_8$. As the relative atomic positions do not change with x (see Fig. 3.11), we attribute the overall increase of the interaction constant to a decrease of the absolute intradimer distance of the Cr^{5+} ions from pure $Ba_3Cr_2O_8$ to pure $Sr_3Cr_2O_8$ (see Fig. 3.12).

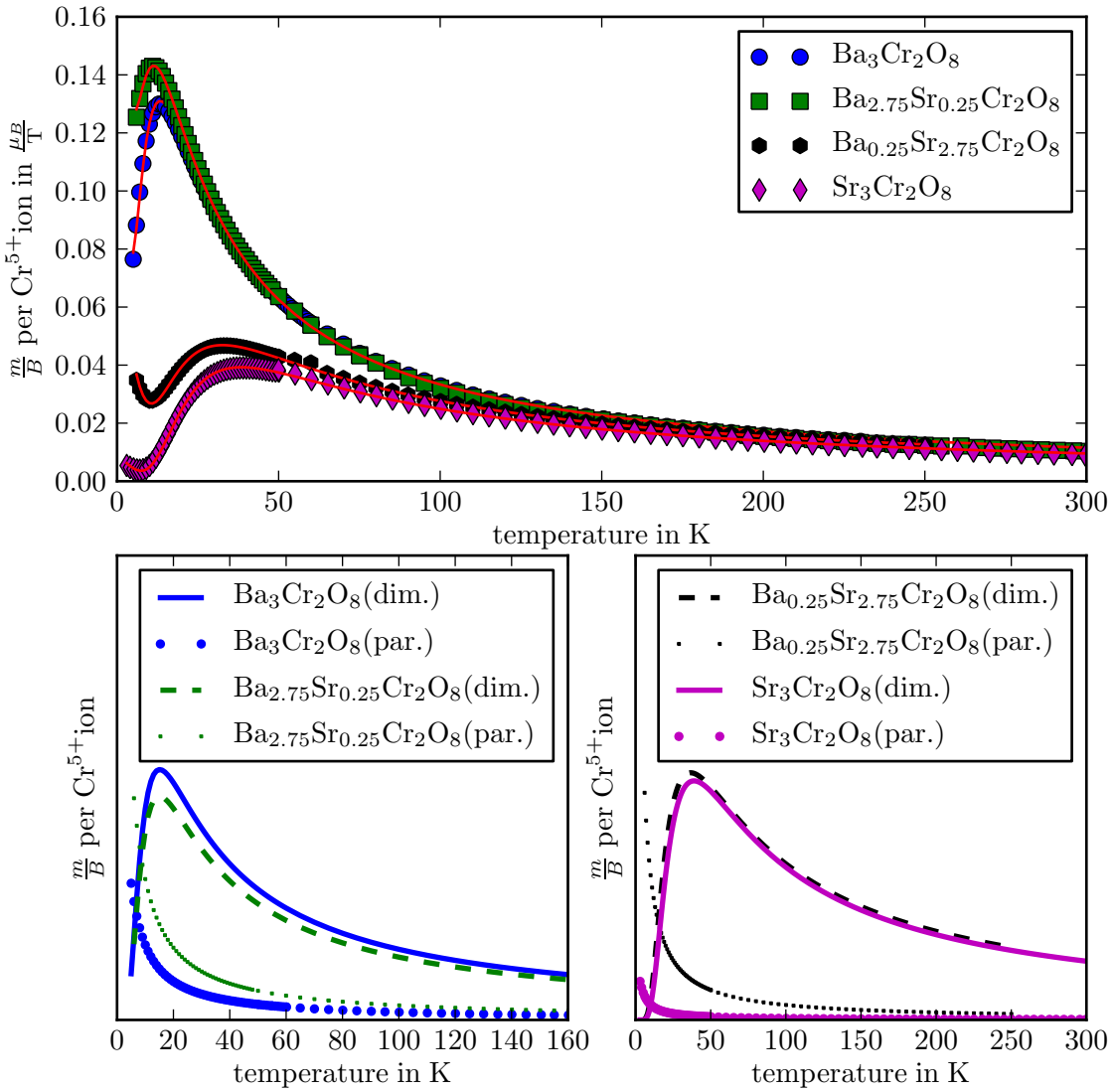

Abbildung 3.13: Upper panel: magnetization data $\frac{m}{B}(T)$ for four different stoichiometries of $Ba_{3-x}Sr_xCr_2O_8$ in $\mu_0 H = 1\,\mathrm{T}$. The solid lines correspond to fits according to a sum of Eqs. 3.9 and 3.10. The lower panels show the respective extracted paramagnetic (par.) and dimer (dim.) contributions to the total magnetization.

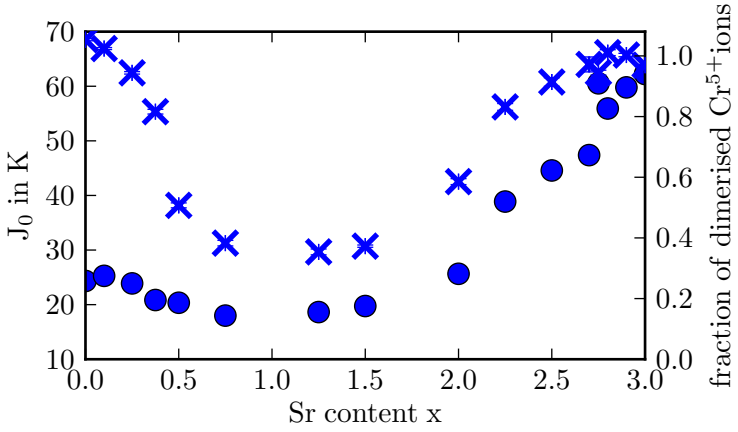

Abbildung 3.14: Estimated intradimer interaction constant J_0 in $Ba_{3-x}Sr_xCr_2O_8$ (filled circles) and the fraction of dimerized Cr^{5+}-ions (crosses, prefactor n_d from Eq. 3.9), as a function of the Sr content x.

3.5 Analyzing the magnetic background

In Fig. 3.14 we show the fraction n_d of dimerized Cr^{5+} ions and we compare it in Fig. 3.15 with the density n_p of uncoupled Cr^{5+} ions, both treated as independent fitting parameters. The paramagnetic background for intermediate x is substantial, but its microscopic origin is not clear up to now. The sum of the prefactors n_d and n_p is reasonably close to 1, which supports the validity of our fitting procedure. An increase of the preparation temperature to 1250 °C as well as repeated grinding and annealing of the polycrystalline samples did not reduce this background contribution substantially, but our corresponding X-ray diffraction data do, most interestingly, not suggest the appearance of possible impurity phases. In Fig. 3.16 we show the part of the total scattering intensity that is neither associated with the expected diffraction peaks of $Ba_{3-x}Sr_xCr_2O_8$ ($I_{calc.}$) nor with the diffuse background ($I_{diff.}$), normalized to the total integrated intensity without the diffuse background. Within the accuracy of this procedure, diffraction peaks stemming from unwanted impurity phases are virtually absent for all values of x. Furthermore, no systematic behavior similar to that of n_p can be found as a function of x. We therefore believe that this magnetic background is intrinsic to the polycrystalline system $Ba_{3-x}Sr_xCr_2O_8$. One possible reason is an increase of quasi-free spins due to broken (*dangling*) bonds, e.g. located at domain boundaries.

The background n_p as a function of x is shaped like an asymmetric dome with a maximum that is slightly shifted to lower values of x. This is strikingly similar to the atomic disorder in the system examined below (see section 3.9).

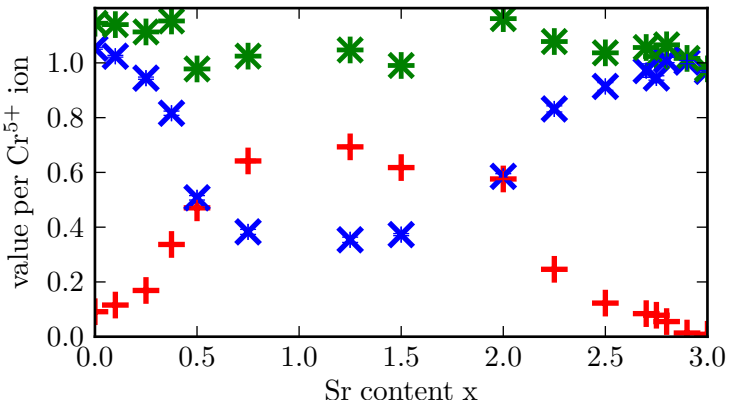

Abbildung 3.15: Estimated fraction n_d of dimerized (crosses) and free Cr^{5+} ions n_p (plus signs) from Eqs. 3.9 and 3.10 and the sum $n_d + n_p$ (stars), as functions of the Sr content x.

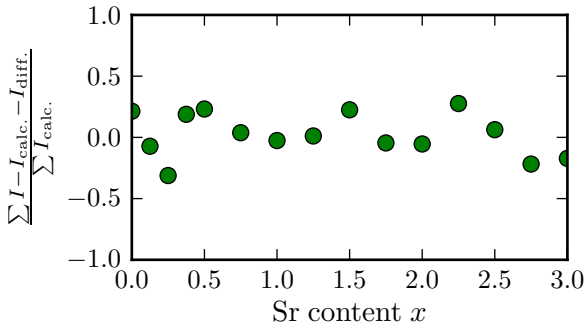

Abbildung 3.16: Integrated scattering intensity of potential impurities.

3.6 Estimating J_0 from high field ESR experiments

As shown in Fig. 3.3 and given by Eqs. 3.2 and 3.3, it is the interaction constant J_0 that is largely responsible for the energy difference between singlet state and the triplet band. In principle, it should therefore be possible to detect changes of J_0 using high frequency ESR techniques. Recent high-frequency ESR experiments on $Ba_3Cr_2O_8$ and $Sr_3Cr_2O_8$ have been performed on single crystals[95, 104, 105, 110]. However, single crystalline material of sufficient quality for ESR experiments was not available with $x \notin 0, 3$. We therefore decided to perform high frequency ESR experiments on a powder sample of $Ba_{0.33}Sr_{2.67}Cr_2O_8$ in order to probe possible changes in the magnetic excitation spectrum. Our magnetization measurements suggested a spin gap of more than 3 meV. Assuming a Landé factor of $g = 1.92$, an ESR excitations frequency of more than $\nu = 450$ GHz would be needed for even the lowest singlet-triplet excitation. Despite the frequency stability of the MVNA setup, we decided to probe the excitation spectrum of $Ba_{0.33}Sr_{2.67}Cr_2O_8$ using an BWO ESR source in conjunction with a GaAs diode based detector that was

cooled with liquid ^{4}He (see section 2.3.2). To ensure a high enough ESR transmission, we ground the sample and mixed it with an ESR silent, *Araldit* type epoxy in a mass ratio of about one to ten. The resulting sample was placed at the bottom of the waveguide, covering it completely.

Different BWOs were used to achieve excitation frequencies between 610 GHz and 970 GHz. Up to two clearly distinguishable resonance lines could be observed in the obtained ESR spectra (see Fig. 3.17) similar to the reported experiments on $Sr_3Cr_2O_8$[105]. These reso-

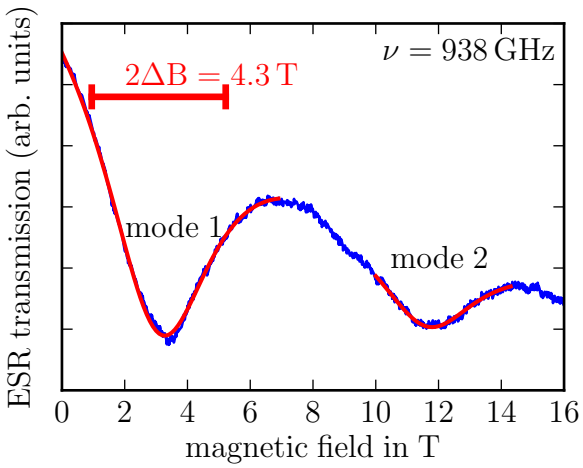

Abbildung 3.17: ESR spectrum of $Ba_{0.33}Sr_{2.67}Cr_2O_8$ for an excitation frequency of $\nu = 938\,\mathrm{GHz}$ taken at $T = 5\,\mathrm{K}$. The solid red lines are the corresponding fits (see text).

nance lines were fitted using a Lorentzian lineshape with a linear background (see Eq. 2.5) to determine the resonance field as a function of the frequency. The corresponding frequency-field diagram shows a linear decrease of the two observed modes as a function of the magnetic field. It is therefore reasonable to identify these modes with the reported *optical* and *acoustical* modes (called $1'$ and 1 in [95] and [105]). A linear fit of the two modes with a common slope gives zero-field excitation frequencies of $\nu_0' = 980(10)\,\mathrm{GHz}$ and $\nu_0 = 1190(20)\,\mathrm{GHz}$. These values are considerably lower than those reported for $Sr_3Cr_2O_8$, where $\nu_0' = 1240\,\mathrm{GHz}$ and $\nu_0 = 1470\,\mathrm{GHz}$. According to Eq. 3.2, this indicates a corresponding lowering of J_0. The difference $\Delta\nu_{x=2.67} = \nu_0 - \nu_0' = 220(30)\,\mathrm{GHz}$ is close to the corresponding value of $\Delta\nu_{x=3} = 230\,\mathrm{GHz}$ for pure $Sr_3Cr_2O_8$. Rewriting Eq. 3.2 as

$$h\nu = J_0\sqrt{1 + \frac{\gamma(h,k,l)}{J_0}},$$

and assuming that any changes in γ and J_0 are small compared to the absolute value of J_0, on can estimate the interaction constant from a change in the zero field ESR gap ν'

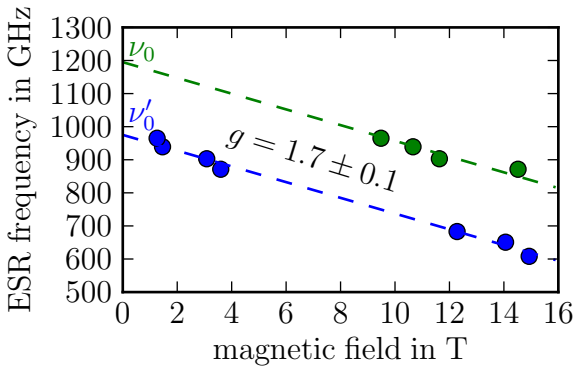

Abbildung 3.18: Experimental frequency-field diagram for $Ba_{0.33}Sr_{2.67}Cr_2O_8$. The dashed lines correspond to linear fits on the measured resonance lines. The thus obtained zero field ESR gaps are given as $\nu_0 = 980(10)\,\mathrm{GHz}$ and $\nu_1 = 1190(20)\,\mathrm{GHz}$ with a Landé factor of $g = 1.7(1)$.

by

$$J_0(x = 2.67) = J_0(x = 3)\frac{\nu_0'(x = 2.67)}{\nu_0'(x = 3)} = 4.50(8)\,\mathrm{meV}.$$

The thus estimated interaction constant matches the corresponding values from the magnetization measurements described above (see Fig. 3.19). It should be noted, however, that the measured ESR resonance lines were much broader than what has been reported for $Sr_3Cr_2O_8$ and $Ba_3Cr_2O_8$[105, 104]. As an anisotropy of the g-tensor could lead to a

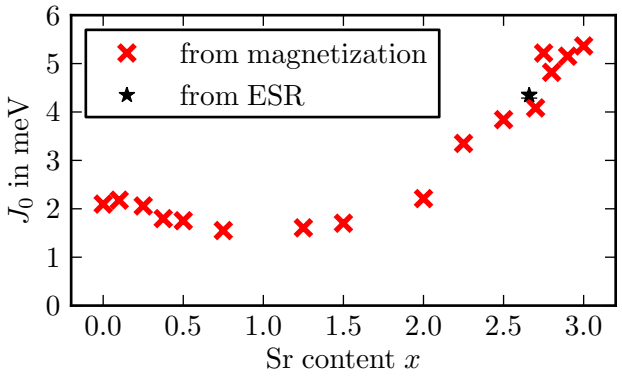

Abbildung 3.19: Estimated value of the intradimer interaction constant J_0 as a function of the Sr content x from magnetization measurements (see section 3.4) and high-frequency ESR experiments.

strong broadening of the ESR resonance lines, we additionally obtained high-frequency ESR spectra for a single crystal and for a powder sample of $Sr_3Cr_2O_8$ as a reference. The linewidth is similar in both cases (see Fig. 3.20) and almost an order of magnitude smaller than in the case of $Ba_{0.33}Sr_{2.67}Cr_2O_8$ so that an anisotropic g-tensor can be safely

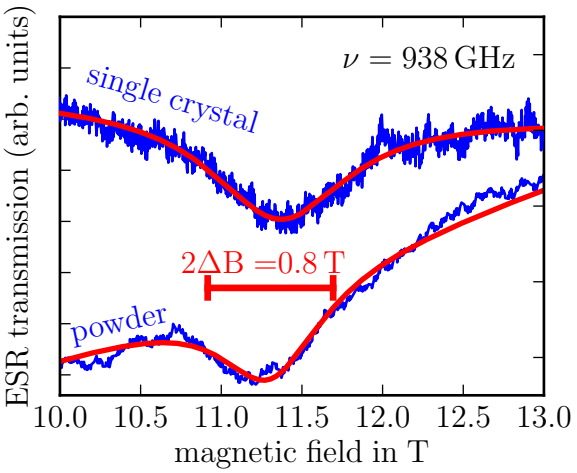

Abbildung 3.20: ESR resonance line of a single crystalline sample and a powder sample of $Sr_3Cr_2O_8$ for a excitation frequency of $\nu = 938\,\mathrm{GHz}$. The width of both lines is of similar size.

ruled out as a reason for the observed strong broadening. It is, however, possible that a distribution of different values of the interaction constant J_0 itself is present due to changes in the local environment from one Cr site to another. Such a distribution would imply that some dimers are stronger (or more weakly) coupled and therefore fulfill the resonance condition at higher (lower) fields, resulting in a broadening of the ESR line. We come back to that idea in section 3.9 and 3.10.

3.7 Crystallographic structure from neutron diffraction

As it is conceivable that the peculiar change of J_0 as a function of x can be explained based on changes in the crystal structure, we have performed high resolution neutron diffraction experiments at the HRPT at PSI. In the neutron powder diffraction patterns obtained at room temperature, the observed diffraction peaks could be indexed using the space group $R\bar{3}m$ for all x. From a Rietveld refinement of the diffraction data we obtained an almost linear behavior of the lattice constants a and c as a function of the Sr content, in accordance with the presented X-ray diffraction results (see Fig. 3.21).

Structural changes as a function of the Sr content x were also observed for the oxygen polyhedra surrounding the metal ions. The oxygen tetrahedron around the Cr ion is only slightly affected by varying the stoichiometry. Neither the tetrahedron height h_{th} nor the corresponding edge length M of the base triangle changes significantly as a function of x (see Fig. 3.22).

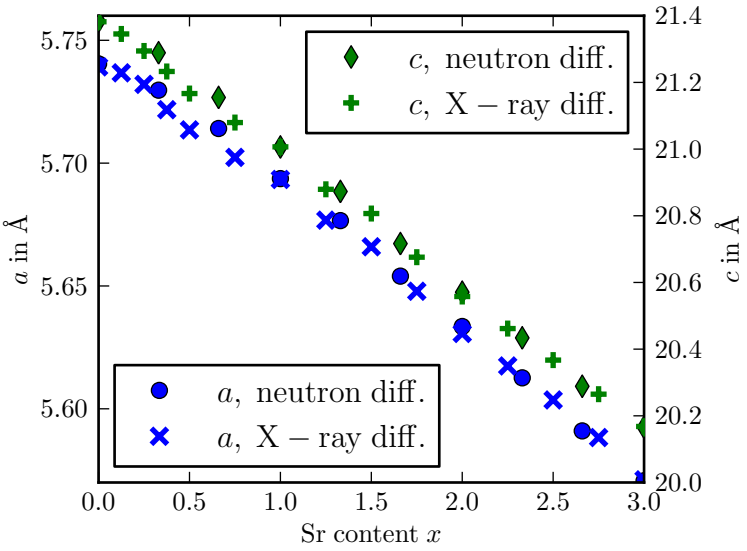

Abbildung 3.21: Lattice constants a and c of $Ba_{3-x}Sr_xCr_2O_8$ at room temperature (space group $R\bar{3}m$). The lattice constants are shown as a function of the Sr content x as obtained from X-ray and neutron powder diffraction experiments. The error bars for the values obtained from neutron diffraction are smaller than the size of the markers.

The Ba/Sr atoms are located at two different positions, site A_1 and A_2. The respective Wyckoff positions are $3a$ and $6c$ for $R\bar{3}m$ ($4e$ and $8f$ for $C_{2/c}$). The atoms located in the Ba_2-position with point site symmetry $3m$ are 10-fold coordinated. The height h_{dt} of the decatope changes linearly as a function of x (see Fig. 3.22). The almost planar oxygen hexagon surrounding the Ba_2 position is not evenly formed. Although the inner angle is always $\alpha = 120°$, the edge length M that is shared with the chromium tetrahedron is shorter than the edge length N that is shared only with the Ba_1 dodecatope. The value of N decreases with increasing x until M and N are equal for $x = 3$ (see Fig. 3.22).

The position Ba_1 is twelve-fold coordinated with site symmetry $\bar{3}m$ (see Fig. 3.22 a). As stated above, the edge length N is shared with the Ba_2-decatope. Both edge lengths N and O as well as the dodecatope height h_{ddt} decrease linearly as a function of x (see Fig. 3.22). Based on the bond lengths derived from the structural data, we have calculated the bond valence for Ba and Sr for both positions. These calculations were performed according to Refs. [112] and [113] and the results are plotted in Figs. 3.23 and 3.24. For both Ba/Sr-positions the average valence is almost equal to 2 for all x.

All oxygen polyhedra and corresponding ion valences therefore change strictly monotonously as a function of x. The site occupancies, on the other hand, are found to be non-monotonous (see Fig. 3.25). On the top of Fig. 3.25, the probability for a given Ba-ion to occupy either site A_1 or site A_2 as a function of the Sr content x is plotted. As site

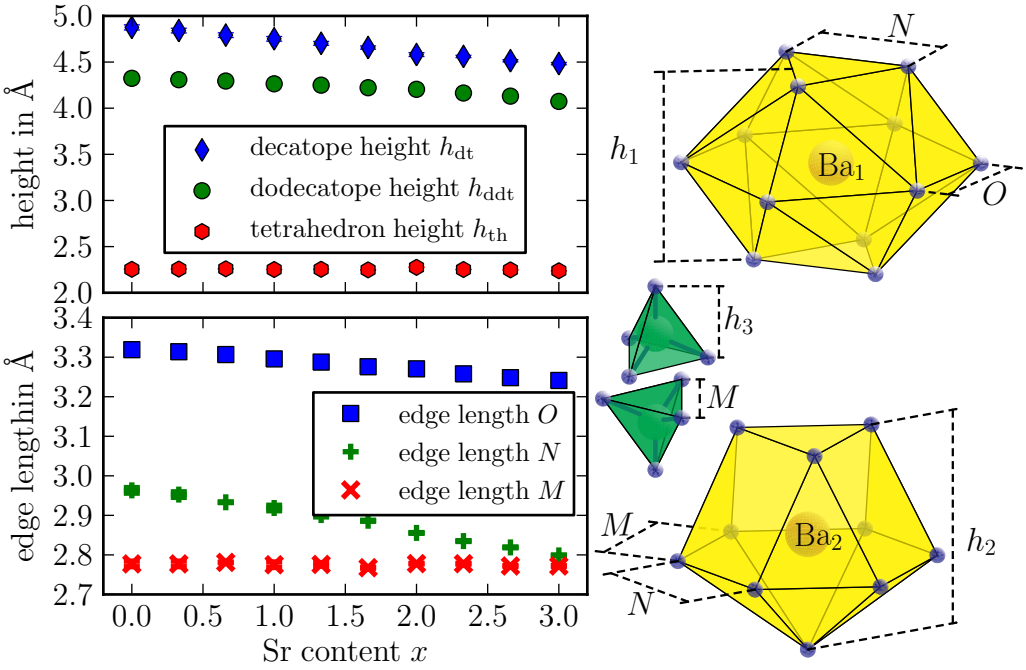

Abbildung 3.22: Height and edge length of the oxygen polyhedra in $Ba_{3-x}Sr_xCr_2O_8$ as functions of the Sr content x. The sketches on the right show the definitions of the plotted parameters.

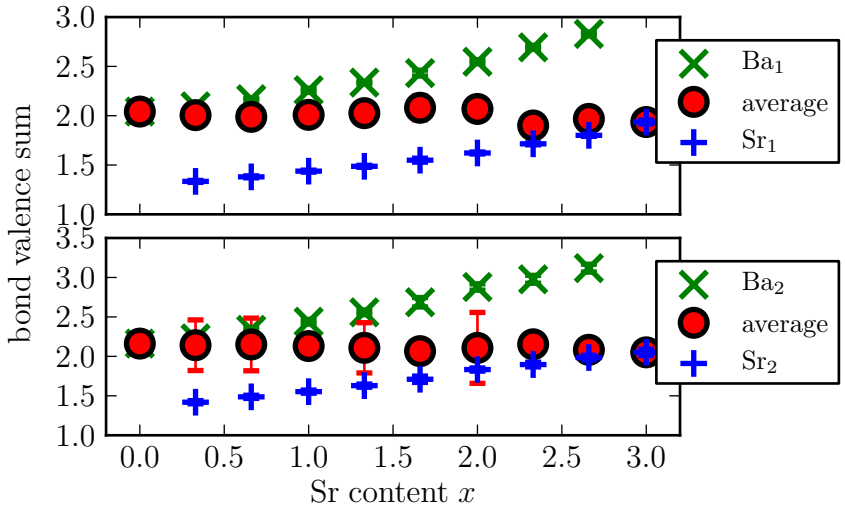

Abbildung 3.23: Calculated bond valence sums for the Ba/Sr-ions at sites A_1 (top) and A_2 (middle) in $Ba_{3-x}Sr_xCr_2O_8$ at room temperature. The average is the sum of the individual valence values weighted by the respective site occupancies.

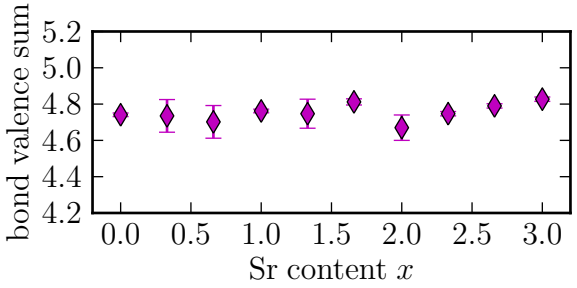

Abbildung 3.24: Calculated bond valence sums for the Cr ions in $Ba_{3-x}Sr_xCr_2O_8$ at room temperature.

A_1 has a multiplicity of 3 and site A_2 has a multiplicity of 6, the occupation probabilities should be $\frac{1}{3}$ and $\frac{2}{3}$, respectively. However, the probability for a Ba-ion to occupy site A_1 increases for increasing Sr content, while that of site A_2 decreases until both probabilities are $\approx \frac{1}{2}$. The corresponding probabilities for a given Sr-ion change accordingly. This preferred occupation can be understood by examining the calculated ion valence at site A_1 and site A_2. As the optimal valence for Ba and Sr would be 2, occupying a position where the valences deviate from this value should require additional energy. We can therefore associate an energy $E_i^{\mathrm{Ba,Sr}} \propto \left|\nu_i^{\mathrm{Ba,Sr}} - 2\right|$ with the valence values ν_i that differ from the optimal value at site i. The energy difference $\Delta E_{i\to j}^{\mathrm{Ba,Sr}} = E_i^{\mathrm{Ba,Sr}} - E_j^{\mathrm{Ba,Sr}}$ then represents the energy gain (loss) when bringing a certain ion from site i to site j. For a positive value of $\Delta E_{i\to j}^{\mathrm{Ba,Sr}}$, site j should be preferentially occupied. In the middle of Fig. 3.26, we have plotted $\Delta E_{2\to 1}^{\mathrm{Ba}}$ and $\Delta E_{1\to 2}^{\mathrm{Sr}}$ as functions of x. As both position changes are energetically favorable, site A_1 should be preferred by Ba-ions and site A_2 by Sr ions, exactly as our data indicate.

Our analysis of the diffraction patterns obtained at $T = 2\,\mathrm{K}$ shows that the lattice symmetry is lowered for some, but not all values of x upon cooling. For chemical compositions close to the parent compounds, i.e. for $x \in \{0, 0.33, 2.33, 3\}$, the lattice is better described using the space group $C_{2/c}$, that has been reported for $Ba_3Cr_2O_8$ and $Sr_3Cr_2O_8$ at low temperatures, with new diffraction peaks appearing (see Fig. 3.27). For the remaining samples, no superstructure peaks could be observed. The diffraction pattern at $T = 2\,\mathrm{K}$ could be equally well described by both space groups $R\bar{3}m$ and $C_{2/c}$, indicating a suppression of the structural phase transition.

Where detected, the symmetry breaking is due to a displacement of the apical oxygen of the tetrahedron surrounding the Cr^{5+} ions (O_1 in our notation, see Fig. 3.1 and Fig. 3.29). This oxygen shift is smaller for intermediate x (see Fig. 3.29) than for the parent compounds. By shifting O_1 along the O_2-O_3-edge, the site symmetry of the Cr ions ($3m$ at room temperature) is entirely lost. This oxygen shift affects the electronic orbitals of the Cr ions. In the case of a perfect tetrahedron, the d-orbitals are grouped into a lower lying, twofold degenerate e_g state and a higher lying, threefold degenerate t_g

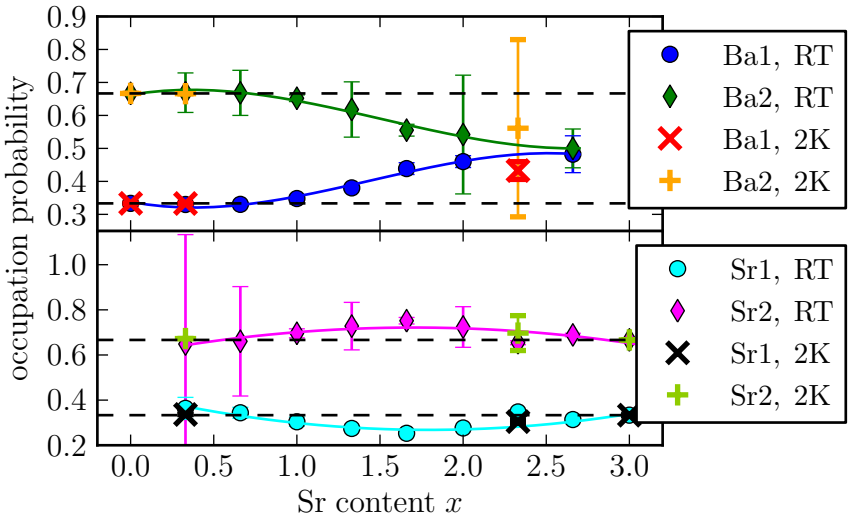

Abbildung 3.25: *Top*: Probability for a given Ba-ion to occupy one of the possible atomic positions. *Bottom*: Probability for a given Sr-ion to occupy one of the possible atomic positions. Dashed lines mark the probability that would be expected for completely random distributions and considering the respective position multiplicities. Solid lines are cubic fits to guide the eye.

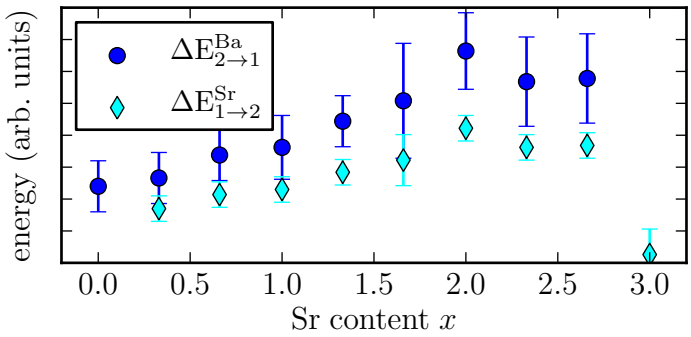

Abbildung 3.26: Energy difference $\Delta E^{Ba}_{2\bar{1}}$ when transferring a Ba-ion from position A_2 to position A_1 and the opposite for a Sr-ion.

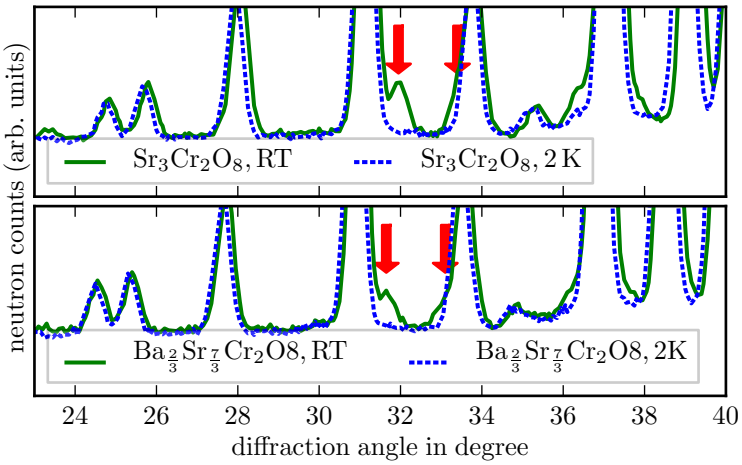

Abbildung 3.27: Additional peaks appearing in the low temperature neutron diffractograms for $Sr_3Cr_2O_8$ and $Ba_{\frac{2}{3}}Sr_{\frac{7}{3}}Cr_2O_8$, indicating the structural phase transition.

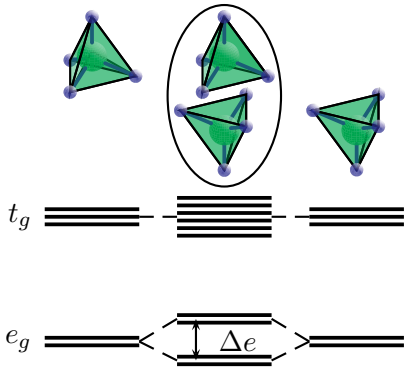

Abbildung 3.28: Sketch for the orbital splitting Δe that occurs when two CrO_4^{3-}-tetrahedra form a dimer. The sketch refers to the undistorted structure.

state. When the symmetry breaking occurs in $Ba_{3-x}Sr_xCr_2O_8$, the e_g state degeneracy is lifted, with a separation into a lower lying $3z^2 - r^2$ orbital and a higher lying $x^2 - y^2$ orbital. Therefore, both of the e_g-states have to be considered when calculating $\langle \Delta e \rangle$ in case of the space group $R\bar{3}m$, whereas only the $3z^2 - r^2$ orbital has to be taken into account for $C_{2/c}$.

Apart from a shift of the apical oxygen atom, the structural distortion also affects the monoclinic angle β. Where the distortion could be detected, β deviates slightly by $\Delta\beta$ from the value that is expected from a conversion between the rhombohedral and the monoclinic space group (see Fig. 3.1). The value of $\Delta\beta$ was found to depend on x (see Fig. 3.29) and vanishes for stoichiometries where the Jahn-Teller transition is suppressed. The obtained structural details are summarized in the appendix.

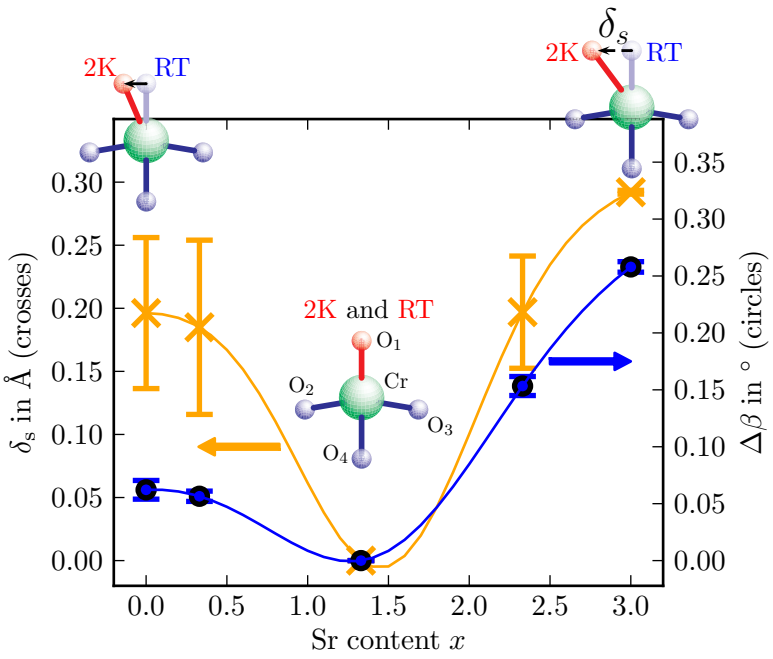

Abbildung 3.29: Distance δ_s of the apical oxygen atom from the dimer axis (crosses) and the angle distortion $\Delta\beta$ (circles) as a function of the Sr content x. The solid lines are guides to the eye. The distance in the corresponding sketches is exaggerated for visual clarity.

3.8 Calculating J_0 by taking the structural transition into account

To quantitatively examine the effect of the oxygen shift on the interaction constant J_0, we calculated the energy splitting $\langle \Delta e \rangle$ for the obtained crystal structures and estimated the repulsion potential U. The calculations are based on the EHTB technique to obtain the orbital energies. This technique is an extension of the Hückel method to non-π orbitals. It is based on treating the molecular orbitals as a linear combination of the atomic orbitals that belong to the respective atoms in the molecule. The method involves a relatively low computational effort compared to ab-initio techniques such as density functional theory, but requires precise structural information for a successful calculation of the orbital energies. This information was taken from our refinement of the neutron diffraction data. Our EHTB calculations have been fully performed using the well tested *SAMOA*-suite[1]. As this software is precompiled, we can give no details on the actual implementaion of the EHTB method. All parameters of the atomic orbitals used for the calculations where chosen according to Ref. [88].

Unfortunately, no experimental values for J_0 at room temperature have been reported.

[1] Available free of charge at http://www.primec.com/.

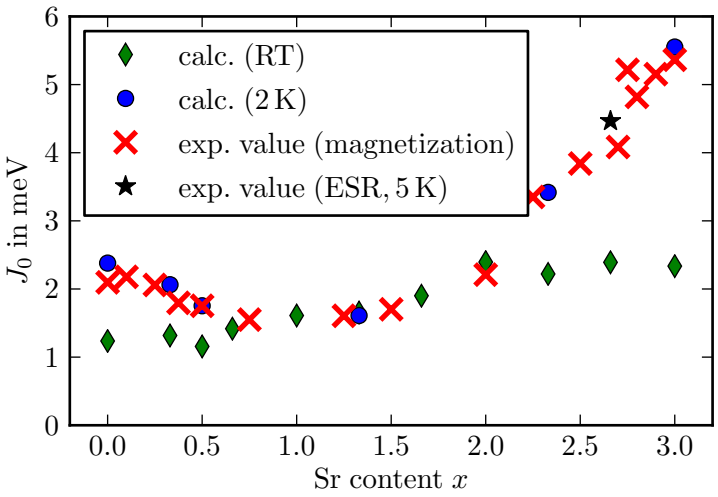

Abbildung 3.30: Intradimer interaction constant J_0 for $Ba_{3-x}Sr_xCr_2O_8$ as a function of the Sr content x. The shown data points are experimentally obtained from SQUID-measurements and high field ESR experiments (see section 3.4) as well as theoretically estimated based on EHTB-calculations for the crystal structure at room temperature and $T = 2\,\mathrm{K}$, respectively.

To obtain reasonable values for U, we therefore first carried out EHTB calculations based on the low temperature structures for $x = 0$ and $x = 3$. Our calculations yielded orbital splittings of $\Delta e(x = 0) = 37.734\,\mathrm{meV}$ and $\Delta e(x = 3) = 48.91\,\mathrm{meV}$. As the repulsion potential should vary only slowly with the stoichiometry, we assumed that $U(x) = Ax+B$ so that $J_0(x) = \frac{\Delta e(x)^2}{Ax+B}$. From the calculated splitting values and the reported interaction constants $J_0^{\mathrm{Ba}} = 2.38\,\mathrm{meV}$[95] and $J_0^{\mathrm{Ba}} = 5.55\,\mathrm{meV}$[86], we obtained $A = -55.8\,\mathrm{meV}$ and $B = 598\,\mathrm{meV}$. The interaction constants taken from Refs. [86] and [95] were obtained from measurements at $1.7\,\mathrm{K} \leq T \leq 6\,\mathrm{K}$, which is approximately the same temperature as for our neutron diffraction experiments. Based on the calculated values for A and B, we could estimate the value of the repulsion potential U for all examined values of x. As we assumed U to be temperature independent, the same values of $U(x)$ were used to calculate for J_0 at low temperature and at room temperature from the calculated splittings $\langle \Delta e \rangle$.

In Fig. 3.30, we have plotted the values of J_0 from section 3.4 together with the results of our calculations of J_0 at room temperature and at $T = 2\,\mathrm{K}$. The experimental values for J_0 are most sensitive to the low-temperature magnetization part of $M(T)$ used for the fitting procedure. Therefore, these experimental values are valid well below room temperature. Fig. 3.30 demonstrates, as expected, that the experimental values can be well reproduced within the EHTB framework if the corresponding calculations are based on the low temperature structure. However, the obtained room temperature values of J_0 underestimate the experimental values for a wide range of x. On the other hand, the experimental values and the calculations for both the room temperature and low

temperature structure almost coincide for a Sr content of $x \approx 1.33$. For this composition, our neutron diffraction experiments did not indicate any evidence for the structural symmetry breaking that we observed for the other values of x at $T = 2\,\mathrm{K}$. Furthermore, when combining Fig. 3.29 and Fig. 3.30, a larger value of J_0 seems to be accompanied by a stronger symmetry breaking.

Hence, we conclude that the Jahn-Teller distortion, which induces an orbital ordering [88, 101], increases the intradimer interaction constant J_0, as it was reported for $Sr_3Cr_2O_8$. Without this orbital ordering, the splitting $\langle \Delta e \rangle$ for a given x remains almost constant for all temperatures. We predict that no (or just a minimal) distortion would be found for stoichiometries with experimental values of J_0 close to the calculated room temperature results.

3.9 A possible explanation of the suppressed structural transition by chemical disorder

To provide an explanation for the suppressed Jahn-Teller distortion, we analyzed the structural data obtained at room temperature in search for non-linearities as a function of the Sr content x. As described in section 3.7, the occupation probability for Ba at site A_1 for intermediate stoichiometries is enhanced with respect to a completely random case and vice versa for site A_2. Albeit, the occupation preferences are not very pronounced and do not fully coincide with the suppression of the Jahn-Teller distortion. In addition, these site preferences do not directly break the site symmetry of the Cr^{5+} ions, so that a Jahn-Teller distortion could still be energetically favorable. As shown in Fig. 3.23, the average bond valence sum for both Ba sites takes the value +2 for all studied compositions. Similarly, the bond valence sum for the Cr ions is almost constant as a function of x. This means that, on average, the electronic energies of the Cr orbitals do not change as a function of x so that a Jahn-Teller distortion should be equally favorable for all examined stoichiometries. However, the bond valence sum is calculated based on the average distance between the atomic cores without taking local deviations from this average into account. This is also true for the site symmetry so that the local symmetry for a given atom can be lower than the average global one.

Due to the very different ionic radii of Ba^{2+} and Sr^{2+}, we can expect strong local deviations of the site symmetry and energy of the electronic orbitals due to local atomic distances that deviate from the global average. The variation of the atomic distances is strongly dependent on the Sr content, as shown by the variation of the mean square displacements $\langle u^2 \rangle$. These mean square displacements, obtained from the structural refinement and shown in Fig. 3.31, are found to be maximum for intermediate values of x. We attribute this behavior to an increase of the local disorder as it is common for solid solutions.

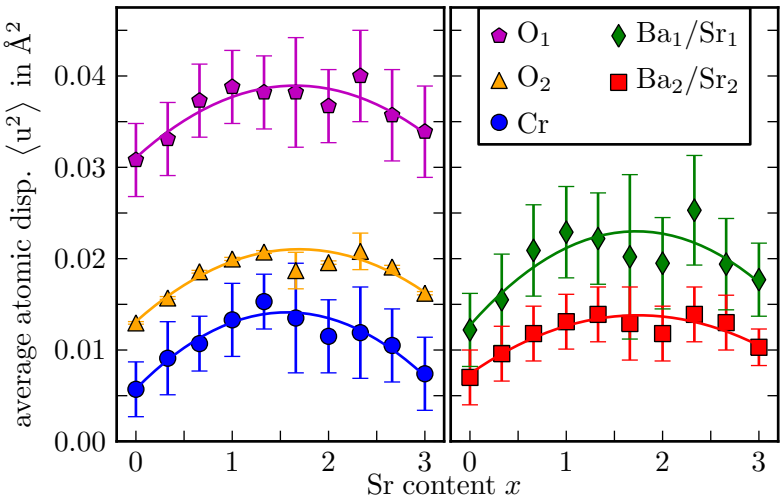

Abbildung 3.31: Atomic displacements $\langle u^2 \rangle$ in $Ba_{3-x}Sr_xCr_2O_8$ at room temperature as a function of the Sr content x. The solid lines are guides to the eye.

To obtain an estimate for this disorder contribution, we have assumed that u comprises a thermal and a disorder term, $u = u_T + u_D$, with no correlation between u_T and u_D. Therefore, the total mean displacement would be $\langle u^2 \rangle = \langle u_T^2 \rangle + \langle u_D^2 \rangle + 2\langle u_D u_T \rangle = \langle u_T^2 \rangle + \langle u_D^2 \rangle$. We have assumed the thermal part to be linear in x, $\langle u_T^2 \rangle (x) = \rho x + \tau$, and calculated the corresponding values for ρ and τ based on $\langle u^2 \rangle$ for $x = 0$ and $x = 3$. We subtracted this thermal part from the experimentally obtained displacements and plotted the resulting $\langle u_D^2 \rangle (x)$ in Fig. 3.32. We have also calculated the variance $\sigma = \langle (d - \langle d \rangle)^2 \rangle$ of the distances d in the oxygen tetrahedra around the Cr^{5+} ions as changes in these distances affect J_0 most strongly. The square root of this variance (see Fig. 3.33) also shows a maximum for intermediate Sr concentrations, indicating a strong disorder.

We believe that it is this type of disorder which is responsible for suppressing the Jahn-Teller induced structural phase transition. While for pure $Ba_3Cr_2O_8$ and $Sr_3Cr_2O_8$, all Cr-O distances are well defined, the different distributions of Sr/Ba-ions inside the unit cell lead to an increasing width of the distribution of Cr-O distances for intermediate values of x. The symmetry at the Cr site is therefore broken locally and preserved only on average. This symmetry breaking lifts the degeneracy of the e_g state by an energy difference $\Delta E(x)$. As $\Delta E(x)$ increases, the possible energy gain associated with the structural phase transition is lowered, and therefore this transition is gradually suppressed.

The chemical disorder also gives an adequate explanation for the broadening of the ESR lines described in section 3.6. As described in section 3.1, the overlap and the energies of the electronic orbitals determine the value of the interaction constant J_0. Thus, the disorder leads to a distribution of J_0's in the sample instead of a single value so that the excitation of dimers requires lower or higher excitation energies, depending on the

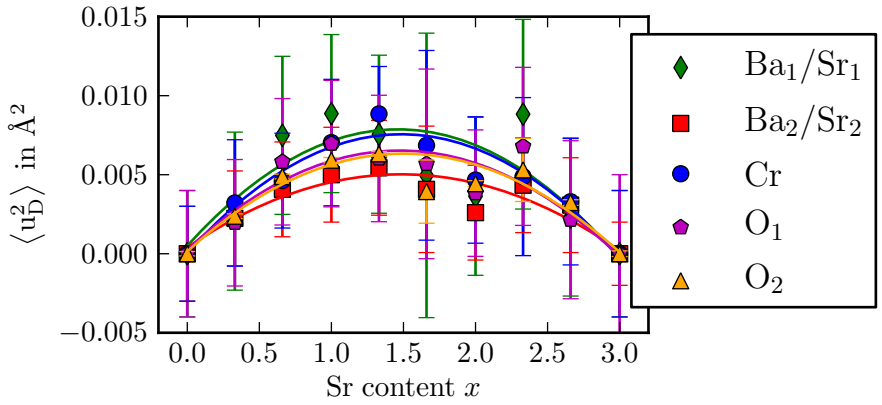

Abbildung 3.32: Estimated disorder contribution to the atomic displacements, $\langle u^2 \rangle$, in $Ba_{3-x}Sr_xCr_2O_8$ at room temperature as a function of the Sr content x. The solid lines are guides to the eye.

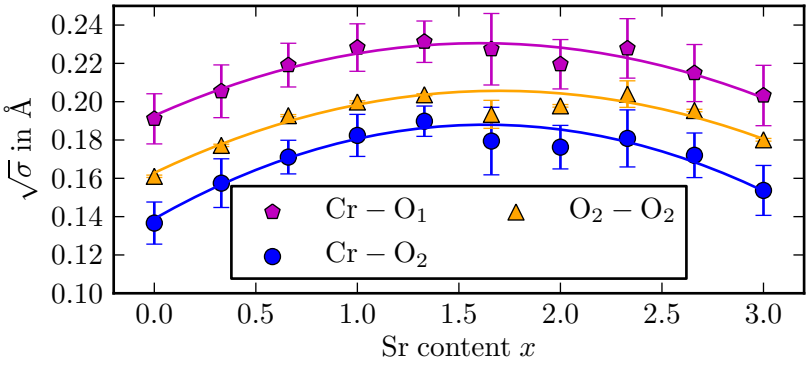

Abbildung 3.33: Square root of the variance of atomic distances relevant to the electronic energies in the oxygen tetrahedron surrounding the Cr ions and for the interaction constant J_0 as a function of the Sr content x. The solid lines are guides to the eye.

environment.

Interestingly, $\langle u_D^2 \rangle (x)$ does not seem to be symmetric with respect to $x = 1.5$, as it would be expected for entirely random distributions, but seems to be shifted to slightly smaller values of x. This could be due to the changing occupation probabilities for large values of x. Any deviation from a completely random distribution, i.e. any difference between the dashed lines and the experimental values in the top of Fig. 3.25, would lower the total disorder (related to the Shannon entropy in [114]). We have therefore calculated the Shannon entropy S, given by the different possible distributions α of Ba and Sr inside the unit cell, as

$$S_{\mathrm{Ba/Sr}} = -\sum_{\alpha} P_\alpha \ln P_\alpha. \tag{3.11}$$

Here P_α is the probability for a given arrangement, calculated based on the obtained occupancies.

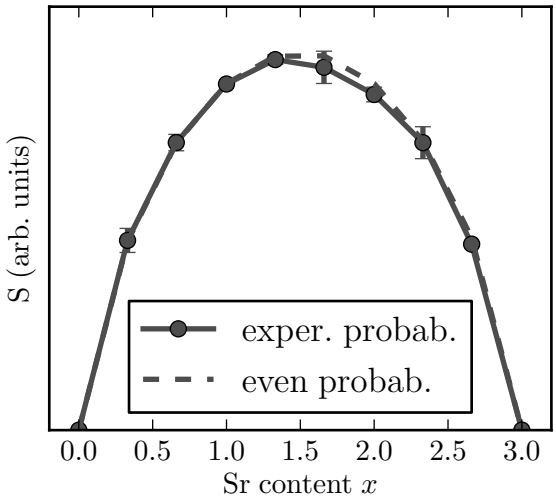

Abbildung 3.34: Shannon entropy S as a function of the Sr content x for the cases of even occupation probabilities and the experimentally obtained occupation probabilities.

In Fig. 3.34, we have plotted the entropy $S^{\mathrm{exp}}(x)$ that is based on the experimental occupation probabilities for sites A_1 and A_2 (see Fig. 3.25) along with the entropy S^{even} that is based on even occupation probabilities (dashed lines in Fig. 3.25 with included site multiplicity). The experimental entropy $S^{\mathrm{exp}}(x)$ is maximum around $x \approx 1.25$, similar to the $\langle u_D^2 \rangle$ (see Fig. 3.32), which coincides also with the minimum for the interaction constant J_0 (see Fig. 3.30). Therefore, the observed asymmetry of $\langle u_D^2 \rangle (x)$ could indeed be induced by the changing occupation probabilities for the different sites. However, as the difference between $S^{\mathrm{exp}}(x)$ and S^{even} is small and of the order of the calculated

uncertainty, our experimental sensitivity with respect to the atomic displacements and site occupancies is not sufficient to unambiguously confirm this explanation for the observed asymmetry of $\langle u_D^2 \rangle (x)$.

3.10 Disorder effects probed by low-frequency ESR techniques

As stated above, the structural phase transition leads to an increase of J_0 by enhancing the splitting Δe of the e_g-levels that occurs when two CrO_4^{6-}-tetrahedra are brought together (see Fig. 3.28). Furthermore, the e_g-states of the single tetrahedra are split by an energy Δ_O into the low lying $3z^2 - r^2$-orbital and the energetically higher $x^2 - y^2$-orbital (see Fig. 3.35).

For $Sr_3Cr_2O_8$, it has been shown that Δ_O greatly influences the low frequency ESR spectra [105]. The spins that are excited by the microwave radiation dispense the excitation energy by spin-lattice relaxation, e.g. interacting with phonons in the system. In the present case, two relaxation processes are relevant[115]. The first is the direct process, where the absorbed microwave energy $h\nu$ is converted into a phonon of the same energy. At low temperatures, this contribution changes only slightly with temperature. The second contribution comes from an Orbach-process (see Fig. 3.35). Here the excited electron (I) absorbs a phonon of energy Δ_O to occupy a higher orbital (II). Afterwards, a phonon with energy $\Delta_O + h\nu$ is created so that the electron is again in the original state (III). As this process requires the existence of a phonon with energy Δ_O, the Orbach-contribution is exponentially diminished with decreasing temperature so that the lifetime τ of the microwave excitation can at low temperatures be described by[115]:

$$\frac{1}{\tau} = A + \frac{B}{e^{\frac{\Delta_0}{k_B T}} - 1}, \tag{3.12}$$

where k_B is the Boltzmann constant. For a system without structural disorder, the observed ESR linewidth when sweeping the magnetic field for a given ESR frequency is inversely proportional to this lifetime. However, in the case of $Ba_{3-x}Sr_xCr_2O_8$, the local environment of the ESR active Cr^{5+} ions varies from site to site. As this variation should lead to corresponding changes in the local crystal field, the ESR linewidth should increase. Similar to Eq. 3.12, we can describe the ESR linewidth ΔB for the dimer system as

$$\Delta B = a + \frac{b}{e^{\frac{\Delta_0}{k_B T}} - 1}, \tag{3.13}$$

where a is composed of the direct spin-lattice relaxation as well as a disorder related broadening term, and b gives the Orbach-relaxation component. Following the discussion of chemical disorder and its influence on the structural symmetry breaking in

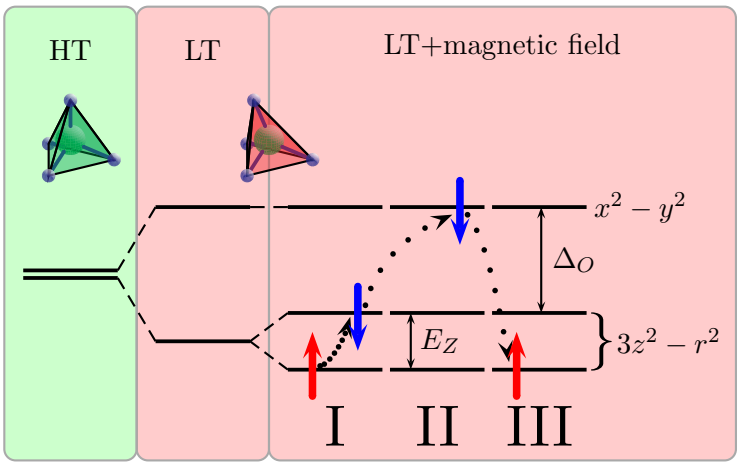

Abbildung 3.35: Sketch of the energy levels involved in the Orbach relaxation of the excited spin states. On the left the energy levels for the high temperature crystal structure without Jahn-Teller distortion are shown. On the right the energy levels for the distorted low temperature structure are shown with the arising energy difference Δe_O between the $3z^2 - r^2$ and the $x^2 - y^2$ orbital and the field dependent Zeeman energy E_Z. The ratio between Δ_O and E_Z is much larger than the sketch suggests: while for X-band ESR experiments $E_Z \approx 0.04\,\text{meV}$, Δ_O is of the order of 10 meV. Therefore, the Zeeman splitting of the $x^2 - y^2$-orbital can be neglected and is not accounted for in the picture.

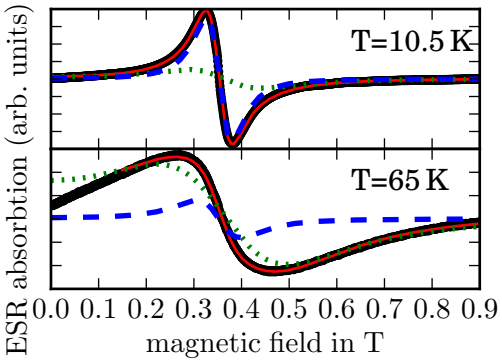

Abbildung 3.36: ESR absorption spectra for $Ba_{0.3}Sr_{2.7}Cr_2O_8$ at $T = 10.5\,\mathrm{K}$ (top) and $T = 65\,\mathrm{K}$ (bottom). The experimental absorption is given by the black symbols while the red line corresponds to the fit by two combined Lorentzian lines. The dimer contribution is marked with a dotted green line, the paramagnetic contribution is given as blue dashed line.

$Ba_{3-x}Sr_xCr_2O_8$, one would expect that a increases for intermediate x due to the increasing disorder. The energy splitting Δ_0, on the other hand, should be decreased for intermediate x due to the gradual suppression of the Jahn-Teller distortion, as described in the previous sections.

To test this model, we have performed corresponding ESR experiments for several values of x using a *Bruker EMX* spectrometer (see section 2.3.1). The spectra, taken at different temperatures, have been fitted using a differential Lorentzian lineshape. For values of x that differed substantially from $x = 3$ it was necessary to take a second resonance line due to the increasing paramagnetic background into account (see Fig. 3.36). From these fits we obtained the resonance fields, the width and the relative intensity of the two lines. As the ESR absorption is proportional to the susceptibility of the sample, the relative intensity of the two lines should correspond to the two parts of the magnetization discussed in section 3.4. Concordantly, we fitted the dimer contribution to the ESR intensity based on the Bleaney-Bowers formula (see Eq. 3.9), while the paramagnetic contribution was fitted based on the Brillouin function (see Eq. 3.10). In both cases, the agreement between the model and the experimental data is reasonably good (see Fig. 3.37). The g-factor was calculated based on the extracted resonance fields B_{res} for each line as $g = \frac{h\nu}{\mu_B B_{\mathrm{res}}}$ with $\nu = 9.56\,\mathrm{GHz}$.

However, with increasing temperature the ESR lines became strongly distorted in low magnetic fields (see Fig. 3.36, bottom panel). In this field region, the line could not be correctly described as a Lorentzian function anymore. We therefore restricted the fit for each temperature to the field region were this distortion was less apparent. Nevertheless, the exact resonance field could not be reliably determined. The obtained g-factor is therefore only based on the mean value of the resonance fields for temperatures below $T = 55\,\mathrm{K}$. Interestingly, this g-factor decreases for intermediate values of x, in qualitative

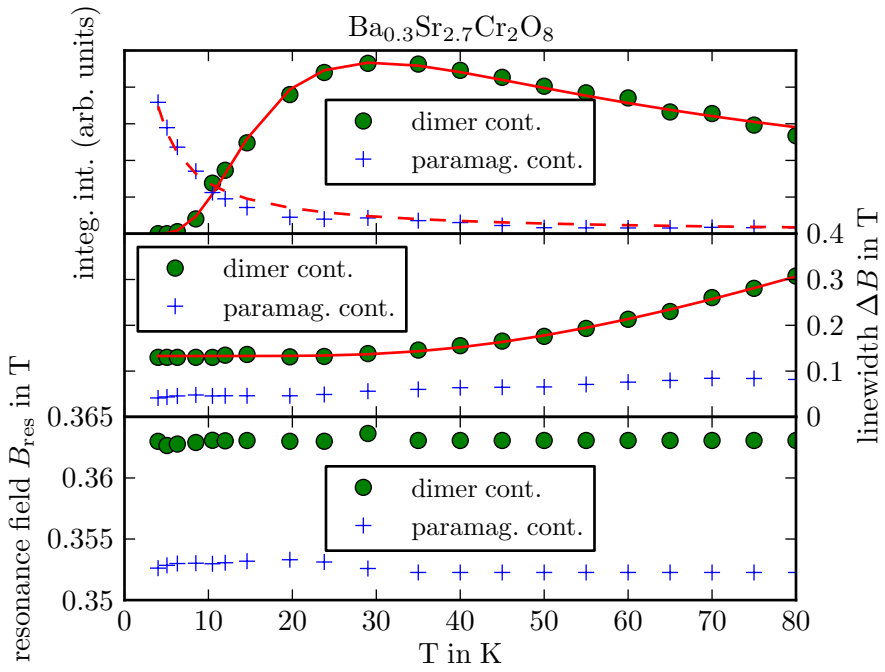

Abbildung 3.37: Results of an analysis of the ESR resonance lines of $Ba_{0.3}Sr_{2.7}Cr_2O_8$ as a function of the temperature. The top panel shows the intensity with the corresponding fits according to Eqs. 3.9 and 3.10. The middle panel presents the ESR linewidth with a fit to the dimer part according to Eq. 3.13. In the bottom panel, the position of the resonance field is plotted.

agreement with the result from section 3.6 (see Fig. 3.38, bottom panel).

The width of the dimer resonance line has been fitted according to Eq. 3.13 to extract the baseline a and the energy splitting Δ_O. These values also are shown in Fig. 3.38. This baseline, partly representing the effect of the chemical disorder, increases for intermediate values of x, as expected. On the other hand, Δ_O decreases for $x < 3$, indicating a smaller energy splitting due to the gradually suppressed Jahn-Teller distortion. The here presented ESR data are thus in agreement with our results from magnetization experiments, neutron diffraction and EHTB calculations. Unfortunately, it was not possible to examine the low frequency ESR properties for stoichiometries closer to $x = 1.5$ due the increasing distortion of the ESR line.

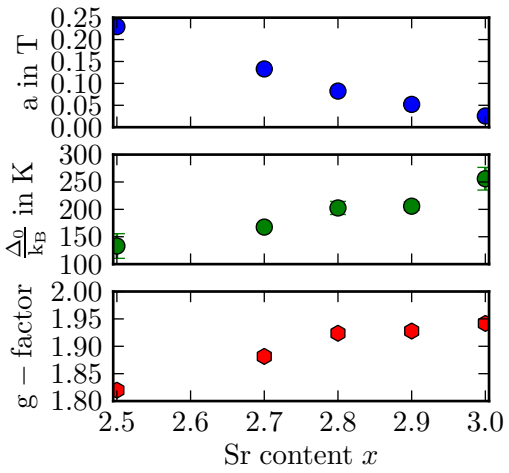

Abbildung 3.38: The g-factor and the parameters describing the temperature evolution of the width of the dimer contribution to the ESR spectra according to Eq. 3.13 as a function of the Sr content x. Top: baseline a, middle panel: energy splitting Δ_O, bottom: g-factor.

3.11 Examination of the critical field of $Ba_{3-x}Sr_xCr_2O_8$ using pulsed high-field magnetometry

As shown in the previous chapters, the interaction constant J_0 and along with it the spin gap are reduced for intermediate values of x. This reduction should reduce the critical field of the triplon condensation. To examine this expected change of the critical field for decreasing values of x, we have performed magnetometry experiment in pulsed magnetic fields at the HZDR in Dresden-Rossendorf. The experimental details are described in section 2.1.2.

To extract the critical field based on magnetization data, we make use of the fact that the condensation of interacting triplons is a second order phase transition [42], which means that the second derivative of the Gibbs free energy $G(H,T)$ shows a discontinuity[116]. This discontinuity leads to a corresponding singularity in the corresponding third derivative[2]. As the first derivative is the magnetization itself, we have:

[2]Naturally, this third derivative is then not the simple derivative of the second derivative, but defined similarly to the delta-distribution as a derivative of the Heavyside-function.

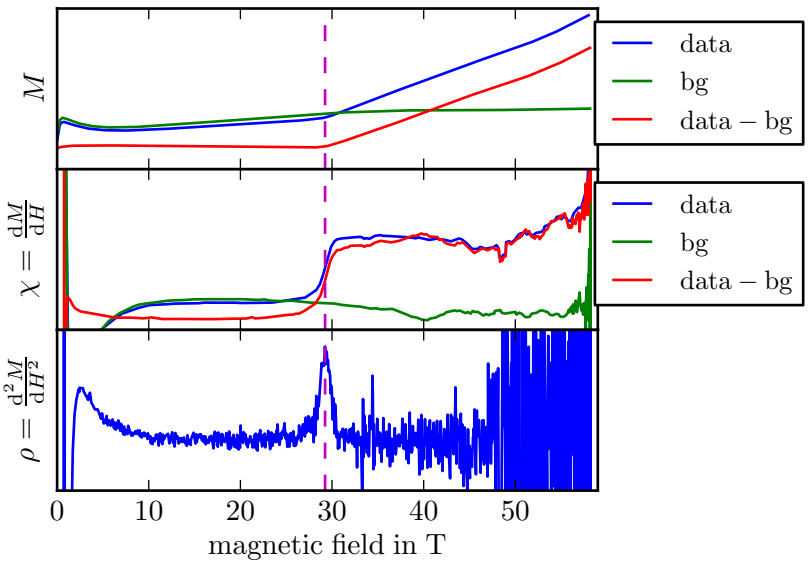

Abbildung 3.39: Magnetic moment M, susceptibility χ and field derivative ρ of the susceptibility obtained for $Ba_{0.1}Sr_{2.9}Cr_2O_8$ at $T = 1.4\,\mathrm{K}$ and the corresponding background measurement. The dashed line marks the critical field H_{c1} obtained from the local extremum of ρ.

$$M(H,T) = -\frac{\partial}{\partial H}G$$
$$\chi(H,T) = \frac{\partial}{\partial H}M = -\frac{\partial^2}{\partial^2 H}G$$
$$\rho(H,T) = \frac{\partial}{\partial H}\chi = -\frac{\partial^3}{\partial^3 H}G.$$

We have therefore determined the critical field as the extremal point of $\rho(H)$, where $\rho(H)$ has been calculated based on the uncorrected experimental data. In Fig. 3.39, we have plotted a corresponding measurement for for $Ba_{0.1}Sr_{2.9}Cr_2O_8$ at $T = 1.4\,\mathrm{K}$. As expected, the magnetization is almost constant up to H_{c1}. The susceptibility χ shows a clear step, while the corresponding derivative ρ exhibits a peak at the transition field. However, the peak is broadening and becomes asymmetrical for intermediate values of x (see Fig. 3.40). We believe that this is due to the above explained distribution of the intradimer interaction constant J_0 which leads to a closing of the spin gap at lower magnetic fields for dimers with a smaller value of J_0. Despite the observed broadening, we have determined the critical field as the extremal point of $\rho(H)$ for all temperatures and values of x. In Fig. 3.40, we have plotted $\rho(H)$ for all examined samples at $T \approx 1.4\,\mathrm{K}$. The obtained critical field decreases for intermediate values of x, in accordance with the above described change of J_0.

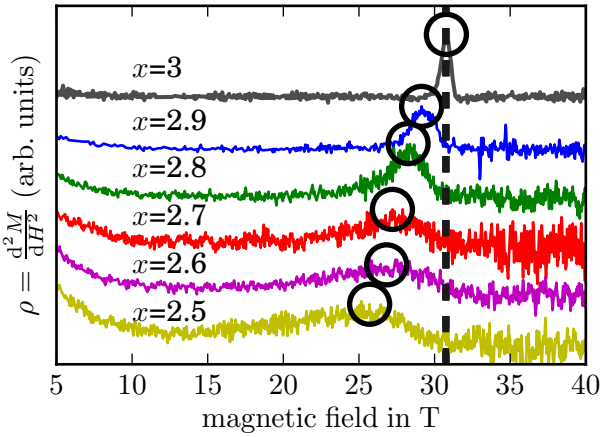

Abbildung 3.40: Derivative ρ of the susceptibility as function of the external magnetic field for $Ba_{3-x}Sr_xCr_2O_8$. The black circles mark the critical points of ρ while the dashed line marks the reported critical field in pure $Sr_3Cr_2O_8$ at $T = 1.5\,\mathrm{K}$ from Ref. [86].

In Fig. 3.41, we have plotted the resulting phase boundary $T_c\,(\mu_0 H)$ for the examined powder samples with $x \in (2.8, 2.9, 3)$. For comparison, we have plotted the critical points reported for single crystalline $Sr_3Cr_2O_8$, as well. The critical field reported in Ref. [86] has also been obtained based on the extraction magnetization technique while the phase boundary reported in Ref. [37] has been determined by measuring the heat capacity and the magnetocaloric effect of the sample.

As expected, the critical temperature increases with increasing external magnetic field so that a dome-like phase boundary is still present, similar to the pure compounds (see Fig. 3.41). However, the phase boundaries of the mixed solid solution extend to higher temperatures and the respective critical fields H_{c1} are lower than in the pure compounds, as expected. Interestingly, the phase boundaries for $x = 2.8$ and $x = 2.9$ seem to cross around $T = 4\,\mathrm{K}$. The reason for this crossing is unclear up to now. It has been reported, however, that the critical fields obtained based on the extraction magnetization technique do not always coincide with those obtained from purely thermodynamic measurements[54, 58, 117, 59]. To the best of our knowledge, this problem seems to be exclusive to the system $A_3B_2O_8$, where A$\in$ {Ba,Sr} and B$\in$ {Cr,Mn}. For other candidates for a BEC of magnetic quasiparticles such as $TlCuCl_3$, $KCuCl_3$, $Pb_2V_3O_9$ or $NiCl_2(SC(NH_2)_2)_4$, this discrepancy has not been reported.

For $Ba_3Cr_2O_8$ and $Sr_3Cr_2O_8$, only very few measurements of these phase boundaries using the extraction magnetization technique have been published, so that, up to now, no satisfying explanation for this discrepancy can be found in the literature. Interestingly, the critical fields that we have determined for $Sr_3Cr_2O_8$ on powder samples using the extraction magnetization technique do agree quite well with the phase boundary reported from measuring the heat capacity and and the magnetocaloric effect (see Fig. 3.41). Thus,

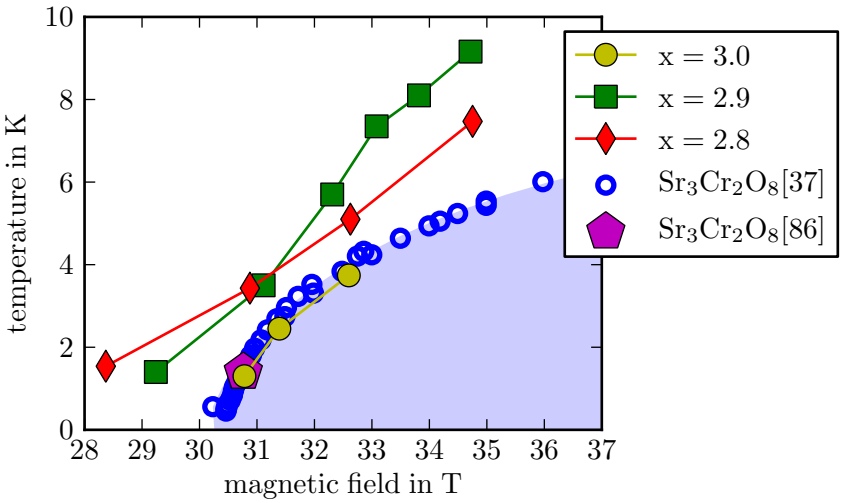

Abbildung 3.41: Obtained critical temperatures as a function of the external magnetic field H powder samples of $Ba_{3-x}Sr_xCr_2O_8$ with $x \in (3, 2.9, 2.8)$ in comparison to the reported values for single crystalline $Sr_3Cr_2O_8$ (see text).

it seems that only the critical fields obtained for single crystalline samples depend on the used experimental technique. Therefore, we are confident that the critical fields that we have deduced for $x < 3$ and plotted in Fig. 3.41 are the true critical fields for the triplon BEC.

In Fig. 3.42, we have plotted the interaction constant J_0 elicited from low field magnetization experiments and the corresponding lower critical fields H_{c1} as a function of x. The almost linear change of H_{c1} does not exactly follow the observed change of J_0. One possible reason is that both the intradimer and interdimer interaction constants are relevant for the value of H_{c1}. The Jahn-Teller distortion found in $Ba_3Cr_2O_8$ and $Sr_3Cr_2O_8$ both increases J_0 and decreases J'. Thus, a gradual suppression of the distortion should not only lead to a decrease of J_0, but also to an increase of J', thereby contributing both to the observed change of the critical field.

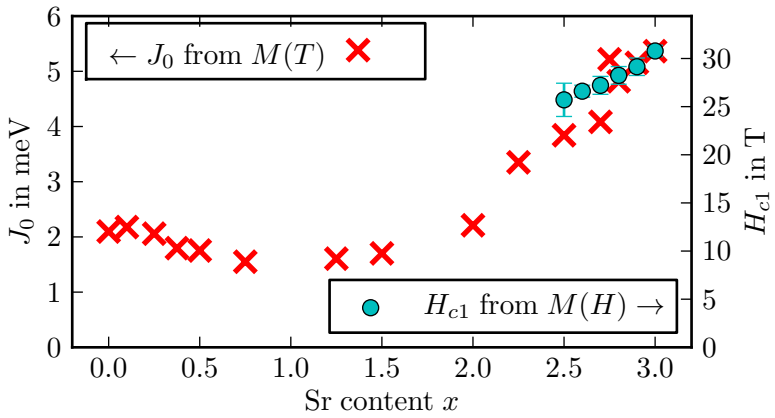

Abbildung 3.42: Experimentally obtained intradimer interaction constant J_0 and lower critical fields H_{c1} for $Ba_{3-x}Sr_xCr_2O_8$. The axes are scaled in such a way that the data points for $Sr_3Cr_2O_8$ are at the same position.

4 Experiments on $NiCl_2(SC(NH_2)_2)_4$ (DTN)

Our interest in Dichlorotetrakis(thiourea)nickel (DTN) has been motivated by our search for suitable materials for the construction of a Josephson device as described in section 1.3. DTN has been identified as a candidate for a BEC of magnetic quasiparticles [42] and the respective critical fields have been shown to be changeable by gradually replacing Cl with Br [118] (Br-DTN), so that we decided to perform ESR experiments to probe the energy spectra of DTN, Br-DTN and a corresponding coupled device.

4.1 General properties of DTN

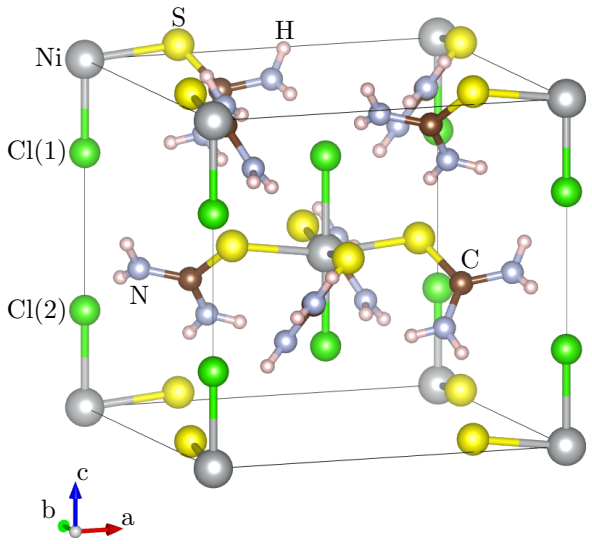

Abbildung 4.1: Crystal structure of DTN.

DTN has first been prepared several decades ago in single crystalline form as part of a program to analyze the structural properties of certain free molecules in comparison to their crystalline version [119]. The conducted structural characterization of DTN using X-ray diffraction identified the compound as a tetragonal system (see Fig. 4.1) with Ni^{2+} ions [119], leading to a spin of $S_{Ni} = 1$. These Ni spins interact with each other along

the c-axis, forming S=1 spin chains. The corresponding interaction constant J_c is given by the super-super-exchange path through the Cl atoms in between. The additional interaction $J_a = J_b$ between the chains is very weak as there is no chemical bond between Ni ions from different chains. The thiourea molecules ($SC(NH_2)_2$), that merely serve as spacer between the Ni-Cl chains and have no large influence on the magnetic interactions, can be omitted to simplify the structural visualization. When also omitting the Cl atoms, the structure is given by two interpenetrating tetragonal arrangements of Ni ions (see Fig. 4.2). It has been established relatively early that DTN and similar compounds with S=1 ions [120, 121] undergo a field-induced magnetic ordering below a critical temperature in strong enough magnetic fields. As such a magnetic ordering is, *per se*, not an unusual phenomenon, only few additional investigations have been undertaken for several decades. However, after the explanation of the magnetic ordering in $TlCuCl_3$ in terms of a BEC of magnetic quasiparticles, interest in DTN has been renewed. Besides analyzing the spin dynamics, the thermodynamic properties of the ordering transition itself have been probed [42, 57] to examine the universality class of the transition. In addition, the system has also been studied extensively using ESR techniques and motivated a broad spectrum of theoretical work [122, 123, 124, 125, 126, 127]. As these investigations required high quality single crystalline samples, they have benefitted from the long experience of Prof. Armando Paduan-Filho (University of São Paulo) who also prepared all the DTN samples used in the present work. The single crystals of DTN are prepared by dissolving nickel chloride in a saturated aqueous solution of thiourea [120]. Slow recrystallization yields crystals with a mass of up to 100 mg, while for the below presented ESR experiments, samples with a total mass of less than 20 mg have been used. Samples used in the ESR experiments that consisted fully or partly of Br-DTN were prepared with a Br concentration of about $x = 0.13$.

One-dimensional model

To first approximation, one can think of DTN as a system of uncoupled chains. These chains consist of $S = 1$ spins with a distance c between them and an antiferromagnetic interaction constant J_c. In addition to this spin-spin interaction, a magnetic anisotropy D leads to an easy xy-plane. Thus, the Hamilton operator can be written as

$$\hat{H} = \sum_n \left(D\,(S_n^z)^2 + J\hat{\vec{S}}_n \cdot \hat{\vec{S}}_{n+1} + g\mu_B\mu_0\hat{\vec{H}}_n \cdot \hat{\vec{S}}_n \right). \tag{4.1}$$

Each of the spins can be oriented antiparallel, perpendicular or parallel to an applied external magnetic field (states $|1\rangle$,$|0\rangle$ or $|-1\rangle$). Partially following Ref. [128], we will describe these as *single ion bound state*, non-magnetic state and *ferromagnetic state*, respectively. The ground state in zero magnetic field is non-magnetic with all spins oriented perpendicular to the c-axis (state $|0\rangle$). The excitation spectrum $\omega(k)$ can be calculated based on different approximations [42, 129], but we will adopt the description

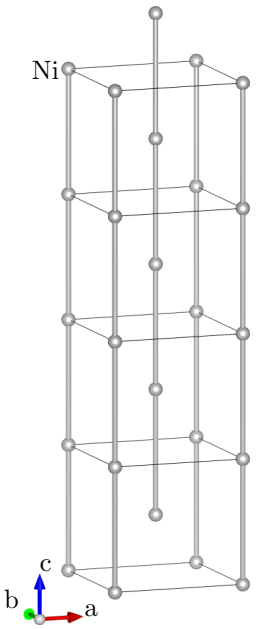

Abbildung 4.2: Simplified structure of DTN, showing only the Ni chains along the c-axis.

given in Refs. [126] and [128], where the dispersion has been calculated up to the third order in $\frac{1}{D}$ to

$$\begin{aligned}\hbar\omega(k) = {} & D + 2J\cos(ck) \\ & + \frac{J^2}{D}\left(1 + 2\sin^2(ck)\right) \\ & + \frac{J^3}{D^2}\left(2\sin^2(ck) - \frac{1}{2}\left(1 + 8\sin^2(ck)\right)\cos(ck)\right).\end{aligned}$$

For non-zero, but small magnetic fields H with $g\mu_B\mu_0 H < D - 2J + \frac{J^2}{D} + \frac{J^3}{2D^2}$ (region I in Fig. 4.3), the energy for the two excited states $|1\rangle$ and $|-1\rangle$ is thus given by

$$\hbar\omega_\pm(k) = \hbar\omega(k) \pm g\mu_B\mu_0 H, \tag{4.2}$$

as sketched in Fig. 4.4. The smallest energy gap Δ occurs at the border of the Brillouin zone at $ck = \pi$. Once the magnetic field is large enough to overcome this gap, $H = H_{c1} = \frac{\Delta}{g\mu_B\mu_0}$, the new ground state is given by a mixture of $|0\rangle$ and $|-1\rangle$. Although the exact properties of the spin states above H_{c1} are difficult to obtain, the ground state should become increasingly *ferromagnetic* as the magnetic field increases. However, once the applied field is high enough to again separate the $|0\rangle$ state and the $|-1\rangle$ state at $H = H_{c2}$ (region II in Fig. 4.3), the system is completely polarized and the ground state is given by the ferromagnetic state. The lowest excited state is then non-magnetic with the dispersion relation [128]

$$\hbar\omega(k) = g\mu_B\mu_0 H - D + 2J(\cos(ck) - 1). \tag{4.3}$$

In addition, a two magnon-continuum develops with energies between

$$\hbar\omega_{2\mathrm{m}}(\kappa) = 2g\mu_B\mu_0 H - 2D - 4J\left(1 \pm \cos\left(\frac{c\kappa}{2}\right)\right). \tag{4.4}$$

A two-magnon state can be understood as two magnons with momenta k_1 and k_2 that are simultaneously excited, but move in opposite directions ($k_1 \uparrow\downarrow k_2$). Their individual momenta differ by the total momentum $\kappa = k_1 - k_2$. As each of the magnons has $S^z = 1$, exciting these two-magnon states from the completely polarized ground state requires a spin transfer of $\Delta S^z = 2$. These excitations can therefore only be observed if the system is not perfectly axially symmetric so that the states are mixed even for zero field.

Above the two-magnon continuum, the so called *single ion bound state* can be found with the dispersion

$$\hbar\omega_{\mathrm{si}}(\kappa) = 2g\mu_B\mu_0 H - 4J \tag{4.5}$$

$$+ 2\left(\frac{J^2}{D} + \frac{J^3}{D^2}\right)\cos^2\left(\frac{k}{2}\right). \tag{4.6}$$

This state, that has been first calculated by Silberglitt *et al* [130], can be understood as a spin excitation with a double spin flip ($|-1\rangle \rightarrow |1\rangle$) at one site instead of the two spin flips at different sites in the case of the two-magnon continuum. This double spin flip also requires $\Delta S^z = 2$, so that a violation of the axial symmetry is required for an excitation by ESR radiation, as in the case of the two-magnon continuum. The single ion bound state is only very weakly dispersive, with a minimum at the border of the Brillouin zone. The excitation energy from the ground state is thus mainly given by the external field.

In Fig. 4.3, we have sketched the ESR excitation spectrum for the two cases $H < H_{\mathrm{c1}}$ and $H > H_{\mathrm{c2}}$ and the underlying spin wave dispersions. As ESR-experiments on DTN have indicated a broken axial symmetry [122], we will assume that $\Delta S^z = 2$ transitions can be excited. Furthermore, we ignore possible resonances due to the two-magnon continuum. In region I of Fig. 4.3, three possible ESR modes are shown. As $|0\rangle$ is the ground state of the system, lines A ($|0\rangle \rightarrow |1\rangle$) and B ($|0\rangle \rightarrow |-1\rangle$) will have a non-vanishing intensity at all temperatures. As the ground state has a a vanishing momentum, these two transitions can only take place at the center of the Brillouin zone. The line H corresponds to a transition $|-1\rangle \rightarrow |1\rangle$ between the two excited states. Due to the dispersive nature of both states, this transition can occur over the entire Brillouin zone. At very low temperature and small magnetic fields, $|-1\rangle$ can not be thermally populated so that the line H vanishes for $T \rightarrow 0$.

In region II, the ESR spectrum becomes somewhat more evolved. As $|-1\rangle$ is now the ground state, transitions from $|-1\rangle$ to $|1\rangle$ can be observed even for $T \rightarrow 0$ so that the E-line should always have a non-vanishing intensity. Although being the high field analogue to resonance H, transition E can only occur at the center of the Brillouin

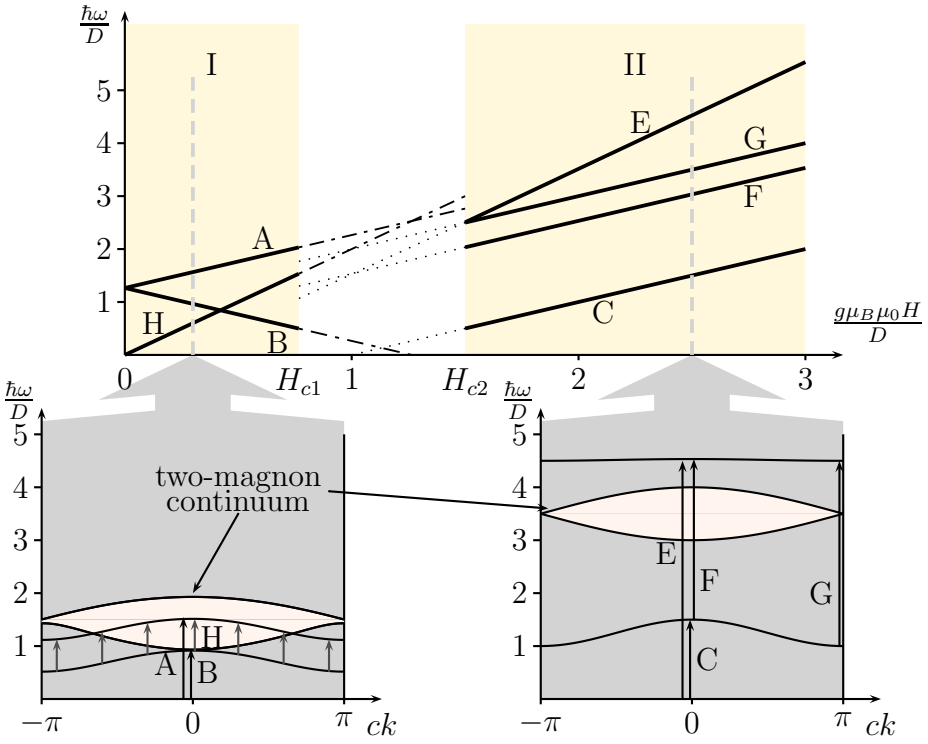

Abbildung 4.3: Calculated frequency-field diagram (top) and corresponding spin dispersion (bottom) for a one-dimensional system of antiferromagnetic spin chains. The notation has been adopted from Ref. [126]. As the exact dispersion relation for the intermediate region $H_{c1} < H < H_{c2}$ is not known, the dotted and dash-dotted lines are only extrapolations from regions I and II. The calculations are based on Tab. 4.1 with $\frac{J}{D} = \frac{1}{8}$ in magnetic fields of $\frac{g\mu_B\mu_0 H}{D} = 0.3$ and 2.5, respectively. The critical fields H_{c1} and H_{c2} can not be probed directly with ESR experiments, similar to $Ba_3Cr_2O_8$ (see Figs. 3.3 and 3.7).

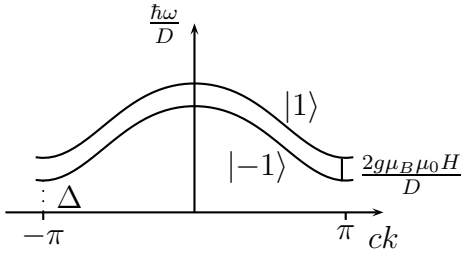

Abbildung 4.4: Energy $E(k)$ in terms of the anisotropy constant D of the spin excitations from the $|0\rangle$ ground state in one dimension for small magnetic fields H (see text).

zone. The same holds for the C-line, corresponding to $|-1\rangle \rightarrow |0\rangle$. In addition to those excitations from the ground state, transitions between higher states can also be observed at finite temperatures, but again will vanish for $T \rightarrow 0$. These higher excitations are given by lines F and G. Line F, corresponding to the transition $|0\rangle \rightarrow |1\rangle$ is the high field analogue to resonance A. This transition can now occur over the entire Brillouin zone, giving rise to a band of excitations. Excitation F, taking place at $k = 0$, is the lower boundary of this band, while the upper boundary is given by line G. The latter occurs at the border of the Brillouin zone. At $H = H_{c2}$, when the gap between $|-1\rangle$ and $|0\rangle$ is still closed at $k = \pi$, the non-magnetic state will be populated for all temperatures so that line G will not vanish even for $T \rightarrow 0$, contrary to line F. This is especially true for the intermediate region with $H_{c1} < H < H_{c2}$, where the gap is closed for all fields [131]. The dependency of the ESR frequencies on the applied external field, the anisotropy and the spin interaction constant are summarized below in Tab. 4.1.

For the ESR resonances that occur in region I or II, one would expect a somewhat smooth continuation into the intermediate region with $H_{c1} < H < H_{c2}$ (see dotted and dash-dotted lines in 4.3), albeit with decreasing intensity. However, one should also expect a deformation of the lines. This is caused by a mixing of the spin states in the intermediate region due to the field-induced level crossing. Changes of the magnetic field therefore have a strong impact on the mixed wavefunctions due to changes in the mixing coefficients, similar to the theoretical predictions for $TlCuCl_3$ [132].

The above described ESR excitations can qualitatively reproduce the experimental results. However, neutron diffraction experiments have unambiguously shown that, despite a weak coupling between the ladders, at least 3 different spin interactions have to be taken into account to correctly describe the spin dispersion in DTN [42].

Three-dimensional model

As for an adequate description of the spin dispersions observed in DTN the three nearest neighbor-interactions J_a, J_b and J_c have to be taken into account, the Hamilton operator reads:

$$\hat{H} = \sum_n \left(D\,(S_n^z)^2 + \sum_\nu J_\nu \hat{\vec{S}}_n \cdot \hat{\vec{S}}_{n,\nu} + g\mu_B\mu_0 \hat{\vec{H}}_n \cdot \hat{\vec{S}}_n \right), \tag{4.7}$$

where $\nu \in (a, b, c)$. A corresponding analysis of zero-field neutron scattering experiments has yielded $J_a = J_b = 0.015(1)\,\mathrm{meV}$, $J_c = 0.15(1)\,\mathrm{meV}$ and an anisotropy of $D = 0.699(1)\,\mathrm{meV}$. However, several different values have been reported for J_c and D [42, 126, 118], strongly depending on the used theoretical model.

Based on the above presented Hamilton operator, one can calculate the three-dimensional

spin dispersions and the corresponding ESR modes. Although the exact details differ somewhat, the basic form is very similar to the one-dimensional case. For the low field region, the calculated energy of the two excited bands $|1\rangle$ and $|-1\rangle$ is given by [126]:

$$\begin{aligned}\hbar\omega_{\pm}(\vec{k}) = D \pm g\mu_B\mu_0 H + 2\sum_{\nu} J_\nu \cos(a_\nu k_\nu) \\ + \frac{1}{D}\left[3\sum_{\nu} J_\nu^2 - 2\left(\sum_{\nu} J_\nu \cos(a_\nu k_\nu)\right)^2\right] \\ + \frac{1}{D^2}\left[2\sum_{\nu} J_\nu^3 + 4\left(\sum_{\nu} J_\nu \cos(a_\nu k_\nu)\right)^3 + \frac{5}{2}\sum_{\nu} J_\nu^3 \cos(a_\nu k_\nu)\right. \\ - 7\left(\sum_{\mu} J_\mu^2\right)\left(\sum_{\nu} J_\nu \cos(a_\nu k_\nu)\right) \\ \left. -2\left(\sum_{\mu} J_\mu^2 \cos(a_\mu k_\mu)\right)\left(\sum_{\nu} J_\nu^2 \cos(a_\nu k_\nu)\right)\right]. \end{aligned} \tag{4.8}$$

In the high field region, the energy of the non-magnetic state $|0\rangle$ is given by

$$\hbar\omega(\vec{k}) = g\mu_B\mu_0 H - D - 2\left(\sum_{\nu} J_\nu(\cos(a_\nu k_\nu) - 1)\right). \tag{4.9}$$

As analytical results for spin states in the intermediate region have not been reported up to now, a number of numerical calculations have been performed [124, 126] in order to successfully explain the experimentally obtained results in this field region, which are summarized in Fig. 4.5. These data are in good agreement with Fig. 4.3 when the calculations are based on the three-dimensional model with the interaction constants $J_x = J_y = 0.34\,\mathrm{K}$, $J_z = 8.9\,\mathrm{K}$, an anisotropy $D = 8.9\,\mathrm{K}$ and a g-value of $g = 2.22$ [126]. At low frequencies and fields between $\mu_0 H = 7\,\mathrm{T}$ and $\mu_0 H = 8\,\mathrm{T}$, an Y-structure of the frequency field diagram has been reported, stemming from the two-magnon continuum. For temperatures and fields that are high enough so that the state $\hbar\omega_-$ and the two-magnon band can be thermally excited, transitions between those two become observable. At very low temperatures ($T < 0.45\,\mathrm{K}$, however, this Y-shape has been shown to disappear with a gapped double-U structure developing (see Fig. 4.5). The latter is typical for the avoided crossing of energy levels. Thus, a lowering of the temperature changes the energy spectrum not only quantitatively, but also qualitatively in the intermediate region.

Tabelle 4.1: Comparison of the calculated ESR frequencies for the one- and three-dimensional case up to third order in $\frac{1}{D}$. For $J_x = J_y = 0$ and $J_z = J$, the formulas for the one- and three-dimensional case are equivalent, as expected.

	1-dim [128]	3-dim [126]
$\hbar\omega_A$	$D + X_1 + \frac{X_2}{D} + \frac{X_3}{D^2} + g\mu_0\mu_B H$	$D + X_1 + \frac{X_2}{D} + \frac{X_3}{D^2} + g\mu_0\mu_B H$
$\hbar\omega_B$	$D + X_1 + \frac{X_2}{D} + \frac{X_3}{D^2} - g\mu_0\mu_B H$	$D + X_1 + \frac{X_2}{D} + \frac{X_3}{D^2} - g\mu_0\mu_B H$
X_1	$2J$	$2\sum_\nu J_\nu$
X_2	J^2	$3\sum_\nu J_\nu^2 - 2\left(\sum_\nu J_\nu\right)^2$
X_3	$\frac{1}{2}J^3$	$2\sum_\nu J_\nu^3 + 4\left(\sum_\nu J_\nu\right)^3 + \frac{5}{2}\sum_\nu J_\nu^3$- $-7\left(\sum_\mu J_\mu^2\right)\left(\sum_\nu J_\nu\right) - 2\left(\sum_\mu J_\mu^2\right)\left(\sum_\nu J_\nu^2\right)$
$\hbar\omega_C$	$g\mu_B\mu_0 H - D$	$g\mu_B\mu_0 H - D$
$\hbar\omega_G$	$g\mu_B\mu_0 H + D$	$g\mu_B\mu_0 H + D$
$\hbar\omega_F$	$g\mu_B\mu_0 H + D - 4J + 2\frac{J^2}{D} + \frac{J^3}{D^2}$	$g\mu_B\mu_0 H + D - 4\left(\sum_\nu J_\nu\right) +$ $+\frac{2}{D}\left(\sum_\nu J_\nu^2\right) + \frac{1}{D^2}\left(J_\nu^3\right)$

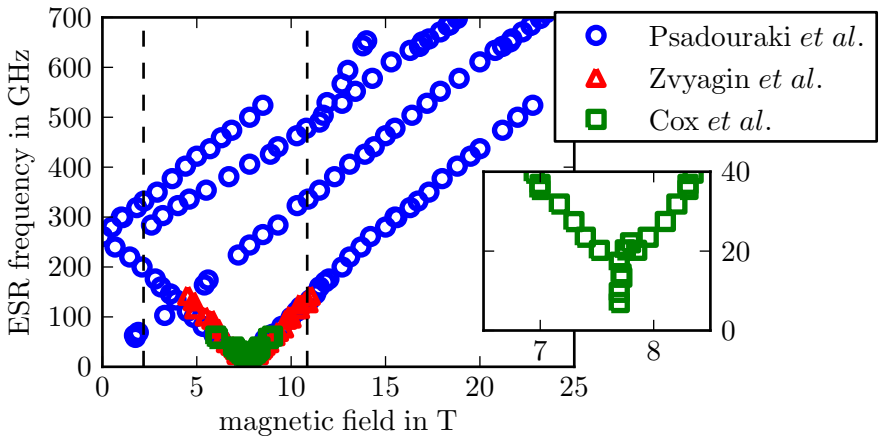

Abbildung 4.5: Reported ESR data for DTN above the critical temperature ($4.2\,\mathrm{K} > T > 1.5\,\mathrm{K}$). The data points have been taken from Refs. [123, 124, 126]. The inset is a magnification to demonstrate the reported Y-shape of the ESR diagram (see text). The dashed vertical lines mark the lower and upper critical field of the quasiparticle BEC.

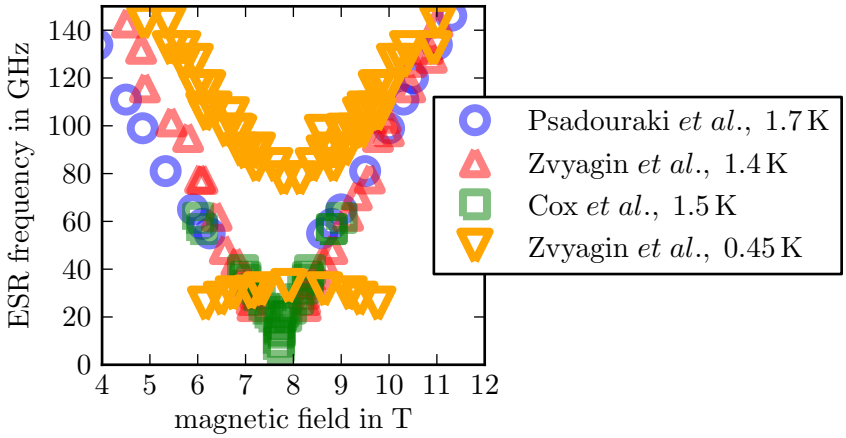

Abbildung 4.6: Comparison of reported experimental ESR data for DTN above ($T \geq 1.4\,\mathrm{K}$) and below the critical temperature ($T = 0.45\,\mathrm{K}$). The data points have been taken from Refs. [123, 124, 126].

4.2 DTN as a prototype system for the the construction of a Josephson-device of magnetic insulators

Close to $T = 0$, the intermediate region between the critical fields H_{c1} and H_{c2} marks the BEC phase of DTN. Similar to the triplon case, the BEC transition takes place as soon as the first exited state $|-1\rangle$ crosses the ground state $|0\rangle$. The new ground state is a superposition of the two states with field-dependent mixing coefficients. The field dependence of these coefficients ensures a smooth transition of the ground state from non-magnetic below H_{c1} to fully polarized above H_{c2}. The experimental values for these critical fields are $\mu_0 H_{c1} = 2.18(1)\,\mathrm{T}$ and $\mu_0 H_{c2} = 10.85\,\mathrm{T}$ [42].

These parameters and the overall behavior of the spin system can be changed when gradually replacing the Cl atoms by Br, creating Br-DTN. On a microscopic level, the Cl(1) position (see Fig. 4.1) is then randomly occupied by either Cl or Br, so that a portion of the Ni spins interact through a Ni-Br-Cl-Ni exchange path. The corresponding change of the exchange energies leads to an increase of the interaction constant along the c-axis to $J_c' = 2.3 J_c = 5.1\,\mathrm{K}$ and a decrease of the anisotropy to $D' = \frac{D}{2} = 4.45\,\mathrm{K}$ for neighboring Ni spins [118]. The relative strength of the spin-spin interaction, $\rho = \frac{J}{D}$ thus increases from $\rho = 0.25$ to $\rho' = 1.13$ so that the anisotropy can no longer be considered to be large. When constructing spatially confined spin chains entirely from Ni-Cl-Br-Ni bonds, the excitation spectrum would exhibit a gap Δ_L that decreases with an increasing length L of the spin chain, vanishing in the thermodynamic limit $L \to \infty$. The actual crystal will be composed of Ni-Cl-Cl-Ni and Ni-Cl-Br-Ni chains with varying length. Subsystems of the whole crystal that consist of finite, but long chains of the latter type can thus exhibit an arbitrarily small gap. In terms of the spin-boson mapping discussed

briefly in section 1.2, this vanishing gap results in the presence of bosonic quasiparticles in these subsystems even for a vanishing external field. These effectively gapless parts of the system will then order at low temperatures and are thus considered as *mini-BEC* at $T = 0$ [118]. When applying an external magnetic field, the chemical potential of the chains is further lowered, resulting in the creation of additional bosonic quasiparticles. At low temperatures, these additional bosons will be localized around the Br-rich regions.

Upon increase of the temperature, however, the quasiparticles are expected to delocalize and move decoherently throughout the sample. For high enough magnetic fields, the whole system (including the Br-free regions) undergoes an ordering transition, leading to the emergence of a long range phase coherence of the quasiparticles. This transition takes place at lower magnetic fields in comparison to the pure material. As discussed in section 1.2, the magnetic field acts as a source for the bosonic quasiparticles. Due to the gapless regions, the quasiparticle density for a given magnetic field is always higher for Br-DTN than for pure DTN so that the critical density is reached at lower fields.

For a Br-concentration of 7.5 %, the critical fields are shifted to $\mu_0 H_{c1} = 1.072(5)\,\mathrm{T}$ and $H_{c2} = 12.162(5)\,\mathrm{T}$ [118]. This corresponds to a shift of the lower critical field of about $\Delta H_{c1} = 1.11(2)\,\mathrm{T}$. Based on the discussion in section 1.3, a Josephson device of Br-DTN and DTN should thus exhibit correspondingly separated side peaks to transitions from the ground state in the frequency spectrum. As shown in section 4.4, the width of the ESR resonances is much smaller than ΔH_{c1} so that these additional peaks should be well observable. For higher concentrations of Br, H_{c1} is even further reduced (see Fig. 4.7), so that an even larger separation is to be expected

Contrary to the usual floating zone technique used to obtain single crystals of $Ba_3Cr_2O_8$ and $Sr_3Cr_2O_8$ (see section 3) the growth of DTN from solution naturally allows to prepare a composite sample with two different stoichiometries. In our case, these devices consist of a core of Br-DTN, surrounded by a shell of pure DTN (see Fig. 4.8). The samples were of tetragonal shape with an approximately square basis in the *ab*-plane ($1.9 \times 1.9\,\mathrm{mm}^2$) and long tetragonal faces along the *c*-axis ($1.9 \times 4\,\mathrm{mm}^2$) with a total mass of about 16 mg. In Fig. 4.9, we have plotted the susceptibility of such a combined device, showing the separate transitions of core and shell. At $T = 0.43\,\mathrm{K}$, the difference of the critical fields for $x = 0.15$ is about

$$\mu_0 \Delta H_c = 1.3\,\mathrm{T}, \tag{4.10}$$

which would correspond to the separation of the expected sidebands.

4.3 ESR experiments on DTN-based samples above T_c

The corresponding ESR experiments were performed using the MVNA ESR setup at the IFW in Dresden, Germany. A sample of DTN with the dimensions $1.5 \times 1.5 \times 3\,\mathrm{mm}^3$ was

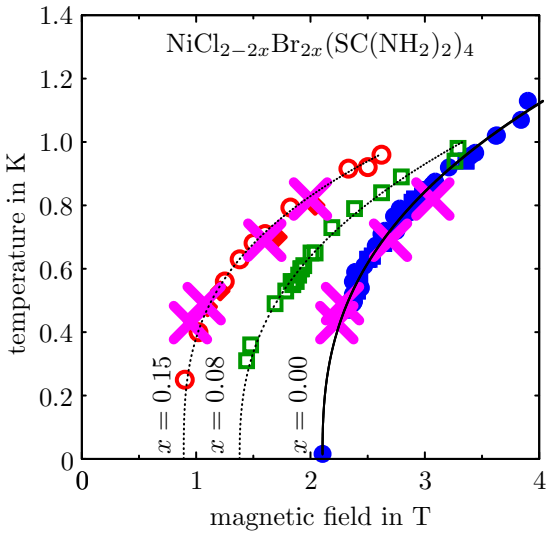

Abbildung 4.7: Critical temperature as a function of the external magnetic field in $NiCl_{2-2x}Br_{2x}(SC(NH_2)_2)_4$ for $x = 0$, $x = 0.08$ and $x = 0.15$ [133]. The magenta-colored crosses represent the values obtained for our combined device consisting of a core with $x = 0.15$ and a shell with $x = 0$ (see Fig. 4.9). The solid and dashed lines are guides to the eye.

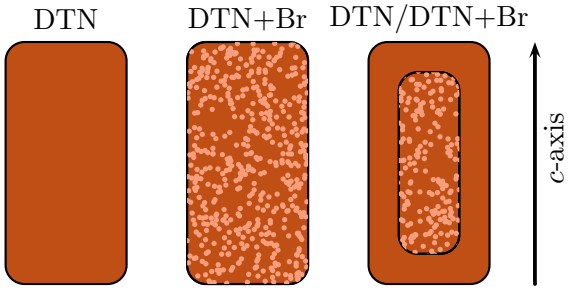

Abbildung 4.8: Sketch of the DTN-based samples used for our ESR-experiments. The sample geometry was essentially given by the shape of the unit cell, so that no cutting was necessary.

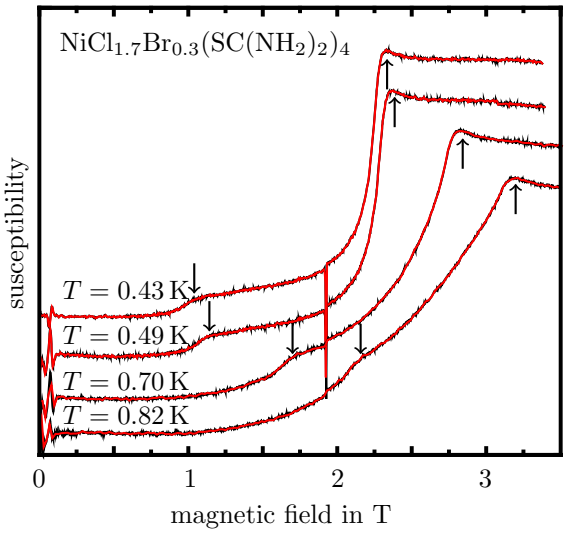

Abbildung 4.9: Susceptibility of a DTN/Br-DTN device as a function of the temperature [133]. The separate phase transitions are marked by arrows (downwards for the Br-rich core, upwards for the pure DTN shell).

examined using frequencies between 83 GHz and 410 GHz at $T = 2\,\mathrm{K}$ and $T = 5\,\mathrm{K}$, well above the maximum critical temperature of the system. The field was applied along the c-axis. As described above, the excitation spectrum of DTN has already been obtained at these temperatures so that these initial experiments have been performed mostly for verification purposes. As shown in Fig. 4.10, the reported ESR resonances could be well reproduced. Due to the high experimental resolution, a yet unreported fine structure could be resolved especially for the lines A and C (see Fig. 4.11). Such a fine structure is, however, in accordance with the reported theoretical calculations [126].

To probe possible changes in the spin excitation spectrum above the critical fields due to the partial replacement of Cl by Br, we have also examined a sample of Br-DTN

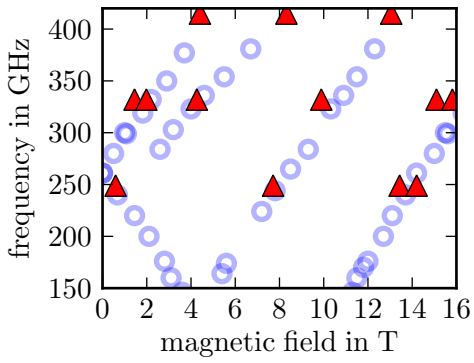

Abbildung 4.10: Measured frequency-field diagram (triangles) for pure DTN in comparison with the published data [126] (open circles).

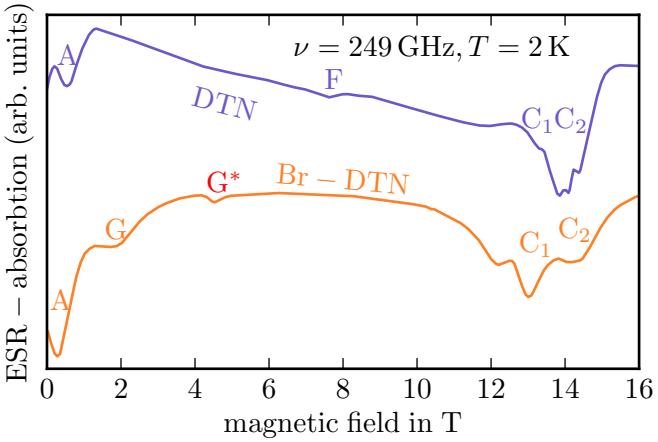

Abbildung 4.11: Comparison of the obtained ESR absorption spectra for pure DTN and Br-DTN, obtained at $T = 2\,\mathrm{K}$.

using the same setup with the field along the c-axis at $T = 2\,\mathrm{K}$. When comparing the corresponding ESR absorption spectra at $T = 2\,\mathrm{K}$ and $\nu = 249\,\mathrm{GHz}$ for pure DTN and Br-DTN, changes of the relative intensities, especially of the A- and C-line become evident (see Fig. 4.11). In addition, a new resonance can be found between the G- and the F-line that we labeled as G*. Depending on the used ESR frequency, the intensity of this new line even surpasses that of the reported G line (see Fig. 4.12).

It is likely that the additional resonance appears because of changes in the spin excitation spectrum due to the gradual exchange of Cl by Br. However, as all ESR resonances that can be found in pure DTN remain unaffected, a change of the interaction constants J_a, J_b and J_c as well as of the anisotropy D for the whole sample can be ruled out. One could also hypothesize that the additional resonance stems from the Br-rich regions. Similar to line G, which stems from the transition $|0\rangle \rightarrow |1\rangle$ above H_{c1} in pure DTN, one could assign line G* to the transition $|0'\rangle \rightarrow |1'\rangle$ in Br-rich regions. Using the reported anisotropy and interaction constants [118], one can estimate the resonance frequency of such a transition. The resulting frequency, calculated based on Eqs. 4.3 and 4.6, is somewhat too low to satisfactorily explain the resonance G*, especially in higher magnetic fields (see Fig. 4.13). However, due to the increased intrachain interaction J_c' and the decreased anisotropy D', Br-rich chains do not fully fall into the range of validity of the one- and three-dimensional calculations as sketched above. One can thus not expect this approximation to give an exact description of the additional resonance. Although one would also expect additional ESR resonances F* and C* that are analogues to lines F and C, it is possible that the complex ESR excitation spectra of DTN make their detection very difficult due to overlap with existing features.

Thus, the above presented explanation for the additional resonance G* can neither be fully verified nor ruled out, but has been considered for the analysis of the ESR spectra of the DTN/Br-DTN device presented in the next chapter.

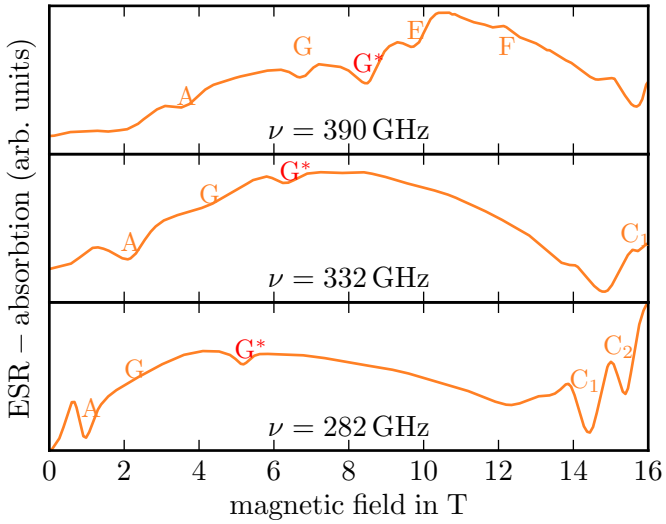

Abbildung 4.12: ESR transmission spectra for Br-DTN at different ESR frequencies, obtained at $T = 2\,\mathrm{K}$.

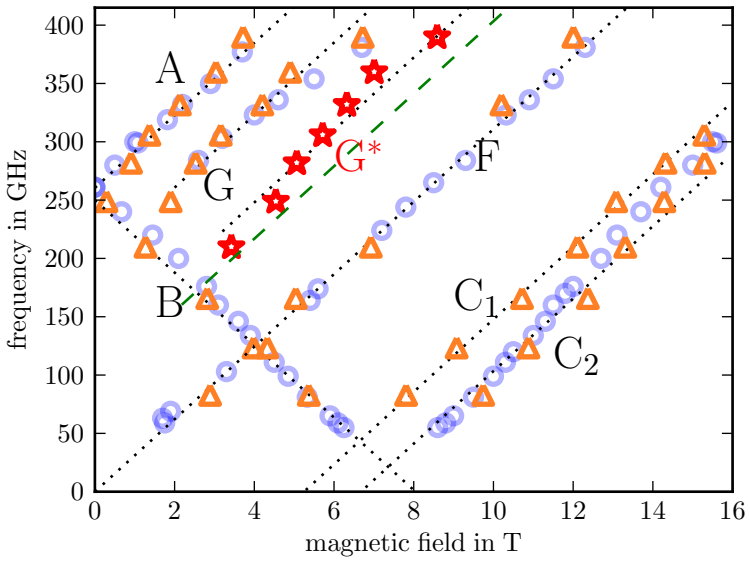

Abbildung 4.13: Frequency-field diagram of Br-DTN. The dotted lines are linear fits to the data according to $\nu = g\mu_B B + \alpha$ with $g = 2.22$. The green dashed line is an estimate for G* that would stem from Br-rich regions according to Tab. 4.1 with $D = 4.45\,\mathrm{K}$ [118] (see text).

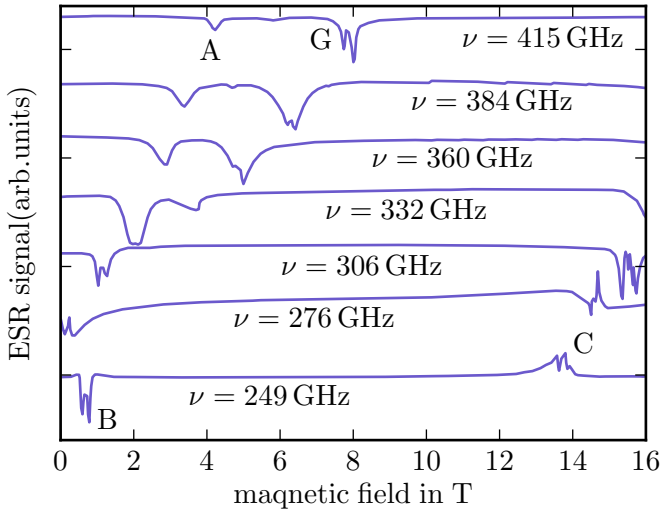

Abbildung 4.14: ESR transmission spectra of a small sample of pure DTN (see text). The baseline of each spectrum has been shifted according to the ESR frequency ν by $\Delta S = \alpha\nu$ with a constant α to emphasize the linear frequency-field dependence.

4.4 ESR experiments on DTN-based samples below T_c

Cooling DTN below the critical temperature not only changes the intensity of the observed ESR transitions, but also introduces profound changes to the frequency-field diagram (see Fig. 4.6). In order to verify that the calculations of the transition frequencies in the high field region based on Eqs. 4.3 and 4.6 still hold below T_c, we have performed ESR absorption experiments below $T = 0.4\,\mathrm{K}$. The initial measurements were performed on a sample of pure DTN with a total mass of about 0.5 mg. This is much less than the mass of the samples which were examined around $T = 2\,\mathrm{K}$ (described in the last section). The ESR spectra obtained from this small sample do not show any signs of the G* resonance found in Br-DTN. The observed resonance lines generally agree quite well with those found at higher temperatures. So that the appearance of the additional resonance G* seems to be an effect of the gradual replacement of Cl by Br. As expected, no transitions between excited states have been observed. The fine structure that has been observed at higher temperatures (see section 4.3) is even more pronounced below T_c and can be observed for all resonances. We believe that this is a clear sign of additional interactions that have been proposed in the literature [122], but are not included in the Hamilton operator that was used to determine the spin dispersion (see Eq. 4.1).

At low enough temperatures, the intermediate field region corresponds to the BEC phase of DTN, so that line G would represent excitations from the condensed state between H_{c1} and H_{c2}, corresponding to possible excitation frequencies $260\,\mathrm{GHz} < \nu < 510\,\mathrm{GHz}$. Following section 1.3, we thus concentrated our efforts to observe possible Josephson

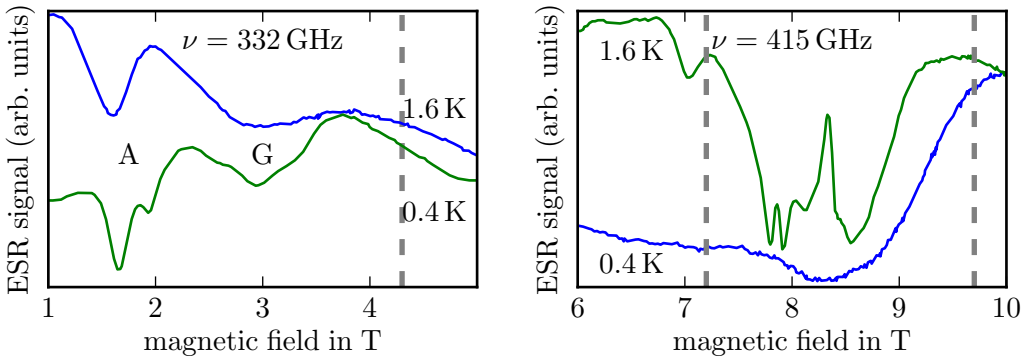

Abbildung 4.15: ESR transmission spectra of a DTN/Br-DTN core-shell device obtained below T_c (0.4 K) and above T_c (1.6 K) for two different ESR excitation frequencies. The dashed lines mark the expected position of side bands for $T = 0.4\,\mathrm{K}$. While for $\nu = 415\,\mathrm{GHz}$ only the G-line is visible for the shown field range, the resonances A and G can be observed for $\nu = 332\,\mathrm{GHz}$ and are labeled accordingly. For $\nu = 332\,\mathrm{GHz}$, one would expect sidebands only for fields above the resonance field for the G-line as the system is not in the BEC state for fields below $\mu_0 H = 2.18\,\mathrm{T}$. The G*-feature is located above the shown field range.

effects in a corresponding device made from DTN on this resonance. We have performed ESR excitation experiments on a DTN/Br-DTN device for temperatures above and below the critical field for several ESR excitation frequencies with $\nu < 415\,\mathrm{GHz}$. In Fig. 4.15, we have plotted the corresponding ESR excitation spectra for $\nu = 332\,\mathrm{GHz}$ and $\nu = 415\,\mathrm{GHz}$. Although we could clearly resolve the fine structure of the G-line, we were unable to identify the expected sidebands in any of the recorded ESR spectra of the DTN/Br-DTN sample.

As described above, one could think of interpreting the line G* observed in Br-DTN as an excitation from the ground state in Br-rich regions. Similar to the G-line, one could thus expect corresponding side bands to the G* line for the coupled device in the condensed phase. In Fig. 4.16, we have plotted a typical ESR spectrum around the G* line for several temperatures, obtained with $\nu = 332\,\mathrm{GHz}$. As in the case of the G-line, no side bands could be observed. As the achieved experimental resolution is good enough considering the expected separation of the sidebands, we conclude that these sidebands are absent in the present device.

This absence might be viewed as a sign that the concept of BEC is not completely applicable to phase transition of the spin system and, concordantly, no long range phase coherence is present in these systems. It should also be noted that the theoretical descriptions of the spin system in terms of bosonic quasiparticles that condense into their ground state are usually formulated for dilute systems with a very small quasiparticle density, $n \ll 1$. This quasiparticle density n depends on the difference $H - H_{c1}$ between

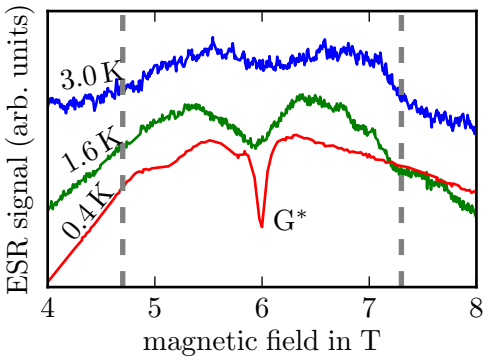

Abbildung 4.16: Comparison of ESR spectra for the examined DTN/Br-DTN device obtained with $\nu = 332\,\mathrm{GHz}$ for $T \in \{0.4\,\mathrm{K}, 1.6\,\mathrm{K}, 3.0\,\mathrm{K}\}$ around line G*. The dashed lines mark the expected position of sidebands in the spectrum taken at $T = 0.4\,\mathrm{K}$ according to Eq. 4.10.

the applied external magnetic field and the critical magnetic field of the condensation. Thus, the experimental parameters where chosen in such a way that the sample is in the BEC state, but close to the phase transition where the correlation length ξ of the condensate diverges. However, it is not clear how well the condition of diluteness was met during our experiments. In addition, the A and the G-line are very close to each other for fields close to the phase boundary, so that possible side bands could have been interpreted as being part of the A-line.

Furthermore, it is not known whether the coupling between core and shell of the device is strong enough to induce side bands of measurable intensity (see Fig. 1.13). As shown in section 1.3, the sidebands for weak couplings have a much lower intensity than the main line. If the effective sample volume for those sidebands is a small region on both sides of the boundary between core and shell, the total intensity of the sidebands is further reduced. It may thus not be possible to detect the expected Josephson effects in this core-shell configuration.

A possible alternative version of such a Josephson device would be a stacked array of two thin films of magnetic insulators with differing critical fields. These could be deposited, e.g. by sputtering or molecular beam epitaxy techniques. These films would offer a much greater control of the transition region, and the total volume of the boundary region could be enhanced by repeated stacking of these thin films. However, developing such a process for even one isolated film of a compound that is supposed to exhibit a BEC of magnetic quasiparticles is highly challenging and time consuming and has, to the best of our knowledge, not yet been attempted.

Conclusion and Outlook

The main purpose of this PhD work was to verify the existence of a long range phase coherence in the supposed BEC phase of certain magnetic insulators. To probe this phase coherence, we have developed a new experimental concept that is based on a coupling of two such magnetic insulators with different critical fields. When both materials are driven to their respective BEC states, the difference of the critical field should lead to characteristic changes in the frequency spectrum of the device when compared to the uncondensed state.

We have therefore searched for systems where the critical fields can be changed by altering the stoichiometry. Our corresponding experiments have revealed that the magnetic interactions in $Ba_{3-x}Sr_xCr_2O_8$ can be changed by varying the Sr content x. The change can be attributed to the gradual suppression of a Jahn-Teller transition which heavily influences the strength of the magnetic interactions in the system. This suppression seems to be induced by the chemical disorder that stems from the gradual element replacement.

Our experiments have shown that due to the change of the magnetic interactions in $Ba_{3-x}Sr_xCr_2O_8$, the critical fields are altered based on the Sr content x. As the change of the critical field is sizable even for small modifications of the stoichiometry, we believe that this system is a good candidate for the construction of a Josephson device.

However, important questions concerning $Ba_{3-x}Sr_xCr_2O_8$ remain unanswered by the present work. The most important issue is the large discrepancy between the phase boundary of the BEC state obtained by the extraction magnetization technique and the boundary obtained by heat capacity and magnetocaloric measurements. As this problem seems to be apparent only in the system $\{Ba,Sr\}_3\{Cr,Mn\}_2O_8$ it deserves specific attention, before starting the complicated process of constructing a Josephson device of $Ba_{3-x}Sr_xCr_2O_8$.

The usual preparation procedure of $Ba_{3-x}Sr_xCr_2O_8$, involving solid state reactions and floating zone growth, is not suited to obtain a high quality coupling with a confined geometry and a well defined boundary between the two coupled materials. Especially this last requirement calls for new techniques such as sputtering or molecular beam epitaxy. These methods have been successfully used to obtain Josephson junctions of ceramic superconductors. To the best of our knowledge, they have never been used

for samples that are candidates for a quasiparticle BEC so that high efforts could be necessary to adapt the technique to these materials.

In addition of these issues concerning the probing of properties inherent to the BEC phase, it is worthwhile to further examine the effects of the element exchange on the Jahn-Teller transition. As such transitions are based on the degeneracy of atomic orbitals, probing the corresponding Cr orbitals in $Ba_{3-x}Sr_xCr_2O_8$, e.g. by photoemission spectroscopy, would be important in order to test the proposed scenario for the suppression of the transition.

As no Josephson device constructed of $Ba_{3-x}Sr_xCr_2O_8$ is yet available, we have performed high field ESR techniques on a device of $NiCl_2(SC(NH_2)_2)_4$, where the difference of the critical fields has been achieved by gradually replacing Cl by Br in a part of the sample. These ESR experiments have revealed that the gradual atomic replacement induces profound changes of the energy spectrum even in the uncondensed state, with a new resonance appearing. However, our experiments could neither unambiguously confirm nor disprove the expected changes of the energy spectra of the material in the condensed phase. The question of the existence of a long range phase coherence in the supposed BEC phase of the examined spin systems thus still remains unanswered.

To sum up, our experimental efforts have not yet succeeded at answering the question of whether or not the phase transition found in insulating spin systems can be regarded as a true BEC. However, our results indicate that this question might be answered using a new experimental route beyond the established methods, which may be viewed as an even more encouraging prospect.

References

[1] A. Einstein. Sitzungsberichte der Preussischen Akademie der Wissenschaften (1924) 261.

[2] S. Bose. Z. Phys. **26** (1924) 178.

[3] M. H. Anderson, J. R. Ensher, M. R. Matthews, C. E. Wieman and E. A. Cornell. Science **269** (1995) 198.

[4] K. B. Davis, M. O. Mewes, M. R. Andrews, N. J. van Druten, D. S. Durfee, D. M. Kurn and W. Ketterle. Phys. Rev. Lett. **75** (1995) 3969.

[5] J. F. Anett. *Supraleitung, Suprafluidität und Kandensate*. Oldenbourg Verlag München (2011).

[6] W. Nolting. *Statistische Physik*. Springer-Verlag (2005).

[7] J.-h. Wang and Y.-l. Ma. J. Phys. B **43** (2010) 175301.

[8] M. Campostrini, M. Hasenbusch, A. Pelissetto and E. Vicari. Phys. Rev. B **74** (2006) 144506.

[9] N. N. Bogoliubov. J. Phys. (USSR) (1947) 23.

[10] V. N. Popov. *Functional integrals and collective excitations*. Cambridge University Press (1987).

[11] P. Kapitza. Nature **141** (1938) 74.

[12] J. F. Allen and A. D. Misene. Nature **142** (1938) 643.

[13] E. L. Andronikashvili. J. Exp. Theor. Phys. (U.S.S.R.) **10** (1946) 201.

[14] Z. M. Galasiewicz. *Helium 4*. Pergamon Press ((1971).

[15] L. Tisza. Phys. Rev. **72** (1947) 838.

[16] W. H. Keesom, B. Saris and L. Meyer. Physica **7** (1940) 817.

[17] J. F. Kerrisk and W. E. Keller. Phys. Rev. **177** (1969) 341.

[18] F. London and P. R. Zilsel. Phys. Rev. **74** (1948) 1148.

[19] M. H. Anderson, J. R. Ensher, M. R. Matthews, C. E. Wieman and E. A. Cornell. Science **269** (1995) 198.

[20] S. O. Demokritov, V. E. Demidov, O. Dzyapko, G. A. Melkov, A. A. Serga, B. Hillebrands and A. N. Slavin. Nature **443** (2006) 430.

[21] V. E. Demidov, O. Dzyapko, S. O. Demokritov, G. A. Melkov and A. N. Slavin. Phys. Rev. Lett. **100** (2008) 047205.

[22] H. Deng, G. Weihs, C. Santori, J. Bloch and Y. Yamamoto. Science **298** (2002) 199.

[23] J. Kasprazak, M. Richard, S. Kundermann, A. Baas, P. Jeambrun, J. M. J. Keeling, F. M. Marchetti, M. H. Szymanska, R. André, J. L. Staehli, V. Savona, P. B. Littlewood, B. Deveaud and L. S. Dang. Nature **443** (2006) 409.

[24] E. Ising. Z. Phys. **31** (1925) 253.

[25] H. Bethe. Z. Phys. A **71** (1931) 205.

[26] L. Hulthén. Arkiv Mat. Astron. Fysik **1938** (26A) 1938.

[27] E. Dagotto and T. M. Rice. Science **271** (1996) 618.

[28] T. Barnes, E. Dagotto, J. Riera and E. S. Swanson. Phys. Rev. B **47** (1993) 3196.

[29] T. Giamarchi and A. M. Tsvelik. Phys. Rev. B **59** (1999) 11398.

[30] A. Oosawa, M. Ishii and H. Tanaka. J. Phys.: Cond. Matter **11** (1999) 265.

[31] H. Tanaka, A. Oosawa, T. Kato, H. Uekusa, Y. Ohashi, K. Kakurai and A. Hoser. J. Phys. Soc. Jap. **70** (2001) 939.

[32] R. Chitra, S. Pati, H. R. Krishnamurthy, D. Sen and S. Ramasesha. Phys. Rev. B **52** (1995) 6581.

[33] T. Nakamura, S. Takada, K. Okamoto and N. Kurosawa. J. Phys.: Cond. Matter **9** (1997) 6401.

[34] R. Dell'Amore, A. Schilling and K. Krämer. Phys. Rev. B **79** (2009) 014438.

[35] A. Oosawa, T. Kato, H. Tanaka, K. Kakurai, M. Müller and H.-J. Mikeska. Phys. Rev. B **65** (2002) 094426.

[36] A. A. Aczel, Y. Kohama, M. Jaime, K. Ninios, H. B. Chan, L. Balicas, H. A. Dabkowska and G. M. Luke. Phys. Rev. B **79** (2009) 100409.

[37] A. A. Aczel, Y. Kohama, C. Marcenat, F. Weickert, M. Jaime, O. E. Ayala-Valenzuela, R. D. McDonald, S. D. Selesnic, H. A. Dabkowska and G. M. Luke. Phys. Rev. Lett. **103** (2009) 207203.

[38] T. Waki, K. Masaki, Y. Itoh, C. Michioka, K. Yoshimura and T. Goto. Journal of Physics and Chemistry of Solids **66** (2005) 1432 . ISSN 0022-3697. Proceedings of the {ISSP} International Symposium (ISSP-9)on Quantum Condensed System.

[39] M. Jaime, V. F. Correa, N. Harrison, C. D. Batista, N. Kawashima, Y. Kazuma, G. A. Jorge, R. Stern, I. Heinmaa, S. A. Zvyagin, Y. Sasago and K. Uchinokura. Phys. Rev. Lett. **93** (2004) 087203.

[40] T. Nikuni, M. Oshikawa, A. Oosawa and H. Tanaka. Phys. Rev. Lett. **84** (2000) 5868.

[41] R. Dell'Amore, A. Schilling and K. Krämer. Phys. Rev. B **78** (2008) 224403.

[42] V. S. Zapf, D. Zocco, B. R. Hansen, M. Jaime, N. Harrison, C. D. Batista, M. Kenzelmann, C. Niedermayer, A. Lacerda and A. Paduan-Filho. Phys. Rev. Lett. **96** (2006) 077204.

[43] M. Campostrini, M. Hasenbusch, A. Pelissetto, P. Rossi and E. Vicari. Phys. Rev. B **63** (2001) 214503.

[44] M. Matsumoto, B. Normand, T. M. Rice and M. Sigrist. Phys. Rev. Lett. **89** (2002) 077203.

[45] C. Rüegg, N. Cavadini, A. Furrer, H.-U. Güdel, K. Krämer, H. Mutka, A. Wildes, K. Habicht and P. Vorderwisch. Nature **423** (2003) 62.

[46] K. Kudo, M. Yamazaki, T. Kawatama, T. Noji, Y. Koike, T. Nishizaki, N. Kobayashi and H. Tanaka. J. Phys. Soc. Jpn. **73** (2004) 2358.

[47] K. Kudo, M. Yamazaki, T. Kawatama, T. Noji, Y. Koike, T. Nishizaki, N. Kobayashi and H. Tanaka. J. Magn. Magn. Mater. **272-276** (2004) 214.

[48] M. Sato, T. Kawamata, K. Naruse, K. Kudo, N. Kobayashi and Y. Koike. JPCS **400** (2012) 032079.

[49] M. Sato, T. Kawamata, N. Sugawara, N. Kaneko, M. Uesaka, K. Kudo, N. Kobayashi and Y. Koike. JPCS **200** (2010) 022054.

[50] R. Dell'Amore. *Bose-Einstein Condensation in the Quantum Spin-System $TlCuCl_3$: Any Sign of "Magnetic Superfluidity?"*. Ph.D. thesis, University of Zürich (2008).

[51] T. Lorenz, S. Stark, O. Heyer, N. Hollmann, A. Vasiliev, A. Oosawa and H. Tanaka. J. Magn. Magn. Mater. **316** (2007) 291.

[52] A. Oosawa, H. A. Katori and H. Tanaka. Phys. Rev. B **63** (2001) 134416.

[53] K. Nawa, C. Michioka, K. Yoshimura, A. Matsuo and K. Kindo. J. Phys. Soc. Jpn. **80** (2011) 034710.

[54] E. C. Samulon, K. A. Al-Hassanieh, Y.-J. Jo, M. C. Shapiro, L. Balicas, C. D. Batista and I. R. Fisher. Phys. Rev. B **81** (2010) 104421.

[55] W. Shiramura, K.-i. Takatsu, H. Tanaka, K. Kamishima, M. Takahashi, H. Mitamura and T. Goto. J. Phys. Soc. Jpn. **66** (1997) 1900.

[56] A. Oosawa, T. Takamasu, K. Tatani, H. Abe, N. Tsujii, O. Suzuki, H. Tanaka, G. Kido and K. Kindo. Phys. Rev. B **66** (2002) 104405.

[57] L. Yin, J. S. Xia, V. S. Zapf, N. S. Sullivan and A. Paduan-Filho. Phys. Rev. Lett. **101** (2008) 187205.

[58] A. Aczel. *Studies of Bose-Einstein Condensates in Magnetic Insulators*. Ph.D. thesis, McMaster University (2010).

[59] D. Quintero-Castro. Private communication.

[60] M. Tachiki and T. Yamada. J. Phys. Soc. Jpn. **28** (1970) 1413.

[61] M. Tachiki and T. Yamada. Progr. Theor. Phys. Suppl. .

[62] T. Giamarchi, C. Ruegg and O. Tchernyshyov. Nat. Phys. **4** (2004) 198 .

[63] V. N. Glazkov, A. I. Smirnov, H. Tanaka and A. Oosawa. Phys. Rev. B **69** (2004) 184410.

[64] A. K. Kolezhuk, V. N. Glazkov, H. Tanaka and A. Oosawa. Phys. Rev. B **70** (2004) 020403.

[65] J. Sirker, A. Wei√üe and O. P. Sushkov. Europhys. Lett. **68** (2004) 275.

[66] E. Y. Sherman, P. Lemmens, B. Busse, A. Oosawa and H. Tanaka. Phys. Rev. Lett. **91** (2003) 057201.

[67] O. Vyaselev, M. Takigawa, A. Vasiliev, A. Oosawa and H. Tanaka. Phys. Rev. Lett. **92** (2004) 207202.

[68] A. Schilling and H. Grundmann. Ann. of Phys. **327** (2012) 2309.

[69] R. P. Feynman, R. B. Leighton and M. Sands. *The Feynman Lectures on Physics*, volume Vol. III. Addison-Wesley (1965).

[70] D. N. Langenberg, D. J. Scalapino, B. N. Taylor and R. E. Eck. Phys. Rev. Lett. **15** (1965) 294.

[71] V. M. Yanson, K. Svistunov and I. M. Dmitrenko. J. Exp. Theor. Phys. **21** (1965) 650.

[72] R. Ozeri, N. Katz, J. Steinhauer and N. Davidson. Rev. Mod. Phys. **77** (2005) 187.

[73] K. Kopitzki. *Einführung in die Festkörperphysik*. Teubner Verlag (1993).

[74] N. D. Mermin. J. Math. Phys. **7** (1966) 1038.

[75] N. W. Ashcroft and D. N. Mermin. *Festkörperphysik*. Oldenburg Verlag (2013).

[76] W. Coffey, Y. P. Kalmykov and W. T. Waldron. *The Langevin Equation*. World Scientific Publishing Co. Pte. Ltd. (2004).

[77] B. W. Batterman, D. R. Chipman and J. J. DeMarco. Phys. Rev. **122** (1961) 68.

[78] F. S. Vareley. Neutron News **3** (1992) 26.

[79] T. W. Crane and M. P. Baker. *Passive nondestructive assay of nuclear materials*. United States Nuclear Regulatory Comission (1991).

[80] P. Fischer, G. Frey, M. Koch, M. Könnecke, V. Pomjakushin, J. Schefer, R. Thut, S. N., R. Bürge, U. Greuter, S. Bondt and E. Berruyer. Physica B: Cond. Matt. **276-278** (2000) 146 .

[81] W. Heisenberg. Z. Phys. **43** (1927) 172. ISSN 0044-3328.

[82] *Bruker EMX Users Manual (1998).*

[83] A. Alfonsov. *High-field electron spin resonance study of electronic inhomogeneities in correlated transition metal compounds.* Ph.D. thesis, Technische Universität Dresden (2011).

[84] J. B. Gunn. Solid State Communications **1** (1963) 88 . ISSN 0038-1098.

[85] C. Golze, A. Alfonsov, R. Klingeler, B. Büchner, V. Kataev, C. Mennerich, H.-H. Klauss, M. Goiran, J.-M. Broto, H. Rakoto, S. Demeshko, G. Leibeling and F. Meyer. Phys. Rev. B **73** (2006) 224403.

[86] D. L. Quintero-Castro, B. Lake, E. M. Wheeler, A. T. M. N. Islam, T. Guidi, K. C. Rule, Z. Izaola, M. Russina, K. Kiefer and Y. Skourski. Phys. Rev. B **81** (2010) 014415.

[87] G. Radtke, A. Saúl, H. A. Dabkowska, G. M. Luke and G. A. Botton. Phys. Rev. Lett. **105** (2010) 036401.

[88] H.-J. Koo, K.-S. Lee and M.-H. Whangbo. Inorg. Chem. **45** (2006) 10743.

[89] T. Dodds, B.-J. Yang and Y. B. Kim. Phys. Rev. B **81** (2010) 054412.

[90] H. Schwarz. Die Naturwissenschaften **52** (1965) 206.

[91] R. Scholder and H. Suchy. Z. anorg. allg. Chem. **308** (1961) 295.

[92] H.-J. Mattausch and H.-K. Müller-Buschbaum. Z. Naturforsch. B **27** (1972) 739.

[93] E. Cuno and H.-K. Müller-Buschbaum. Z. anorg. allg. Chem. **572** (1989) 95.

[94] M. Kofu, H. Ueda, H. Nojiri, Y. Oshima, T. Zenmoto, K. C. Rule, S. Gerischer, B. Lake, C. D. Batista, Y. Ueda and S.-H. Lee. Phys. Rev. Lett. **102** (2009) 177204.

[95] M. Kofu, J.-H. Kim, S. Ji, S.-H. Lee, H. Ueda, Y. Qiu, H.-J. Kang, M. A. Green and Y. Ueda. Phys. Rev. Lett. **102** (2009) 037206.

[96] B. Leuenberger, A. Stebler, H. U. Güdel, A. Furrer, R. Feile and J. K. Kjems. Phys. Rev. B **30** (1984) 6300.

[97] T. Nakajima, H. Mitamura and Y. Ueda. J. Phys. Soc. Jpn. **75** (2006) 054706.

[98] Y. Singh and D. C. Johnston. Phys. Rev. B **76** (2007) 012407.

[99] B. Bleaney and K. D. Bowers. Proc. R. Soc. A **214** (1952) 451.

[100] D. L. Quintero-Castro. *Neutron Scattering Investigations on 3d and 4f Frustrated Magnetic Insulators*. Ph.D. thesis, Technische Universität Berlin (2011).

[101] L. Chapon, C. Stock, P. G. Radaelli and C. Martin **arXiv:0807.0877v2**.

[102] M.-H. Whangbo, D. Dai and H.-J. Koo. Solid State Sciences **7** (2005) 827 . ISSN 1293-2558. Selected articles from the 4th International Conference on Inorganic Materials Antwerp, Belgium 19-21 Septembre 2004.

[103] P. J. Hay, J. C. Thibeault and R. Hoffmann. J. Am. Chem. Soc. **97** (1975) 4884.

[104] D. Kamenskyi, J. Wosnitza, J. Krzystek, A. Aczel, H. Dabkowska, A. Dabkowski, G. Luke and S. Zvyagin. J. Low Temp. Phys. **170** (2013) 231. ISSN 0022-2291.

[105] Z. Wang, M. Schmidt, A. Günther, S. Schaile, N. Pascher, F. Mayr, Y. Goncharov, D. L. Quintero-Castro, A. T. M. N. Islam, B. Lake, H.-A. Krug von Nidda, A. Loidl and J. Deisenhofer. Phys. Rev. B **83** (2011) 201102.

[106] M. Matsumoto, T. Shoji and M. Koga. J. Phys. Soc. Jpn. **77** (2008) 074712.

[107] S. Kimura, M. Hagiwara, H. Tanaka, A. K. Kolezhuk and K. Kindo. J. Magn. Magn. Mater. **310** (2007) 1218 . ISSN 0304-8853. Proceedings of the 17th International Conference on Magnetism The International Conference on Magnetism.

[108] S. Kimura, K. Kindo and H. Tanaka. Physica B: Cond. Matt. **346-347** (2004) 15 . ISSN 0921-4526. Proceedings of the 7th International Symposium on Research in High Magnetic Fields.

[109] H. Tanaka, T. Takatsu, W. Shiramura, T. Kambe, H. Nojiri, T. Yamada, S. Okubo, H. Ohta and M. Motokawa. Physica B: Cond. Matt. **246-247** (1998) 545 .

[110] Z. Wang, D. Kamenskyi, O. Cépas, M. Schmidt, D. L. Quintero-Castro, A. T. M. N. Islam, B. Lake, A. A. Aczel, H. A. Dabkowska, A. B. Dabkowski, G. M. Luke, Y. Wan, A. Loidl, M. Ozerov, J. Wosnitza, S. A. Zvyagin and J. Deisenhofer. Phys. Rev. B **89** (2014) 174406.

[111] H. A. Dabkowska and A. B. Dabkowski. *Springer Handbook of Crystal Growth, Defects and Characterization*, chapter 12, 367–391. Springer Berlin Heidelberg (2010).

[112] I. D. Brown and D. Altermatt. Acta Crystallogr. Sect. B **41** (1985) 244.

[113] R. M. Wood, K. A. Abboud, R. C. Palenik and G. J. Palenik. Inorg. Chem. **39** (2000) 2065.

[114] C. Shannon. Bell Syst. Tech. J. **27** (1948) 379.

[115] A. Abragam and B. Bleaney. *Electron Paramagnetic Resonance of Transition Ions*. Oxford University Press (1970).

[116] S. J. Blundell and K. M. Blundell. *Concepts in Thermal Physics*. Oxford University Press (2010).

[117] A. Aczel. Private communication.

[118] R. Yu, L. Yin, N. S. Sullivan, J. S. Xia, C. Huan, A. Paduan-Filho, N. F. Oliveira Jr, S. Haas, A. Steppke, C. F. Miclea, F. Weickert, R. Movshovich, E.-D. Mun, B. L. Scott, V. S. Zapf and T. Roscilde. Nature **489** (2012) 379.

[119] A. Lopez-Castro and M. R. Truter. J. Chem. Soc. (1963) 1309.

[120] A. Paduan-Filho, R. D. Chirico, K. O. Joung and R. L. Carlin. J. Chem. Phys **74** (1981) 4103.

[121] A. Paduan-Filho, X. Gratens and N. F. Oliveira. Phys. Rev. B **69** (2004) 020405.

[122] S. Zvyagin, C. Batista, J. Krzystek, V. Zapf, M. Jaime, A. Paduan-Filho and J. Wosnitza. Physica B: Cond. Matt. **403** (2008) 1497 . ISSN 0921-4526. Proceedings of the International Conference on Strongly Correlated Electron Systems.

[123] S. A. Zvyagin, J. Wosnitza, A. K. Kolezhuk, V. S. Zapf, M. Jaime, A. Paduan-Filho, V. N. Glazkov, S. S. Sosin and A. I. Smirnov. Phys. Rev. B **77** (2008) 092413.

[124] S. Cox, R. D. McDonald, M. Armanious, P. Sengupta and A. Paduan-Filho. Phys. Rev. Lett. **101** (2008) 087602.

[125] S. A. Zvyagin, J. Wosnitza, C. D. Batista, M. Tsukamoto, N. Kawashima, J. Krzystek, V. S. Zapf, M. Jaime, N. F. Oliveira and A. Paduan-Filho. Phys. Rev. Lett. **98** (2007) 047205.

[126] C. Psaroudaki, S. A. Zvyagin, J. Krzystek, A. Paduan-Filho, X. Zotos and N. Papanicolaou. Phys. Rev. B **85** (2012) 014412.

[127] A. K. Kolezhuk and H.-J. Mikeska. Phys. Rev. B **65** (2001) 014413.

[128] N. Papanicolaou, A. Orendáčová and M. Orendáč. Phys. Rev. B **56** (1997) 8786.

[129] A. V. Sizanov and A. V. Syromyatnikov. Phys. Rev. B **84** (2011) 054445.

[130] R. Silberglitt and J. B. Torrance. Phys. Rev. B **2** (1970) 772.

[131] C. Psaroudaki. Private communication.

[132] M. Matsumoto, B. Normand, T. M. Rice and M. Sigrist. Phys. Rev. B **69** (2004) 054423.

[133] A. Paduan-Filho. Private communication.

Appendix - Structural details of $Ba_{3-x}Sr_xCr_2O_8$

Tabelle 4.2: Lattice parameters and atomic coordinates in $Ba_{3-x}Sr_xCr_2O_8$ for $0 \leq x \leq 1.33$ obtained at room temperature.

		x=0.0	x=0.33	x=0.66	x=1.0	x=1.33
a=b		5.74038	5.72971(9)	5.71411(8)	5.69371(9)	5.67664(8)
c		21.38354	21.2889(3)	21.1549(3)	21.0063(4)	20.8729(3)
	x	0.00000	0.00000	0.00000	0.00000	0.00000
Cr	y	0.00000	0.00000	0.00000	0.00000	0.00000
(6c)	z	0.40766(8)	0.40760(8)	0.40740(8)	0.40687(9)	0.40673(8)
	B_{iso}	0.45(3)	0.72(3)	0.85(3)	1.05(3)	1.21(3)
	x	0.00000	0.00000	0.00000	0.00000	0.00000
Ba_1/Sr_1	y	0.00000	0.00000	0.00000	0.00000	0.00000
(3a)	z	0.00000	0.00000	0.00000	0.00000	0.00000
	B_{iso}	0.97(3)	1.22(4)	1.65(4)	1.81(4)	1.76(4)
	occ.	1.0/0(0)	0.88/0.12(2)	0.77/0.23(2)	0.7/0.3(2)	0.64/0.37(1)
	x	0.00000	0.00000	0.00000	0.00000	0.00000
Ba_2/Sr_2	y	0.00000	0.00000	0.00000	0.00000	0.00000
(6c)	z	0.20600(8)	0.20586(7)	0.20567(7)	0.20547(7)	0.20485(6)
	B_{iso}	0.55(2)	0.76(2)	0.93(2)	1.03(2)	1.10(2)
	occ.	1.0/0(0)	0.89/0.11(8)	0.78/0.22(8)	0.65/0.35(1)	0.52/0.48(7)
	x	0.00000	0.00000	0.00000	0.00000	0.00000
O_1	y	0.00000	0.00000	0.00000	0.00000	0.00000
(6c)	z	0.32906(9)	0.32860(8)	0.32797(8)	0.32765(8)	0.32706(6)
	B_{iso}	2.43(3)	2.61(3)	2.95(3)	3.07(3)	3.01(3)
	x	0.82791(9)	0.82823(9)	0.82889(10)	0.82911(9)	0.82967(6)
O_2	y	0.17209(9)	0.17177(9)	0.17111(10)	0.17089(9)	0.17033(6)
(18h)	z	0.89885(4)	0.89878(4)	0.89853(4)	0.89847(4)	0.89823(4)
	B_{iso}	1.024(11)	1.239(12)	1.466(12)	1.577(13)	1.637(12)

Tabelle 4.3: Lattice parameters and atomic coordinates in $Ba_{3-x}Sr_xCr_2O_8$ for $1.66 \leq x \leq 3$ obtained at room temperature.

		x=1.66	x=2.0	x=2.33	x=2.66	x=3.0
a=b		5.65396(15)	5.63354(8)	5.61265(9)	5.59098(3)	5.57071(6)
c		20.7165(6)	20.5707(3)	20.4338(4)	20.28850(16)	20.1654(3)
	x	0.00000	0.00000	0.00000	0.00000	0.00000
Cr	y	0.00000	0.00000	0.00000	0.00000	0.00000
(6c)	z	0.40659(15)	0.40775(6)	0.40681(11)	0.40615(10)	0.40530(10)
	B_{iso}	1.06(4)	0.91(3)	0.94(4)	0.83(3)	0.58(3)
	x	0.00000	0.00000	0.00000	0.00000	0.00000
Ba_1/Sr_1	y	0.00000	0.00000	0.00000	0.00000	0.00000
(3a)	z	0.00000	0.00000	0.00000	0.00000	0.00000
	B_{iso}	1.59(7)	1.54(4)	2.00(5)	1.53(4)	1.39(3)
	occ.	0.59/0.42(2)	0.46/0.55(2)	0.19/0.81(2)	0.16/0.84(2)	0/1.0(0)
	x	0.00000	0.00000	0.00000	0.00000	0.00000
Ba_2/Sr_2	y	0.00000	0.00000	0.00000	0.00000	0.00000
(6c)	z	0.20434(10)	0.20420(6)	0.20393(8)	0.20367(7)	0.20371(7)
	B_{iso}	1.02(3)	0.93(2)	1.10(3)	1.03(2)	0.816(19)
	occ.	0.37/0.62(1)	0.27/0.72(9)	0.24/0.76(1)	0.09/0.92(1)	0/1.0(0)
	x	0.00000	0.00000	0.00000	0.00000	0.00000
O_1 (6c)	y	0.00000	0.00000	0.00000	0.00000	0.00000
	z	0.32666(14)	0.32490(6)	0.32507(11)	0.32433(10)	0.32332(10)
	B_{iso}	3.02(5)	2.90(3)	3.16(4)	2.82(4)	2.68(4)
	x	0.82982(16)	0.83102(11)	0.83164(13)	0.83195(12)	0.83252(12)
O_2 (18h)	y	0.17018(16)	0.16898(11)	0.16835(13)	0.16805(12)	0.16748(12)
	z	0.89810(7)	0.89784(4)	0.89808(5)	0.89821(5)	0.89903(5)
	B_{iso}	1.474(18)	1.545(15)	1.643(16)	1.507(15)	1.281(14)

Tabelle 4.4: Lattice parameters and atomic coordinates in $Ba_{3-x}Sr_xCr_2O_8$ for $0 \leq x \leq 3$ obtained at $T = 2\,\mathrm{K}$.

		x=0.0	x=0.33	x=1.33	x=2.33	x=3.0
a		9.89993(16)	9.8845(2)	5.65455(8)	9.71586(19)	9.66544(10)
b		5.72162(9)	5.70827(14)	5.65455(8)	5.58357(11)	5.54178(6)
c		14.6191(2)	14.5559(3)	20.8334(3)	13.9739(3)	13.78653(15)
β		103.1217(7)	103.1426(14)	90.00000	103.4912(7)	103.6774(4)
Cr (8f)/(6c)	x	0.2033(7)	0.2045(8)	0.00000	0.2035(4)	0.2031(3)
	y	0.2497(9)	0.2511(14)	0.00000	0.2560(5)	0.2555(4)
	z	0.86078(16)	0.86041(16)	0.40677(8)	0.85928(13)	0.85805(10)
	B_{iso}	0.02(4)	0.51(4)	0.92(3)	0.58(3)	0.53(2)
Ba_1/Sr_1 (4e)/(3a)	x	0.00000	0.00000	0.00000	0.00000	0.00000
	y	0.26547(16)	0.2631(15)	0.00000	0.2779(5)	0.2847(2)
	z	0.25000	0.25000	0.00000	0.25000	0.25000
	B_{iso}	0.02(4)	0.56(5)	1.46(4)	1.08(4)	0.527(18)
	occ.	1.0/0(0)	0.89/0.11(0)	0.62/0.39(2)	0.29/0.71(2)	0/1.0(0)
Ba_2/Sr_2 (8f)/(6c)	x	0.10045	0.1032(7)	0.00000	0.1021(3)	0.10176(15)
	y	0.2482(7)	0.2506(10)	0.00000	0.2480(3)	0.24771(12)
	z	0.55933(15)	0.55907(15)	0.20483(6)	0.55547(9)	0.55455(6)
	B_{iso}	-0.09(2)	0.61(3)	0.83(2)	0.611(19)	0.558(11)
	occ.	1.0/0(0)	0.89/0.11(0)	0.53/0.48(8)	0.19/0.81(9)	0/1.0(0)
O_1 (8f)/(6c)	x	0.1628(5)	0.1516(7)	0.00000	0.1598(4)	0.15800(16)
	y	0.2837(6)	0.2727(12)	0.00000	0.2960(4)	0.31238(19)
	z	0.74290(14)	0.74232(14)	0.32694(7)	0.73715(12)	0.73509(8)
	B_{iso}	0.69(4)	1.62(6)	2.76(3)	1.46(3)	0.769(16)
O_2 (8f)/(18h)	x	0.1202(5)	0.8686(10)	0.83034(9)	0.1177(3)	0.11576(16)
	y	0.7473(15)	0.0075(13)	0.16966(9)	0.7728(4)	0.7810(2)
	z	0.5981(5)	0.6026(4)	0.89803(4)	0.5993(3)	0.59893(13)
	B_{iso}	0.46(7)	1.13(9)	1.467(11)	1.02(3)	0.686(20)
O_3 (8f)	x	0.8640(7)	0.1213(6)		0.8544(3)	0.85482(14)
	y	0.0059(10)	0.7508(16)		-0.0077(5)	-0.0110(3)
	z	0.6014(3)	0.5974(6)		0.60101(20)	0.60426(10)
	B_{iso}	0.23(6)	0.47(9)		1.25(4)	0.59(2)
O_3 (8f)	x	0.3623(7)	0.3644(10)		0.3724(3)	0.37492(12)
	y	0.9916(9)	0.9922(13)		0.9860(4)	0.98557(6)
	z	0.5943(3)	0.5941(4)		0.5905(2)	0.59014(11)
	B_{iso}	0.05(6)	0.95(10)		0.97(4)	0.80(2)

Tabelle 4.5: Selected bindings angles in $Ba_{3-x}Sr_xCr_2O_8$ for $0 \leq x \leq 0.66$ obtained at room temperature and $T = 2\,\mathrm{K}$.

	x=0.0		x=0.33		x=0.66
	RT	2 K	RT	2 K	RT
O_1-Cr-O_2	109.69(13)	110.2(5)	109.69(12)	109.0(6)	109.85(12)
O_1-Cr-O_3	109.69(13)	114.1(4)	109.69(12)	115.1(6)	109.85(12)
O_1-Cr-O_4	109.69(13)	105.9(4)	109.69(12)	105.9(6)	109.85(12)
O_1-Cr	1.681(3)	1.690(3)	1.682(2)	1.684(3)	1.680(2)
O_1-O_2	2.7663(17)	2.792(6)	2.7674(16)	2.763(8)	2.7723(16)
O_1-O_3	2.7663(17)	2.838(6)	2.7674(16)	2.849(8)	2.7723(16)
O_1-O_4	2.7663(17)	2.722(6)	2.7674(16)	2.727(8)	2.7723(16)
O_2-Cr	1.7027(8)	1.714(8)	1.7030(8)	1.710(11)	1.7070(8)
O_2-O_3	2.7768(5)	2.772(9)	2.7771(5)	2.797(12)	2.7809(6)
O_2-O_4	2.7768(5)	2.786(9)	2.7771(5)	2.769(10)	2.7809(6)
O_3-Cr	1.7027(8)	1.692(8)	1.7030(8)	1.691(9)	1.7070(8)
O_3-O_4	2.7768(5)	2.781(8)	2.7771(5)	2.780(12)	2.7809(6)
O_4-Cr	1.7027(8)	1.721(8)	1.7030(8)	1.732(11)	1.7070(8)

Tabelle 4.6: Selected bindings angles in $Ba_{3-x}Sr_xCr_2O_8$ for $1.33 \leq x \leq 2$ obtained at room temperature and $T = 2\,\mathrm{K}$.

	x=1.0	x=1.33		x=1.66	x=2.0
	RT	RT	2 K	RT	RT
O_1-Cr-O_2	110.16(13)	110.28(10)	110.35(11)	110.4(2)	109.59(10)
O_1-Cr-O_3	110.16(13)	110.28(10)	110.35(11)	110.4(2)	109.59(9)
O_1-Cr-O_4	110.16(13)	110.28(10)	110.35(11)	110.4(2)	109.59(9)
O_1-Cr	1.664(3)	1.663(2)	1.663(2)	1.656(4)	1.7043(17)
O_1-O_2	2.7638(16)	2.7667(12)	2.7688(14)	2.759(3)	2.7834(13)
O_1-O_3	2.7638(16)	2.7667(12)	2.7688(14)	2.759(3)	2.7834(13)
O_1-O_4	2.7638(16)	2.7667(12)	2.7688(14)	2.759(3)	2.7834(13)
O_2-Cr	1.7065(8)	1.7086(7)	1.7097(8)	1.7044(14)	1.7022(7)
O_2-O_3	2.7747(5)	2.7759(3)	2.7765(5)	2.7674(9)	2.7777(6)
O_2-O_4	2.7747(5)	2.7759(3)	2.7765(5)	2.7674(9)	2.7777(6)
O_3-Cr	1.7065(8)	1.7086(7)	1.7097(8)	1.7044(14)	1.7022(7)
O_3-O_4	2.7747(5)	2.7759(3)	2.7765(5)	2.7674(9)	2.7777(6)
O_4-Cr	1.7065(8)	1.7086(7)	1.7097(8)	1.7044(14)	1.7022(7)

Tabelle 4.7: Selected bindings angles in $Ba_{3-x}Sr_xCr_2O_8$ for $2.33 \leq x \leq 3$ obtained at room temperature and $T = 2\,\mathrm{K}$.

	x=2.33		x=2.66	x=3.0	
	RT	2 K	RT	RT	2 K
O_1-Cr-O_2	109.92(16)	109.6(3)	110.17(15)	110.08(15)	109.50(16)
O_1-Cr-O_3	109.92(16)	114.8(3)	110.17(15)	110.08(15)	116.46(16)
O_1-Cr-O_4	109.92(16)	106.7(3)	110.17(15)	110.08(15)	104.22(15)
O_1-Cr	1.670(3)	1.675(2)	1.660(3)	1.653(3)	1.6774(17)
O_1-O_2	2.764(2)	2.758(4)	2.7595(19)	2.7513(19)	2.7716(19)
O_1-O_3	2.764(2)	2.856(4)	2.7595(19)	2.7513(19)	2.8744(19)
O_1-O_4	2.764(2)	2.716(4)	2.7595(19)	2.7513(19)	2.6815(19)
O_2-Cr	1.7059(10)	1.701(5)	1.7051(10)	1.7038(9)	1.716(3)
O_2-O_3	2.7779(7)	2.778(4)	2.7723(7)	2.7718(7)	2.808(2)
O_2-O_4	2.7779(7)	2.775(4)	2.7723(7)	2.7718(7)	2.7781(19)
O_3-Cr	1.7059(10)	1.714(4)	1.7051(10)	1.7038(9)	1.704(3)
O_3-O_4	2.7779(7)	2.768(4)	2.7723(7)	2.7718(7)	2.7688(17)
O_4-Cr	1.7059(10)	1.711(4)	1.7051(10)	1.7038(9)	1.720(3)

Acknowledgements

The foundations of the project and thus my whole PhD-work relied heavily on the input and support of Professor Andreas Schilling. Although the progress was often not as fast as it could have been, he never limited my scientific freedom and patiently allowed me to explore my PhD topic in directions that might have seen not very fruitful in the beginning. Besides his interesting and unconventional thinking, his countless valuable suggestions when it finally came to bring our results to paper in form of manuscripts, proposals and even reports helped me immensely to develop a scientific writing style that really conveys my thoughts. I am truly grateful to him for these years of learning.

Although there may have been some delusional moments during those years as a PhD student when I believed the presented work was solely based on my own intellectuality, I know that "my" results would not exist without the constant help of my collaborators. Especially Dr. Marisa Medarde Barragan has contributed immensely to keep my work scientifically sound and my sometimes faltering spirit intact. Besides always giving me new concepts to explore, she constantly assured me (and made sure) that *everything will turn out nicely*, even when I myself was full of doubt about it. Together with Dr. Denys Sheptyakov, she also helped me to gain important insight into the sometimes tricky topic of structural refinement.

Professor Bruce Gaulin and Dr. Hanna Dabkowska have welcomed me with open arms for my visit at McMaster University, showing me how things are run abroad, allowing me to take part in their beam time and giving my list of results some interesting additions. Although the snowfall in Ontario failed to meet my (naive) expectations, I really have to thank all members of their lab for this nice Canadian winter.

I am furthermore indebted to Dr. Vladislav Kataev at the IFW in Dresden who granted me access to his ESR laboratory and help by his staff, even on the shortest possible notice. Especially Dr. Alexey Alfonsov has introduced me to the important concepts and techniques of electron spin resonance, thereby deepening my understanding of my own scientific topic. And of the Russian culture - the countless nights we spent discussing (and measuring, of course) will always be remembered.

The HZDR in Dresden has proven to be an excellent host with very competent and resourceful personnel. Dr. Sergei Zvyagin, Dr. Mykhaylo Ozerov and Dr. Tobias Förster have done all they can to ensure that I left for Zürich with satisfying results. And some

muscle soreness for joining their team in the latest running events in Dresden.

Stefan Siegrist has introduced me to the techniques of solid state reactions and prepared many of the samples used in this thesis himself. As not a single measurement would have been possible without samples of sufficient quality I am definitely indebted to him.

"My" students Leonie Ulrich, Phillippe Hasler and Daniel Destraz made my life as a supervisor quite simple with an unusually high working morale and a lot of interest in their topic.

Olaf Bossen, Kevin Inderbitzin, Simon Strässle and Fabian von Rohr have been almost exactly how I always expected good colleagues to be: critical and skeptical in professional discussions, but otherwise supportive and cheerful. Simon's subtle encouragements for our daily training sessions (and his constant reminder to think of my life after the PhD) will surely pay off in the long run. Olaf's contribution on the other hand has already been fruitful. His solid programming knowledge sped up my analyses immensely, while his assistance in moving from our flood-ridden apartment (and back, after reconstruction) was an even greater relief.

More than anything it is this sort of friendship and cordiality that I remember most distinctly now that I write these last sentences of my thesis. Though far away, my friends backed me up whenever necessary. Andreas Hirsch forced me to silence my weaker self and finish the Zürich Marathon with him. And the Team-Marathon. And the 80 km of the SOLA Duo run. Without him, I would probably be still sitting somewhere between St. Gallen and Zürich, pointlessly complaining to myself about peanuts such as the rain or numb feet. While still being busy with his own thesis and job applications. Martin Hofmann has read my thesis with the eyes of a theoretician and removed a number of lumps and bumps that only I could ever have perceived as clear and concise writing. Adam Dusza helped me to edit my talks until even I could understand them. They all have helped to keep my focus on the really important parts of life. I thank them for this (and for being such an amiable band of merry men).

In many cases thanking one's family is a mere phrase. However, my parents Kerstin and Ralf Grundmann (and my parents-in-law, Sabine and Reinhard Bär) definitely helped to bring my PhD project to a satisfying end. When they took our toddler for a three-week vacation, it not only meant sleeping through the night again, but also finishing of what feels like half of this thesis. A big *thanks* to you!

For you, my dear Eva and the inspiration you are to me, a simple *thank you* would not be enough. Alas, though considering myself as quite eloquent, I fail to mold my deep feelings of gratitude towards you into written words. Instead, I hope to show these feelings in the years that lie ahead of us.

List of Publications

Influence of disorder on the structural phase transition and magnetic interactions in $Ba_{3-x}Sr_xCr_2O_8$.
H. Grundmann, M. Medarde, and D. Sheptyakov and A. Schilling. Phys. Rev. B **90** (2014) 075101

Structure and magnetic interaction in the solid solution $Ba_{3-x}Sr_xCr_2O_8$
H. Grundmann, C.A. Marjerrison, H.A. Dabkowska, B.D. Gaulin and A. Schilling. Mat. Res. Bull. **48** (2013) 3108

Experimental tests for macroscopic phase coherence in magnetic-quasiparticle condensates of insulating spin systems.
A. Schilling, H. Grundmann and R. Dell'Amore. JPCS **400** (2012) 032081
(Invited paper at the LT-26, Beijing, Aug 11th - Aug 17th 2011)

On Josephson effects in insulating spin systems.
A. Schilling and H. Grundmann. Ann. Phys. **327** (2012) 2301.